First Sagittarius A* event horizon telescope results. II. EHT and multiwavelength observations, data processing, and calibration

Akiyama, K.; Alberdi, A.; Alef, W.; Algaba, J.C.; Anantua, R.; Asada, K.; ... ; et al.

The Astrophysical Journal Letters, 930:L13 (31pp), 2022 May 10 https://doi.org/10.3847/2041-8213/ac6675

First Sagittarius A* Event Horizon Telescope Results. II. EHT and Multiwavelength Observations, Data Processing, and Calibration

The Event Horizon Telescope Collaboration
(See the end matter for the full list of authors.)

Received 2022 February 28; revised 2022 April 4; accepted 2022 April 10; published 2022 May 12

Abstract

We present Event Horizon Telescope (EHT) 1.3 mm measurements of the radio source located at the position of the supermassive black hole Sagittarius A* (Sgr A*), collected during the 2017 April 5–11 campaign. The observations were carried out with eight facilities at six locations across the globe. Novel calibration methods are employed to account for Sgr A*'s flux variability. The majority of the 1.3 mm emission arises from horizon scales, where intrinsic structural source variability is detected on timescales of minutes to hours. The effects of interstellar scattering on the image and its variability are found to be subdominant to intrinsic source structure. The calibrated visibility amplitudes, particularly the locations of the visibility minima, are broadly consistent with a blurred ring with a diameter of $\sim$50 μas, as determined in later works in this series. Contemporaneous multiwavelength monitoring of Sgr A* was performed at 22, 43, and 86 GHz and at near-infrared and X-ray wavelengths. Several X-ray flares from Sgr A* are detected by Chandra, one at low significance jointly with Swift on 2017 April 7 and the other at higher significance jointly with NuSTAR on 2017 April 11. The brighter April 11 flare is not observed simultaneously by the EHT but is followed by a significant increase in millimeter flux variability immediately after the X-ray outburst, indicating a likely connection in the emission physics near the event horizon. We compare Sgr A*'s broadband flux during the EHT campaign to its historical spectral energy distribution and find that both the quiescent emission and flare emission are consistent with its long-term behavior.

Unified Astronomy Thesaurus concepts: Black holes (162)

1. Introduction

The first legacy set of papers by the Event Horizon Telescope (EHT) focused on M87* (Event Horizon Telescope Collaboration et al. 2019a, 2019b, 2019c, 2019d, 2019e, 2019f, hereafter M87* Papers I, II, III, IV, V, and VI), but Sagittarius A* (Sgr A*) was the spark that motivated the formation of the EHT. This work presents EHT observations of Sgr A* at 1.3 mm, which serve as the foundation for the observational and theoretical papers presented in this second legacy series (Event Horizon Telescope Collaboration et al. 2022a, 2022b, 2022c, 2022d, 2022e, 2022f, hereafter Papers I, II, III, IV, V, and VI).

Sgr A*, the $\sim 4 \times 10^6\, M_\odot$ black hole at the center of our own Milky Way (at a distance of $\sim$8 kpc), is the closest observable supermassive black hole (SMBH; e.g., Gravity Collaboration et al. 2019; Do et al. 2019a; Reid & Brunthaler 2020). Among all known black holes, Sgr A* has the largest predicted angular diameter of the black hole shadow ($\sim$50 μas; see Papers III and IV, and references therein). It is also a highly variable source, with flickering, flares, and other stochastic processes occurring across the electromagnetic spectrum on short and long timescales. These unique characteristics make Sgr A* an important laboratory for studying the fundamental physics and astrophysics of black holes at high angular resolution.

Sgr A* has been observed with millimeter very long baseline interferometry (VLBI) for over a quarter century. After initial successful 1 mm VLBI tests on quasars (Padin et al. 1990; Greve et al. 1995), Sgr A* was first successfully detected on a VLBI baseline between the IRAM 30 m telescope on Pico Veleta (PV) in Spain and a single antenna of the Plateau de Bure Interferometer in France in 1995 (Krichbaum et al. 1997). This detection revealed a compact source, with a size of 110 ± 60 μas (Krichbaum et al. 1998). Early size measurements at 3 and 1 mm were larger than expected (see, e.g., Lo et al. 1998), indicating that short-wavelength VLBI measures the intrinsic structure in Sgr A* rather than interstellar scattering along the line of sight. Subsequent VLBI experiments using wider recorded bandwidth and three telescopes with longer baselines provided a tighter estimate of the source size, 43^{+14}_{-8} μas, giving the first unambiguous detection of horizon-scale structure in Sgr A* (Doeleman et al. 2008). Meanwhile, continued VLBI observations at $\lambda \gtrsim 3$ mm were better able to characterize the properties of the anisotropic interstellar scattering screen (e.g., Bower et al. 2004; Johnson et al. 2018).

Excitement from these VLBI measurements was further galvanized by crucial theoretical and technical advancements made in parallel. Simulations of Sgr A* by Falcke et al. (2000) demonstrated that a shadow of the sort originally predicted by Bardeen (1973) would be observable with millimeter-wavelength VLBI.[161] Technological advances greatly increased the capabilities of the growing EHT, as detailed in M87* Paper II. These advances led to a new era in which the detection of Sgr A* on long baselines at 1 mm became routine (Fish et al. 2011; Johnson et al. 2015; Fish et al. 2016; Lu et al. 2018). Most significantly, the phased Atacama Large Millimeter/

[161] More details about the appearance of black holes are given in M87* Paper I.

submillimeter Array (ALMA; Matthews et al. 2018) participated in its first EHT science observations in 2017, along with other antennas that added to the baseline coverage. Indeed, data from these observations produced the M87* total-intensity (M87* Papers I, II, III, IV, V, VI) and polarization results (Event Horizon Telescope Collaboration et al. 2021a, 2021h, hereafter Papers VII and VIII), as well as high angular resolution images of extragalactic radio jets (Kim et al. 2020; Janssen et al. 2021). These data also motivate the Sgr A* results in this series.

As these VLBI discoveries were advancing, Sgr A* was also being studied intensively at other wavelengths. Radio, millimeter, infrared, and X-ray observations showed that Sgr A* has both a very low bolometric-to-Eddington luminosity ratio of $L/L_{\rm Edd} \sim 10^{-9}$ (Genzel et al. 2010) and a very low mass accretion rate of $\sim 10^{-9}$–$10^{-7}\ M_\odot\ {\rm yr}^{-1}$ (Baganoff et al. 2003; Marrone et al. 2006a, 2007; Shcherbakov et al. 2012; Yusef-Zadeh et al. 2015). At most wavelengths, Sgr A*'s flux can be decomposed into a quiescent and variable component.

In the X-ray, Sgr A* is a persistent source, with a flux of about 3×10^{33} erg s^{-1} (Baganoff et al. 2001, 2003) from thermal bremsstrahlung radiation originating from hot plasma near the Bondi radius (e.g., Quataert 2002; Baganoff et al. 2003; Yuan et al. 2003; Liu et al. 2004; Wang et al. 2013). Bright X-ray flares punctuate this emission about once per day and are characterized by nonthermal emission centered on the black hole (e.g., Neilsen et al. 2013). Near-infrared (NIR) detections of Sgr A* also reveal a highly variable source, with emission peaks observed more frequently than in the X-ray (Genzel et al. 2003; Ghez et al. 2004; Gravity Collaboration et al. 2020). Both the X-ray variability and NIR variability occur on timescales of several hours, consistent with emission originating near the black hole's innermost stable circular orbit (ISCO), which depends on the black hole's mass and spin. Sgr A*'s mid-IR flux is only marginally detected (e.g., Iwata et al. 2020), or it can be inferred indirectly from model fitting.

Millimeter polarimetry of Sgr A* reveals linearly polarized flux from an emitting region of $\sim$10 Schwarzschild radii ($R_{\rm S}$), which indicates a dense magnetized accretion flow again extending out to the Bondi radius. Bower et al. (2018) find a mean rotation measure (RM) of about -5×10^5 rad m^{-2} that can be modeled as a radiatively inefficient accretion flow (RIAF) with an accretion rate of $\sim 10^{-8}\ M_\odot\ {\rm yr}^{-1}$. Circular polarization is also detected at a mean value of $-1.1\% \pm 0.2\%$. Both the RM and the circular polarization are variable on timescales of hours to months (Bower et al. 2018).

Similarly, observations of Sgr A* between 15 and 43 GHz reveal variability at the 5%–10% level on timescales shorter than 4 days (Macquart & Bower 2006). Sgr A*'s flux density distribution at 217.5, 219.5, and 234.0 GHz was investigated recently by Iwata et al. (2020); they find variability on timescales of $\sim$tens of minutes to hours, indicating that the emission at these wavelengths is also likely to arise near the ISCO.

Hence, in addition to the excitement around resolving Sgr A*'s intrinsic structure at 1.3 mm, it became clear that multiwavelength (MWL) observations during the EHT campaign would offer the first opportunity to definitively connect the black hole's variable flux components with changes observed at horizon scales.

In this work we present the first EHT 1.3 mm observations of Sgr A*, alongside MWL data collected contemporaneously in 2017 April. Contemporaneous interferometric array data from ALMA and SMA have been analyzed and are described here (and are presented in more detail in a companion paper, Wielgus et al. 2022). The campaign also includes observations from the East Asian VLBI Network (EAVN), the Global 3 mm VLBI Array (GMVA), the Very Large Telescope (VLT), the Neil Gehrels Swift Observatory, the Chandra X-ray Observatory, and the Nuclear Spectroscopic Telescope (NuSTAR). These coordinated observations provide (quasi-)simultaneous MWL coverage with exceptional spatial and spectral resolution. Since variability at timescales of minutes to hours can be probed on horizon scales by the EHT and on a range of other spatial (and spectral) scales by these other observatories, combining them into a single "snapshot" spectral energy distribution (SED) maximizes the broadband constraints that the observations can place on theoretical models.

This manuscript (Paper II) is organized as follows. In Section 2 we present an overview of the 2017 EHT observing campaign. Section 3 delves more deeply into the EHT data calibration and reduction specific to these Sgr A* data. Section 4 outlines the MWL campaigns that accompanied the EHT observations. Section 5 describes the resulting EHT and MWL data products, including those provided via a public data archive, and discusses these new observations in the context of longer-term monitoring campaigns that have characterized Sgr A*'s variability over more than 20 yr. We offer a brief summary and conclusions in Section 6.

2. Event Horizon Telescope Observing Campaign

The first EHT observations of Sgr A* were collected in 2017 April, alongside contemporaneous broadband data—the coverage is shown in Figures 1 and 2. A detailed description of the EHT array and its instrumentation can be found in M87* Paper II, with further details related to the 2017 observing campaign in M87* Paper III. Here we provide a brief summary of this material, along with details pertinent to the observations of Sgr A* and associated calibration sources.

EHT observations were carried out with eight observatories at six locations: ALMA and the Atacama Pathfinder Experiment (APEX) on the Llano de Chajnantor in Chile, the Large Millimeter Telescope Alfonso Serrano (LMT) on Volcán Sierra Negra in Mexico, the James Clerk Maxwell Telescope (JCMT) and Submillimeter Array (SMA) on Maunakea in Hawai'i, the IRAM 30 m telescope on Pico Veleta (PV) in Spain, the Submillimeter Telescope (SMT) on Mt. Graham in Arizona, and the South Pole Telescope (SPT) in Antarctica. The locations of these telescopes are plotted in Figure 1 of Paper I.

Sgr A* was observed on five nights: 2017 April 5, 6, 7, 10, and 11. ALMA did not participate in the array for observations of Sgr A* on 2017 April 5 or 10. PV observed Sgr A* only on 2017 April 7. Weather conditions were good or excellent at all sites on all five observing nights. Median opacities on each night are provided in M87* Paper III. In this series of papers, we focus our analysis on April 6 and 7, which have the best (u, v)-coverage.

Two bands of approximately 2 GHz each were observed, centered at sky frequencies of 227.1 and 229.1 GHz ("low" and "high" bands, respectively). Single-dish stations recorded a 2-bit Nyquist-sampled bandwidth of 2048 MHz per polarization using

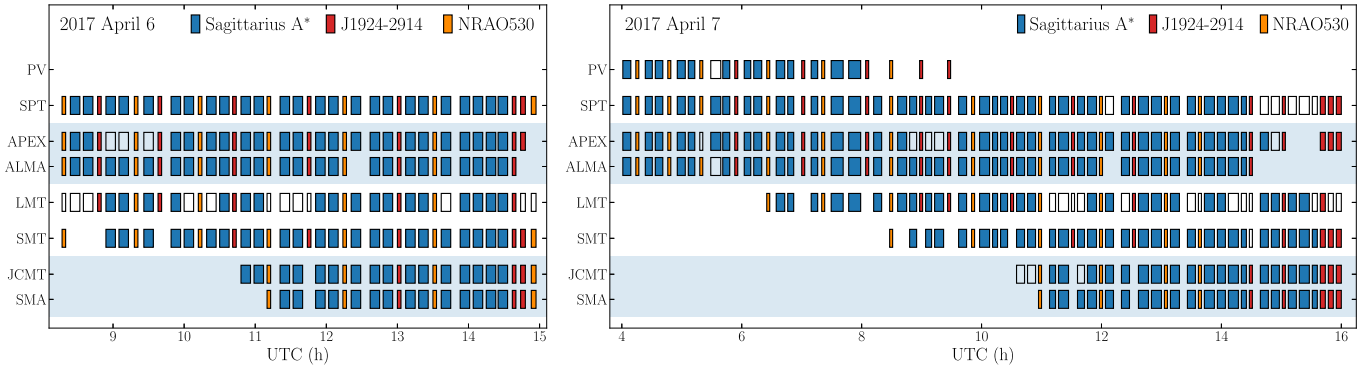

Figure 1. EHT 2017 observing schedules for Sgr A* and its calibrators (J1924−2914 and NRAO530), covering observations on 2017 April 6–7. Open rectangles represent scans that were scheduled but not observed successfully owing to weather or technical issues. The filled rectangles represent scans corresponding to detections available in the final data set. Scan durations vary between 3 and 12 minutes, as reflected by the width of each rectangle. ALMA/APEX and JCMT/SMA are pairs of colocated stations (enclosed in light-blue shaded regions), providing the same (u, v)-coverage.

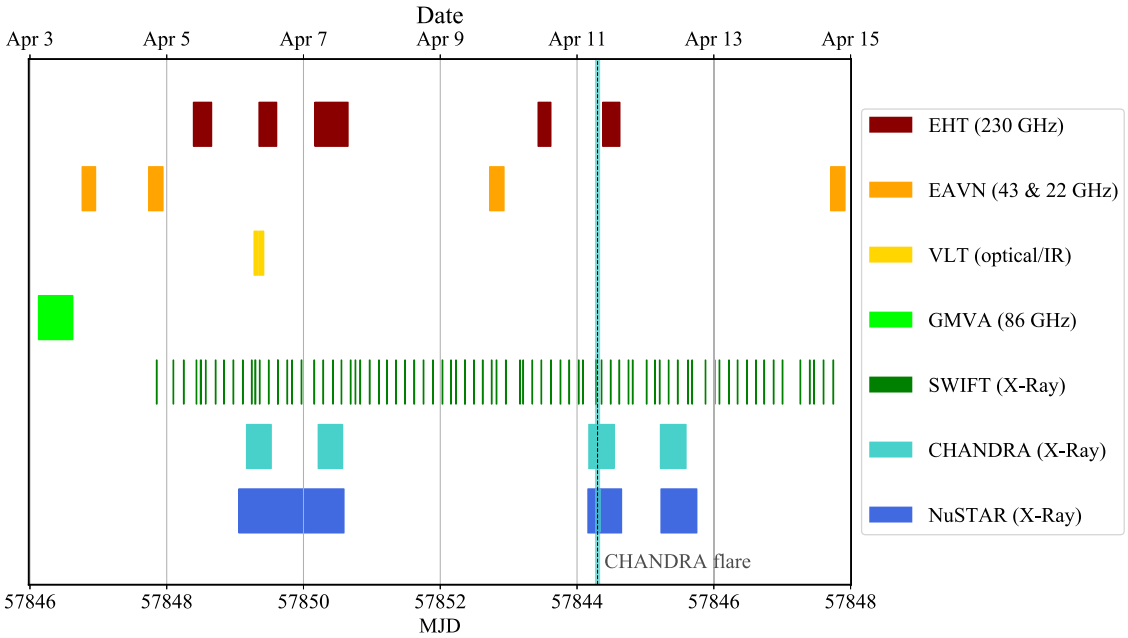

Figure 2. Instrument coverage of Sgr A* during the 2017 April 3–15 MWL observing campaign, which includes the East Asian VLBI Network (EAVN), the Global 3 mm VLBI Array (GMVA), the Very Large Telescope (VLT), the Neil Gehrels Swift Observatory (SWIFT), the Chandra X-ray Observatory (CHANDRA), and the Nuclear Spectroscopic Telescope (NuSTAR). For the EHT data described in this work we focus on April 6 and 7, which have the best (u, v)-coverage and for which detailed instrument and source coverage is shown in Figure 1. Details of the MWL campaign and SED are contained in Sections 4 and 5.2.1.

Reconfigurable Open Architecture Computing Hardware 2 (ROACH2) digital back ends (Vertatschitsch et al. 2015). The SMA observed using six or seven telescopes (depending on the observing night), whose signals were summed using the SMA Wideband Astronomical ROACH2 Machine (SWARM; Primiani et al. 2016; Young et al. 2016). Since SWARM produces data in the frequency domain at a different sampling rate than at other observatories, SMA data require a post-observation, pre-correlation pass through the Adaptive Phased-array and Heterogeneous Interpolating Downsampler for SWARM (APHIDS; see also the Appendix of M87* Paper II). ALMA observed as a phased array of 35–37 telescopes using the ALMA Phasing System (Matthews et al. 2018). Data were recorded onto Mark 6 VLBI Data Systems (Whitney et al. 2013).

All but two observatories recorded both left and right circular polarization (LCP and RCP, respectively). The JCMT was equipped with a single-polarization receiver that observed RCP on 2017 April 5–7 and LCP on 2017 April 10–11. ALMA recorded both linear polarizations (X and Y).

The schedule consisted of scans of Sgr A* interleaved with scans of NRAO 530 (J1733−1304) and J1924−2914 as calibration sources. On 2017 April 6, observations commenced after the preceding target source, M87, set at ALMA. Generally, two 8-minute scans of Sgr A* were followed by a short (typically 3-minute) scan on a calibrator, with an 8-minute gap approximately every hour. The 2017 April 7 schedule, which did not include M87, started when Sgr A* rose above the 20° elevation limit at ALMA. Scan lengths on Sgr A* for this schedule were dithered between 5 and 12 minutes to reduce the effects of periodic sampling on detection of time variability associated with the ISCO period. On both nights, Sgr A* was observed until the source set below the local

horizon at the SMT and LMT, which happens at approximately the same time. The scan coverage for these nights is shown in Figure 1.

Data were correlated with the Distributed FX (DiFX) software correlation package (Deller et al. 2011) at the two correlator centers at the Max-Planck-Institut für Radioastronomie in Bonn, Germany, and MIT Haystack Observatory in Westford, Massachusetts; for details see M87* Paper III. The CALC model was used for an a priori correction of rates and delays. Multiple correlation passes were required to diagnose and mitigate data issues, as discussed in the Appendix of M87* Paper III; parameters hereafter refer to those for the final correlation (Rev7) used for science-release data. The final correlation produced 32 baseband channels, each 58 MHz wide with a spectral resolution of 0.5 MHz and averaged to a 0.4 s accumulation period. The Sgr A* correlation center was set to $\alpha_{\rm J2000} = 17^{\rm h}45^{\rm m}40\overset{\rm s}{.}0356$, $\delta_{\rm J2000} = -29°00'28\overset{''}{.}240$[162], based on the position of Reid & Brunthaler (2004) corrected to the epoch of observation for the apparent motion introduced by the orbit of the solar system around the Galaxy. The corrected position produced smaller residual delays and rates compared with the uncorrected position, resulting in a minor improvement in sensitivity. Subsequent to correlation, PolConvert (Martí-Vidal et al. 2016) was run to convert the mixed-polarization data products (XL, XR, YL, YR) to the circular basis on ALMA baselines, as described in Goddi et al. (2019).

3. EHT Data Calibration and Reduction

In this section, we summarize the EHT data calibration pathway and highlight aspects that are particular for the Sgr A* data. A comprehensive description of the EHT data reduction methods, combined with a recap of VLBI data calibration fundamentals, is given in M87* Paper III.

3.1. Processing Pipelines

To reduce the volume of the data and to accumulate signal-to-noise ratio (S/N), we average the visibilities in time and frequency. To avoid nonclosing errors, we must stabilize the signal by removing all significant external data corruption effects that have not been captured by the correlator model beforehand. We apply scaling corrections as a function of time to the visibilities to ensure unity autocorrelations. Additionally, phase errors induced by atmospheric turbulence on second timescales must be modeled and removed (M87* Paper III). Along the frequency axis, residual post-CALC delays—phase slopes over the frequency band—are caused primarily by atmospheric path-length variations. No significant instrumental delay effects are present in our digital recording system. However, imperfect amplitude and phase bandpass responses impact the data and must be corrected.

We have developed two independent VLBI data reduction pipelines to perform these pre-averaging calibration steps to stabilize the signal: EHT-HOPS (Blackburn et al. 2019), which is based on the Haystack Observatory Postprocessing System (HOPS; Whitney et al. 2004) software, and rPICARD (Janssen et al. 2018, 2019b), which is based on the Common Astronomy Software Applications (CASA; McMullin et al. 2007; van Bemmel et al. 2019) package. The other papers in this series make use of the data produced from both pipelines, whose consistency has been established in M87* Paper III, for a verification of scientific results. The AIPS-based (Greisen 2003) pipeline that has also been used for the M87* EHT results (M87* Paper III) is no longer being maintained.

EHT-HOPS processes data that have been converted into Mark4 format by DiFX task `difx2mark4`. These correlation coefficients have been normalized to unity autocorrelation at 0.4 s × 58 MHz resolution and then scaled to idealized analog correlation amplitudes according to the 2-bit quantization efficiency correction factor $\sim 1/0.88$. Baseline rate and delay solutions are fit with the HOPS `fourfit` routine. These fringe solutions are then "globalized" into station-based corrections using a least-squares method (similar to Alef & Porcas 1986). A stable phase bandpass response for each antenna is derived using an ensemble of high-S/N detections on bright calibrators and applied to all data. Turbulent phases introduced by the troposphere are corrected by fitting a piecewise polynomial phase model to the visibilities from baselines connected to the most sensitive station in each scan. To avoid overfitting to thermal noise, the phases of each 58 MHz spectral window are independently corrected using a model derived from the other, remaining 31 spectral windows. Finally, the geometric feed rotation angle evolution is corrected, and relative complex gains between the RCP and LCP signal paths are fitted. We commonly refer to the calibrated data produced by the EHT-HOPS pipeline as "HOPS" data.

rPICARD follows the Hamaker–Bregman–Sault measurement equation (Hamaker et al. 1996; Smirnov 2011a, 2011b, 2011c, 2011d) as implemented in the CASA framework. For the amplitude calibration, the CASA `accor` task is used to enforce unity autocorrelations, correcting for digital sampler biases. As this task scales the visibilities at the 58 MHz resolution, it also corrects for the gross amplitude bandpass of each station. Residual amplitude bandpass effects are removed with a custom bandpass calibration table formed by taking the median of the normalized 0.5 MHz channelized autocorrelations of all VLBI scans combined. The phases are corrected with the `fringefit` task, which performs a global Schwab & Cotton (1983) fringe fit assuming an unpolarized point-source model. The data are segmented into the shortest bins within the expected atmospheric coherence time, where a sufficiently high S/N can be accumulated to obtain fringe detections. These detections are then used to correct for atmospheric phase turbulence and small residual delay variations that can occur within VLBI scans. A crude phase bandpass at 58 MHz is solved with a "single-band fringe fit," where we apply the solutions from the scan with the highest-S/N fringe solution per antenna. The residual 0.5 MHz phase bandpass is corrected with the CASA `bandpass` task with an S/N > 3 cutoff using the data of all calibrator scans combined. Geometric feed rotation angles are corrected for on the fly, following the measurement equation, and no relative complex gains are corrected in the CASA data. We commonly refer to the calibrated data produced by the rPICARD pipeline as "CASA" data.

The EHT VLBI data indicate a phase offset (either constant or with a time-dependent drift component) between the two polarization channels that can be attributed largely to instrumental effects, and in a small part to circular polarization (Stokes $\mathcal{V}$) of the source. The instrumental phase shifts are corrected through polarimetric gain ratio calibration, aligning RR and LL components to compute the total-intensity

[162] This position for Sgr A* is also adopted in the MWL analysis that follows.

(Stokes $\mathcal{I}$) visibilities coherently. Leveraging the facts that the RCP−LCP instrumental phase of ALMA after PolConvert is zero (Martí-Vidal et al. 2016; Goddi et al. 2019) and that intrinsic Stokes $\mathcal{V}$ signals will have a negligible phase contribution on ALMA baselines, the parallel hand signals have been aligned for each VLBI scan under the assumption of $\mathcal{V} = 0$ on ALMA baselines. The same strategy is also employed inherently by rPICARD, as the parallel correlation products are fringe-fitted separately. As the phase calibration is station based, intrinsic Stokes $\mathcal{V}$ signals are not removed from the data. More details about the EHT data reduction pipelines, including flowcharts of their processing steps, and detailed verification tests are given in M87* Paper III.[163]

Due to the excellent sensitivity of the EHT, we have a high S/N on many baselines probing Sgr A*, which allows us to model atmospheric phase fluctuations occurring on short timescales to effectively extend the coherence time (M87* Paper III). Combined with the small field of view around the VLBI correlation phase center of the EHT, this means that reasonable averaging intervals are limited primarily by the spectral and temporal variations of the target. With a fractional bandwidth of $\sim 1\%$, we can safely average the data over our observing bandpass without introducing considerable bandwidth smearing effects (Thompson et al. 2017). On the other hand, Sgr A* is known to vary on very short timescales, possibly down to the gravitational timescale, $GMc^{-3} \approx 21$ s. We have therefore chosen to average our data, which was correlated with a 0.4 s period, into 10 s time bins.

3.2. Flux Density Scaling

To scale our correlation coefficient measurements to a physical flux density unit scale, we estimate the system equivalent flux density (SEFD) of every station in the array. The SEFD of a single antenna or phased-up array is given as

$$\mathrm{SEFD} = \frac{T_{\mathrm{sys}}^{*}}{\eta_{\mathrm{ph}}\ \mathrm{gc}(E)\ \mathrm{DPFU}}. \quad (1)$$

Here T_{sys}^{*} is the effective system temperature, which characterizes the total noise contribution along a station's signal path and corrects for the signal attenuation caused by Earth's atmosphere. The phasing efficiency of a phased array is given by η_{ph}, which is unity for single-dish stations. The station gain is factored into a normalized elevation (E) gain curve gc(E) and the "degrees-per-flux-unit" (DPFU) conversion factor between measured system temperatures and flux densities. The DPFU is determined by the aperture efficiency η_{ap} and total collecting area A_{geom} as $\mathrm{DPFU} = \eta_{\mathrm{ap}} A_{\mathrm{geom}}/(2k_{\mathrm{B}})$, with k_{B} the Boltzmann constant. We can scale a correlation coefficient r_{i-j} measured on a baseline $i-j$ in units of thermal noise to a visibility V_{i-j} in units of Jy via

$$V_{i-j} = \sqrt{\mathrm{SEFD}_i \mathrm{SEFD}_j}\, r_{i-j}. \quad (2)$$

We have performed this flux density calibration with a common framework[164] for both the CASA and HOPS data.

[163] Note that the M87* HOPS data presented in M87* Paper III were obtained with multisource, multiday calibration of the polarimetric gain ratios (Steel et al. 2019). While the aim of this method was to preserve the Stokes $\mathcal{V}$ structure of the resolved images, it indicated underfitting of the instrumental effects, potentially increasing the resulting systematic errors.

[164] https://github.com/sao-eht/eat

Table 1
Fitted LMT Gains on Each EHT Observing Day

UTC Day (2017 Apr.)	RCP DPFU (Jy K^{-1})	LCP DPFU (Jy K^{-1})
05	0.046 ± 0.003	0.048 ± 0.003
06	0.032 ± 0.009	0.034 ± 0.009
07	0.061 ± 0.001	0.064 ± 0.001
10	0.076 ± 0.001	0.077 ± 0.001
11	0.067 ± 0.005	0.067 ± 0.004

Compared to the SEFDs used to calibrate the data released for M87* and 3C 279 (M87* Paper III), we have updated several a priori calibration parameters. We are using the Butler (2012) planet models (updated for the year 2017) for the gain calibration of the APEX, PV, and SMT telescopes, instead of the previously used GILDAS[165] models. Additionally, we have used 10.″1 instead of 8.″5 as an updated estimate for the beam size of the LMT and subsequently fitted for the variable station gain on a per-day basis (Table 1).

Data from SMA were reanalyzed, using the intra-SMA interferometric data to derive new SEFD estimates for the phased-array data. Aperture efficiencies were calculated using observations of the solar system objects Callisto, Ganymede, and Titan and the brightness temperature models from Butler (2012) and derived separately for low and high band. Amplitude gain solutions were derived using two quasars—NRAO 530 and J1924−2914—that were observed periodically during the observations of Sgr A*. Phase-only self-calibration was applied to the SMA interferometer data of Sgr A*, assuming a point-source model and excluding baselines shorter than 15 kλ in length, due to the presence of large-scale emission features. The resultant gain solutions were used to rederive phasing efficiencies for the beamformed data used for VLBI analysis. More details about the SMA data reduction are given in Wielgus et al. (2022, Section 2.3).

Typical SEFDs used to calibrate the Sgr A* flux density are shown in Figure 3. For the time-averaged SED data gathered in Table 2, we calculate a flux density of 2.4 ± 0.2 Jy between 213 and 229 GHz.

3.2.1. Light Curves of Sgr A* and ALMA-VLBI Amplitude Calibration

The ALMA Phasing System is designed to construct a summed, formatted VLBI signal without interrupting the data stream of each individual antenna, thus allowing the ALMA correlator to compute all of the intra-ALMA visibilities at the same time (Matthews et al. 2018). The calibration information related to these intra-ALMA visibilities is needed for the correct polarimetric processing of the ALMA-VLBI signal (Martí-Vidal et al. 2016; Goddi et al. 2019, 2021).

At the spatial scales sampled by the intra-ALMA baselines, the Sgr A* field consists of the sum of two components: a point-like source located at the field center and with a time-dependent flux density (i.e., the active galactic nucleus), and an extended structure that covers several arcseconds, with a total flux of about 1.1 Jy and a surface brightness of about 0.12 Jy beam^{-1} (Wielgus et al. 2022). This extended component is known as the "minispiral," and its emission is related to ionized gas and dust in the Galactic center (e.g., Lo & Claussen 1983).

[165] http://www.iram.fr/IRAMFR/GILDAS

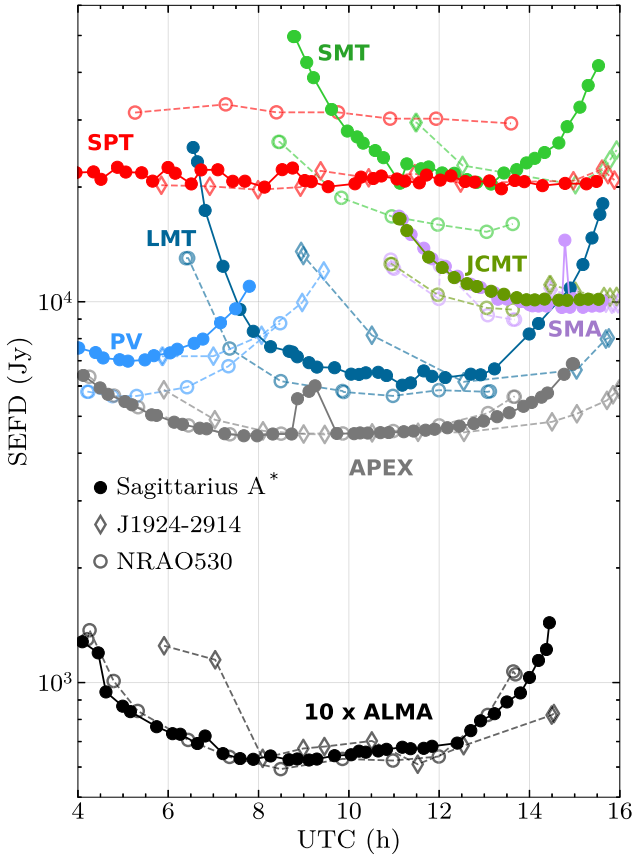

Figure 3. Example of SEFD values during a single night of the 2017 EHT observations (2017 April 7, high-band RCP). Values for Sgr A* are marked with filled circles, values for J1924−2914 are marked with open diamonds, and values for NRAO 530 are marked with open circles. ALMA SEFDs have been multiplied by 10 in this plot for visualization purposes.

The use of the intra-ALMA self-calibration gains to compute the corrections for the VLBI amplitudes of the ALMA-related baselines provides a very accurate determination of the relative changes in ALMA's VLBI amplitude gains (Goddi et al. 2019). However, this approach has important limitations for the correct calibration of a time-variable source like Sgr A* (see also Section 4). In particular, the use of an a priori (constant) model for the amplitude self-calibration of the Sgr A* intra-ALMA visibilities results in an incorrect estimate of the phased-ALMA amplitude scaling. To overcome this limitation, we calibrate the Sgr A* ALMA gains with the source's light curve, which is computed under the assumption that the flux density distribution of the minispiral remains stable across the extent of the observations (Wielgus et al. 2022).

We note that, even though the minispiral modeling allows us to calibrate relative ALMA gains at the $\sim 1\%$ level, a constant $\sim 10\%$ calibration uncertainty remains for the overall gain of the phased array, which is tied to the estimated flux density of Ganymede (the source used as primary calibrator; Goddi et al. 2019).

We perform a time-dependent variant of the network calibration (M87* Paper III) of the EHT VLBI data to a merged light curve from ALMA and the SMA (presented alongside the MWL light curves in Section 4). The ALMA light curve is computed through the minispiral method described above, and a description of the SMA light curve is given in Wielgus et al. (2022). These show small offsets at the level of a few percent between the two raw light curves, within the absolute flux calibration uncertainty. The two light curves are combined by leveling the median amplitudes in the overlapping time between ALMA and SMA and a smoothing spline interpolation in time, which corrects for these offsets. The network calibration procedure leverages the presence of colocated sites, constraining gains of telescopes with a colocated partner by assuming that intrasite baselines (ALMA–APEX and JCMT–SMA; see Figure 1) observe a point source with a time-dependent flux density, corresponding to the light curve.

3.2.2. Calibrator Gain Transfer

Ensembles of opacity-corrected antenna temperature (T_a^*) measurements are used to fit for gain curves and DPFUs (Janssen et al. 2019a; Issaoun et al. 2017). For the gain curve, we fit

$$\mathrm{gc}(E) = 1 - B(E - E_0)^2 \tag{3}$$

to normalized T_a^* values from quasars tracked over a wide range of elevations E. The parameters B and E_0 describe the peak and shape of the gain curve, respectively. For the DPFU, we typically fit a constant value for the entire observing track to T_a^* measurements of solar system objects to estimate the constant aperture efficiency η_{ap}. A statistical T_a^* scatter translates into uncertainties of the fitted B, E_0, and η_{ap} parameters of the gain curve and DPFU, respectively. The uncertainty of the planet model brightness temperature is added in quadrature for the DPFU fitting. For the Butler (2012) models, we have a 10% uncertainty for Saturn and 5% for Mars, Jupiter, and Uranus. The error contribution from T_{sys}^* measurements is negligible. Finally, ALMA and SMA exhibit an additional calibration uncertainty from the phasing efficiency. The performance of ALMA has been determined in the quality assurance stage 2 (QA2) ALMA interferometric reduction of data (Goddi et al. 2019). The final calibration method is described in Section 3.2.1, for which we have estimated a global 10% flux density calibration uncertainty. The small SMA dishes are well characterized. Here the phasing efficiency dominates the overall calibration uncertainty, which ranges between 5% in optimal observing conditions and 15% when the phasing efficiency is low. The a priori flux calibration parameters are summarized in Table 3. The reported uncertainties provide a good upper limit for residual gain errors. Compared to our 2017 M87* data (M87* Paper III), the DPFU values are slightly updated, which does not affect our previous results, while the gain curves stayed the same.

However, there are several loss factors that are not captured in our a priori calibration framework, most notably imperfect pointing and focus solutions of individual telescopes. The case is most severe for the large LMT dish, where the measured DPFU varies from day to day. In order to provide a conservative estimate of the gain uncertainties, a bootstrap approach was applied to the DPFU measurements on 2017 April 6 and 7. With 10,000 medians drawn from the bootstrapped samples, we are able to derive the median absolute deviation, which is then scaled to an equivalent sigma. With this method we find a $\sim 35\%$ uncertainty on the LMT DPFU.

Table 2
Values for the Sgr A* SED Observed by Coordinated Ground-based and Space-based Observatories during the EHT 2017 Run

Observatory	Frequency (GHz)	νF_ν ($\times 10^{-12}$ erg s^{-1} cm^{-2})	Flux (Jy)	νL_ν ($\times 10^{34}$ erg s^{-1})
EAVN	22	0.24 ± 0.02	1.07 ± 0.11	0.19 ± 0.02
EAVN	43	0.58 ± 0.06	1.35 ± 0.14	0.48 ± 0.05
GMVA	86	1.63 ± 0.17	1.9 ± 0.2	1.3 ± 0.1
GMVA	88	1.67 ± 0.18	1.9 ± 0.2	1.4 ± 0.1
GMVA	98	1.96 ± 0.20	2.0 ± 0.2	1.6 ± 0.2
GMVA	100	2.10 ± 0.20	2.1 ± 0.2	1.67 ± 0.2
ALMA/SMA[a]	213–229	5.28 ± 0.44	2.4 ± 0.2	4.3 ± 0.4
VLT	1.38×10^5	<4.12	<0.003	<3.4
Chandra/NuSTAR	5.68×10^8	$0.70^{+0.15}_{-0.20}$	$1.23^{+0.27}_{-0.35} \times 10^{-7}$	$0.57^{+0.13}_{-0.16}$
Chandra/NuSTAR	7.84×10^8	$0.49^{+0.06}_{-0.11}$	$6.27^{+0.74}_{-1.40} \times 10^{-8}$	$0.40^{+0.05}_{-0.09}$
Chandra/NuSTAR	1.08×10^9	$0.33^{+0.01}_{-0.05}$	$3.09^{+0.11}_{-0.46} \times 10^{-8}$	$0.27^{+0.01}_{-0.04}$
Chandra/NuSTAR	1.49×10^9	$0.25^{+0.25}_{-0.04}$	$1.71^{+1.71}_{-0.25} \times 10^{-8}$	$0.21^{+0.21}_{-0.03}$
Chandra/NuSTAR	2.06×10^9	$0.08^{+0.09}_{-0.02}$	$0.39^{+0.43}_{-0.11} \times 10^{-8}$	$0.06^{+0.07}_{-0.02}$
Chandra[b]	1.57×10^9	$5.63^{+5.06}_{-3.36}$	$3.6^{+3.2}_{-2.1} \times 10^{-7}$	$4.61^{+4.15}_{-2.76}$
NuSTAR[b]	9.55×10^9	$0.78^{+0.86}_{-0.73}$	$8.3^{+9.0}_{-7.6} \times 10^{-9}$	$0.64^{+0.70}_{-0.60}$

Notes. Frequencies for X-ray observatories reflect the central frequency of the keV energy band within the observation bin.
[a] Mean measurement across 213–229 GHz. The spectral index at these frequencies was observed to be close to zero (Wielgus et al. 2022).
[b] 2017 April 11 X-ray flare.

Table 3
EHT Flux Density Calibration Parameters and Their Uncertainties

Station(Code)	RCP DPFU (K Jy^{-1})	LCP DPFU (K Jy^{-1})	B	E_0
ALMA(AA)[a]	$1.03 \pm 10\%$	$1.03 \pm 10\%$	0	0
APEX(AP)	$0.0245 \pm 11\%$	$0.0250 \pm 11\%$	$0.00002 \pm 3.6\%$	$36.6 \pm 1\%$
IRAM 30 m(PV)[b]	$0.034 \pm 10\%$	$0.033 \pm 10\%$	$0.00018 \pm 5.3\%$	$43.7 \pm 1.3\%$
JCMT(JC)[c]	$(0.026 \pm 14\%)$–$(0.033 \pm 11\%)$	$(0.026 \pm 14\%)$–$(0.033 \pm 11\%)$	0	0
LMT(LM)[d]	$0.061 \pm 35\%$	$0.064 \pm 35\%$	0	0
SMA(SM)[e]	$0.046 \pm (5$–$15)\%$	$0.046 \pm (5$–$15)\%$	0	0
SMT(AZ)	$0.01683 \pm 7\%$	$0.01681 \pm 7\%$	$0.000082 \pm 10.4\%$	$57.6 \pm 2.0\%$
SPT(SP)[f]	$0.0061 \pm 15\%$	$0.0061 \pm 15\%$	0	0

Notes. For phased arrays (ALMA and SMA), the DPFUs represent the combined sensitivity of all phased dishes. The gain curve parameters as a function of elevation E are given based on a $\mathrm{gc}(E) = 1 - B(E - E_0)^2$ parameterization (Equation (3)).
[a] The ALMA DPFU uncertainty is based on the overall 10% uncertainty estimated by the QA2 team.
[b] The PV DPFU has been scaled down by a factor of 3.663 to account for the known maser instability in 2017.
[c] For the JCMT DPFU, a range between the smallest daytime value and the nighttime value is given.
[d] The LMT has an unparameterized 10% uncertainty on the gain curve, which has been added to the DPFU uncertainty. The DPFU values shown here are from 2017 April 7. The uncertainty is the most conservative value from April 6.
[e] The SMA DPFU uncertainty is based on the dominant 5%–15% uncertainty on the phasing efficiency.
[f] The gain curve of the SPT is uncharacterized, as normalized antenna temperature values cannot be obtained from sources that remain at a constant elevation when observed from the South Pole.

Additionally, the antenna gains can be characterized by amplitude self-calibration, which solves the empirical corrections for time-variable instrumental or environmental factors that cannot be measured directly. In order to avoid any variability from Sgr A* that could contaminate the antenna gain estimations, the scan-averaged visibility data of calibrators (J1924−2914 and NRAO 530) are utilized by assuming their stationarity in both source structure and flux density. For both calibrators, the fiducial images independently produced with different imaging pipelines (i.e., eht-imaging, SMILI, Difmap and DMC; Papers III and IV) are employed to improve the statistics on the gains (for more details, see S. Jorstad et al. 2022, in preparation; S. Issaoun et al. 2022, in preparation). We use the mean values of the gains obtained from each imaging pipeline. As an example, the resultant antenna gains derived by amplitude self-calibration for the low-band data sets for both calibrators are shown in Figure 4. The results were obtained after performing a gain alignment procedure meant to minimize the offset between the gains from the two calibrators within the overlapping time and flagging the data points lying beyond 3σ from the mean value. The procedure is as follows: (1) we first derive a mean gain value for each calibrator by only using the gains in the overlapping times; (2) from these gain mean values for the two calibrators, in the overlapping times, we derive an average gain value and rescale the two calibrators' mean gains with this average value; (3) the scaling factors thus obtained are then applied to the gains over the entire time range. The mean gains for each station (reported on top of each panel in

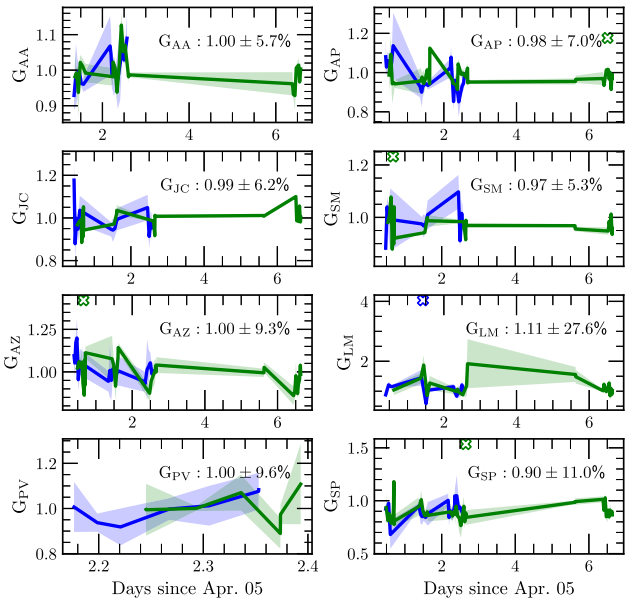

Figure 4. Low-band antenna gains of NRAO 530 (blue curve) and J1924 −2914 (green curve) by amplitude self-calibration. The two-letter station codes are taken from Table 3. The colored bands indicate 1σ uncertainties of the gains. The open cross symbols represent the flagged data points lying beyond 3σ from the mean value. The PV telescope observed Sgr A* only on April 7.

Figure 4) are within their corresponding a priori DPFU error budgets (Table 3). We can therefore assume that the calibrator self-calibration method captures the known gain uncertainties that enter into our a priori flux density calibration error budget. At this point, we linearly interpolate the fiducial gains obtained from the calibrators to the Sgr A* time stamps and apply them to the Sgr A* data.

3.3. Systematic Error Budget

We compute $S/N > 7$ closure phases (ψ_C) and log closure amplitudes ($\ln A_C$), which are reasonably well described by a normal distribution (Blackburn et al. 2020), to estimate the amount of systematic noise s present in the EHT data following M87* Paper III and Wielgus et al. (2019). We have augmented these "traditional" closure phases and closure amplitude tests with novel closure trace quantities, $\mathcal{T}$, described in Broderick & Pesce (2020). Closure traces are complex composite data structures, which we characterize by their phase and log amplitude. The closure traces are produced from parallel- and cross-hand correlation products, and they are insensitive to all linear station-based corruptions of the data, including both station gains and polarization leakage. The uncertainty σ_x of a data product X follows from the a priori estimated thermal noise $\sigma_{\rm th}$ from our calibration pipelines and a constant systematic nonclosing error s_x as

$$\sigma_x^2 = \sigma_{\rm th}^2 + s_x^2. \quad (4)$$

We estimate s_x based on the criterion that the median absolute deviation of X/σ_x becomes unity for the following data quantities:

1. RR − LL closure phases ($X = \psi_{\rm C,\ RR} - \psi_{\rm C,\ LL}$) and log closure amplitudes ($X = \ln A_{\rm C,\ RR} - \ln A_{\rm C,\ LL}$), which should be zero in the absence of significant circular source polarization and instrumental polarization leakage.
2. Low-band − high-band closure phases ($X = \psi_{\rm C,\ lo} - \psi_{\rm C,hi}$, log closure amplitudes ($X = \ln A_{\rm C,\ lo} - \ln A_{\rm C,\ hi}$), closure trace phases ($X = \arg(\mathcal{T}_{\rm lo}) - \arg(\mathcal{T}_{\rm hi})$), and log closure trace amplitudes ($X = \ln|\mathcal{T}_{\rm lo}| - \ln|\mathcal{T}_{\rm hi}|$), all of which should be close to zero in the absence of significant variations of source structure and flux over the observed EHT bandwidth. The phase shift due to the small frequency difference between the two bands is negligible.
3. Closure phases of small, trivial triangles ($X = \psi_{\rm C,trivial}$) and log closure amplitudes of small, trivial quadrangles ($X = \ln A_{\rm C,trivial}$), which should be zero in the absence of significant instrumental polarization leakage as they probe the symmetric large-scale source structure. Additionally, trivial closure phases will be affected by large-scale source structures.
4. Closure trace phases ($X = \arg(\mathcal{T}_{\rm trivial})$) and closure trace log amplitudes ($X = \ln|\mathcal{T}_{\rm trivial}|$) on trivial boomerang quadrangles, in which a site is repeated so that the area of the quadrangle vanishes. Both sets of quantities should be zero in the absence of nonlinear station-based or baseline-based errors.

We studied the magnitude of systematic error budgets on different coherent averaging timescales and found the systematics to be minimized for a time-averaging of 120 s. At shorter times, low-S/N biases occur. At longer times, decoherence from residual atmospheric phase turbulence becomes pronounced. Therefore, we construct all closure quantities X from visibilities that have been coherently averaged over 120 s and apply the $S/N > 7$ threshold; we subsequently average the constructed closure traces on scan-length intervals.

The systematic error budgets derived for Sgr A*, NRAO 530, and J1924−2914 are shown in Table 4. These are estimated using only data on days when ALMA was observing, i.e., 2017 April 6, 7, and 11. However, we exclude Sgr A* data from 2017 April 11 owing to flaring activity—these will be the subject of a forthcoming study (see also Wielgus et al. 2022). The underlying distributions of the various data quantities, with and without added systematic error, are shown in Figure 5.

From the combined data on all baselines, an excess in systematic errors of RR − LL closure quantities can be seen for Sgr A* compared to the observed NRAO 530 and J1924−291 calibrator sources. These offsets may be indicative of intrinsic source polarization in Sgr A*. However, the overall offsets are just at the level of thermal noise for scan-averaged data. It is likely for source polarization to be significant on particular baselines only. Horizon-scale polarization signatures in the 2017 Sgr A* EHT data will be analyzed in future work.

The systematic error budgets agree between the traditional closure quantities and the novel closure traces. It is therefore unlikely for large-scale source structure and uncorrected polarization leakage effects to be the dominant sources of systematic uncertainties.

There are several EHT data issues affecting Sgr A* observations that require special care. These are described in detail in M87* Paper III and briefly summarized below.

1. The JCMT and SMA used an identical frequency setup derived from a shared frequency standard in 2017. Radio frequency interference (RFI) is not washed out due to low fringe rate. Both stations are therefore never chosen as the reference station for the correction of atmospheric phase

Table 4
Nonclosing Systematic Uncertainties, s (and in Units of Thermal Noise, $s/\sigma_{\rm th}$), for Sgr A* and Its Calibrators Estimated Using Various Statistical Tests on Both the CASA and HOPS Products

Source	Test	CASA			HOPS		
		s	$s/\sigma_{\rm th}$	n	s	$s/\sigma_{\rm th}$	n
Sgr A*	RR − LL closure phases	3.°6	0.6	313	3.°6	0.6	328
	lo − hi closure phases	2.°1	0.3	333	2.°0	0.3	367
	trivial closure phases	0.°2	0.1	373	1.°0	0.2	411
	RR − LL log closure amplitudes	10.9%	0.8	239	11.3%	0.9	278
	lo − hi log closure amplitudes	9.7%	0.6	284	7.6%	0.5	371
	trivial log closure amplitudes	5.6%	0.5	168	1.4%	0.1	212
	lo − hi closure trace phases	1.°1	0.2	97	0.°0	0.0	125
	trivial closure trace phases	1.°5	0.3	160	0.°0	0.0	158
	lo − hi log closure trace amplitudes	3.7%	0.4	97	0.0%	0.0	125
	trivial log closure trace amplitudes	5.7%	0.6	160	4.6%	0.5	158
NRAO 530	RR − LL closure phases	1.°4	0.2	125	0.°0	0.0	121
	lo − hi closure phases	2.°5	0.3	156	2.°8	0.3	150
	trivial closure phases	0.°0	0.0	151	0.°0	0.0	147
	RR − LL log closure amplitudes	0.4%	0.0	114	0.0%	0.0	117
	lo − hi log closure amplitudes	0.0%	0.0	203	2.7%	0.1	188
	trivial log closure amplitudes	6.2%	0.6	100	3.2%	0.3	91
	lo − hi closure trace phases	1.°3	0.2	56	0.°0	0.0	54
	trivial closure trace phases	0.°0	0.0	104	0.°0	0.0	95
	lo − hi log closure trace amplitudes	5.6%	0.5	56	8.5%	0.8	54
	trivial log closure trace amplitudes	2.1%	0.2	104	0.0%	0.0	95
J1924−2914	RR − LL closure phases	2.°4	0.5	207	2.°6	0.5	235
	lo − hi closure phases	1.°1	0.2	224	0.°9	0.2	280
	trivial closure phases	0.°5	0.2	190	0.°0	0.0	204
	RR − LL log closure amplitudes	2.0%	0.2	272	3.5%	0.3	313
	lo − hi log closure amplitudes	6.6%	0.6	367	6.8%	0.7	455
	trivial log closure amplitudes	3.7%	0.5	190	4.2%	0.6	218
	lo − hi closure trace phases	2.°3	0.5	222	1.°3	0.3	253
	trivial closure trace phases	2.°2	0.8	106	1.°9	0.7	106
	lo − hi log closure trace amplitudes	5.5%	0.7	222	6.4%	0.8	253
	trivial log closure trace amplitudes	0.0%	0.0	106	2.6%	0.5	106

Note. The data from April 6 and 7 have been used for Sgr A*, and for the calibrators we have also used April 11. n is the number of closure quantities used for each test.

fluctuations. Resultant amplitude errors on this baseline are mostly mitigated by flagging channels affected by RFI and network calibration.

2. An instability in the maser used in 2017 for PV caused a decorrelation over the 0.4 s correlator accumulation period, which was corrected by up-scaling the SEFD.
3. Partial data dropouts due to a misconfigured Mark 6 recorder at APEX have been accounted for by adjusting the amplitudes and data weights accordingly during correlation. A hard drive failure at the JCMT, causing 1/16 of the low-band data to be lost, has been similarly corrected. Furthermore, a small SEFD correction factor has been applied to the APEX data to correct for an amplitude loss from an interfering one-pulse-per-second signal.
4. High-band SMA SEFDs on the first three observing days have been up-scaled to correct for occasionally corrupted frequency channels in the beamformer system.
5. A negligible <0.1% amplitude loss due to a periodic ALMA correlator glitch occurring every 18.192 s was left uncorrected. Moreover, a baseline-dependent ∼0.67% signal loss due to finite fast Fourier transform lengths over the full 2048 MHz band on non-ALMA baselines has not been corrected.

The systematic error studies presented in Figure 5 and Table 4 reflect a comparable level of data quality and internal self-consistency for the CASA and HOPS data products. All data distributions are well behaved, and the different amounts of estimated systematic noise are balanced, being sometimes higher in one or the other data set. Small differences in the number of recorded visibilities are due to the effects of thresholding near the detection limit, as well as slight differences in flagging between the two pipelines.

As indicated also by the scatter in the s measurements, optimal systematic error budgets depend on the exact baselines and data quantities used. A crude recommendation for data averaged in 120 s bins is to adopt 2.°5 for closure phases and 9% for log closure amplitudes.

4. Multiwavelength Observing Campaign

In addition to the ALMA and SMA millimeter light curves collected as a part of the EHT observations (Figure 6; see also Wielgus et al. 2022), the 2017 Sgr A* EHT campaign includes observations from elite ground-based facilities (Section 4.1),

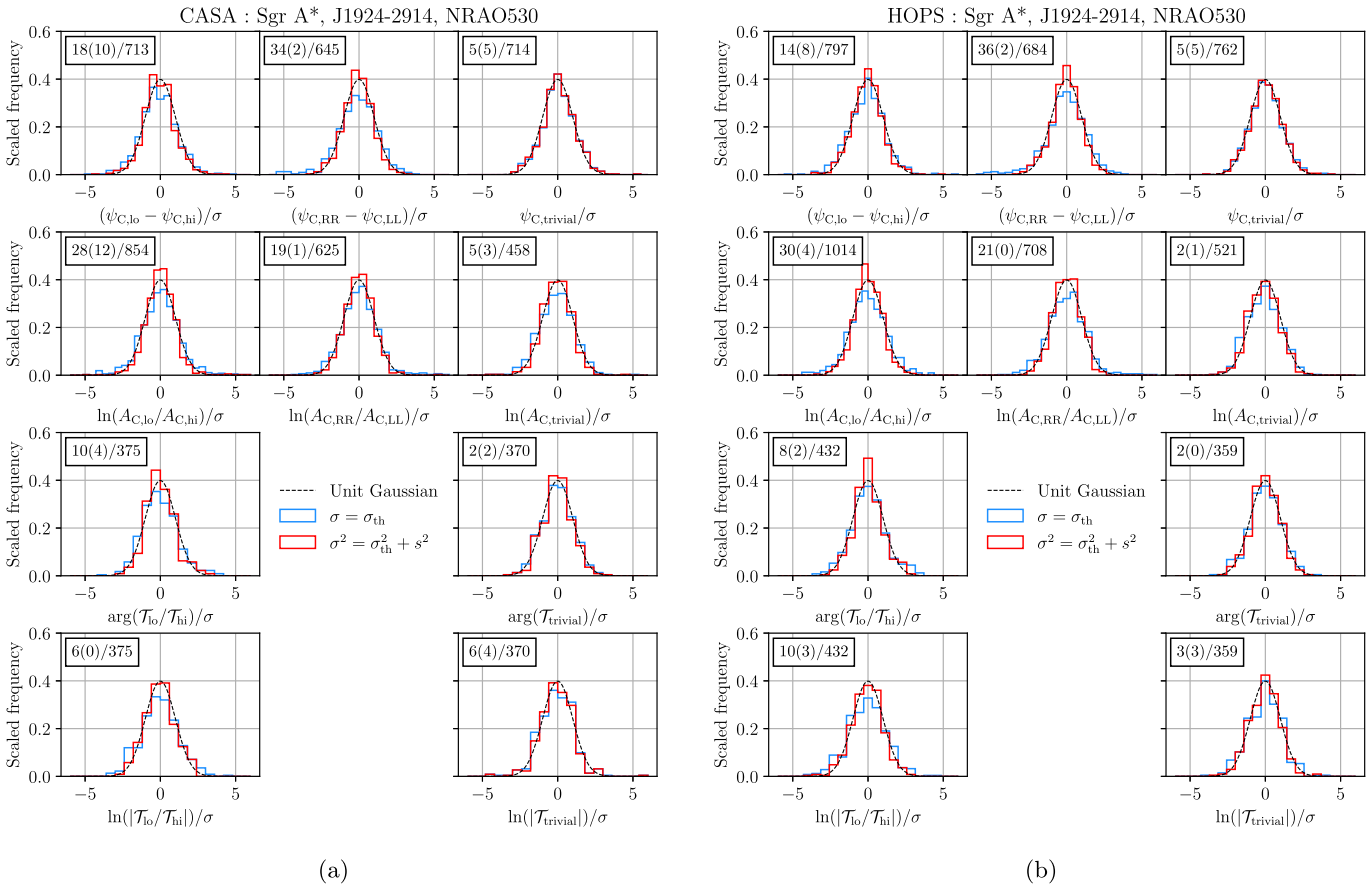

Figure 5. Normalized distributions of lo−hi, RR−LL, and trivial closure quantities, as well as lo−hi and trivial closure trace quantities of Sgr A*, NRAO 530, and J1924−2914 from both the (a) CASA and (b) HOPS reduction pipelines. The data from April 6 and 7 have been used for Sgr A*, and for the calibrators we have also used April 11. The distributions prior to (blue) and after (red) accounting for the estimated systematic uncertainties, s, are shown. The values of s for each source and reduction pipeline are given in Table 4. In the top left corner of each distribution, the number of $>3\sigma$ outliers is given considering thermal noise only, followed by the number of outliers considering thermal plus systematic noise for σ in parentheses. These numbers are followed by the total number of data points after a slash.

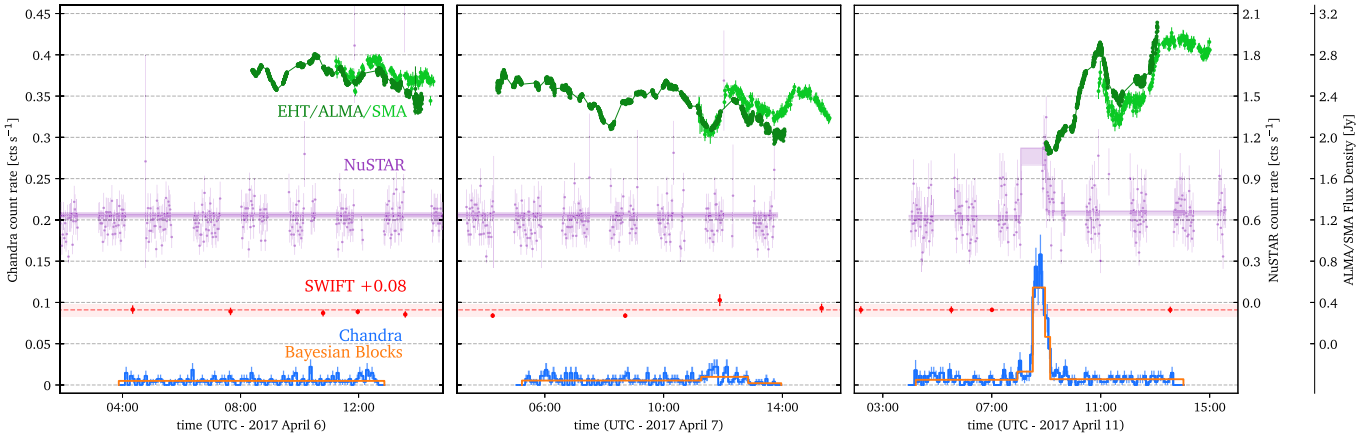

Figure 6. Light curves from ALMA at a 4 s cadence and SMA at a 62 s cadence at 229 GHz (dark- and light-green points, respectively; see Wielgus et al. 2022, for details), along with (quasi-)simultaneous, coordinated Swift (red; 2–10 keV), Chandra (blue; 2–8 keV), and NuSTAR (purple; 3–79 keV) observations on 2017 April 6, 7, and 11. The long-term average flux value of Sgr A* measured from Swift is plotted as a red dashed line with upper and lower 2σ percentiles for the 2017 cumulative flux distribution marked with a light-red shaded region (e.g., Degenaar et al. 2013, 2015). The Bayesian block flare detection algorithm (Scargle 1998; Scargle et al. 2013; Williams et al. 2017) has been run on the Chandra and NuSTAR light curves, and results, including flare detections on April 7 and 11, are overplotted as orange histograms on the Chandra data and purple histograms on the NuSTAR data.

including the East Asian VLBI Network, the Global 3 mm VLBI Array, and the Very Large Telescope, as well as space-based telescopes (Section 4.2) including the Neil Gehrels Swift Observatory, the Chandra X-ray Observatory, and the Nuclear Spectroscopic Telescope. Figure 2 shows coverage of Sgr A* for each of these instruments during the campaign. These coordinated observations provide (quasi-)simultaneous wavelength coverage and enable detailed MWL variability studies that place broadband constraints on models (see Papers V and VI). We describe these observations briefly here and place

them in the broader EHT and Sgr A* historical context in Section 5.2.

4.1. Supplementary Ground-based Observations

4.1.1. East Asian VLBI Network

The East Asian VLBI Network (EAVN; e.g., Wajima et al. 2016; An et al. 2018; Cui et al. 2021) consists of the seven telescopes of KaVA (KVN[166] and VERA[167] Array; e.g., Lee et al. 2014; Niinuma et al. 2015), and additional telescopes of the Japanese VLBI Network (JVN; e.g., Doi et al. 2006) and the Chinese VLBI Network (CVN; e.g., Zheng 2015). During the EHT 2017 window, four EAVN observations were carried out at 22 and 43 GHz (Figure 2). A single, symmetric Gaussian model was found to describe the intrinsic structure of Sgr A* at both wavelengths. The measured flux densities from Sgr A* at these frequencies are 1.07 ± 0.11 Jy and 1.35 ± 0.14 Jy, respectively (Table 2). Two of the observations on 2017 April 3 and 4 are (quasi-)simultaneous with the Global 3 mm VLBI Array observations (Section 4.1.2), as well as the EHT sessions (Cho et al. 2022). These measurements provide an estimated size and flux density of Sgr A* at 1.3 mm via extrapolation of power-law models (i.e., the intrinsic size scales with observing wavelength as a power law with an index of $\sim 1.2 \pm 0.2$).

4.1.2. Global 3 mm VLBI Array

VLBI observations of Sgr A* at 86 GHz were conducted on 2017 April 3 with the Global Millimeter VLBI Array (GMVA).[168] Eight Very Long Baseline Array antennas equipped with 86 GHz receivers, the Robert C. Byrd Green Bank Telescope (GBT), the Yebes 40 m telescope, the Effelsberg 100 m telescope, PV, and 37 phased-ALMA antennas participated in the observation (project code MB007, published in Issaoun et al. 2019b).

The data were recorded with a bandwidth of 256 MHz for each polarization, and fringes were detected out to 2.3 Gλ. The total on-source integration time on Sgr A* was 5.76 hr over a 12 hr track, with ALMA co-observing for 8 hr. The results of the experiment rule out jet-dominated radio emission models of Sgr A* with large viewing angles ($> 20°$) and provide stringent constraints on the amount of refractive noise added by the interstellar scattering screen toward the source (Issaoun et al. 2019b), discussed in more detail in Section 5.1.2. The total flux density measured at 86 GHz is 1.9 ± 0.2 Jy (Table 2).

4.1.3. Very Large Telescope

The Paranal Observatory's Nasmyth Adaptive Optics System (NAOS) and Near-Infrared Imager and Spectrograph (CONICA) instrument on the VLT, also known as VLT/NACO, measured a *K*-band NIR upper limit of 3 mJy during the 2017 April 7 EHT observing run (courtesy of the MPE Galactic Center Team). Ongoing observations with the new Very Large Telescope Interferometer GRAVITY instrument (VLTI/GRAVITY; Gravity Collaboration et al. 2017) indicate that Sgr A*'s typical flux distribution in the NIR *K* band changes slope at a median flux density of 1.1 ± 0.3 mJy, characteristic of Sgr A*'s quiescent NIR emission (Gravity Collaboration et al. 2020).

4.2. Coordinated Space-based Observations

4.2.1. Neil Gehrels Swift Observatory

Observations from the Swift X-ray Telescope (XRT; Gehrels et al. 2004; Burrows et al. 2005) were reprocessed with the latest calibration database files and the Swift tools contained in HEASOFT-v6.20.footnote https://heasarc.gsfc.nasa.gov/lheasoft/. Source flux in the 2–10 keV energy band is extracted from a 10″-radius circular region centered on the position of Sgr A*. Count rates are reported as measured (e.g., Degenaar et al. 2013), i.e., without any correction for the known significant absorption along the Sgr A* sight line ($N_{\rm H} \sim 9 \times 10^{22}$ cm^{-2}).

There are 48 Swift observations of the Galactic center between 2017 April 5 and 12, with a total exposure time of 26.3 ks (Figure 2). These observations include a dedicated dense sampling schedule to coincide with the EHT observing window and two observations from the regular Galactic center monitoring program (Degenaar et al. 2013, 2015; van den Eijnden 2021). The average exposure time of the dense sampling was ~500 s, with an average interval between observations of ~3.5 hr.

In the 2017 April 7 Swift observation that overlaps the EHT window (Figure 6), a 2–10 keV flux is detected (0.023 counts s^{-1}) in excess of the 2017 2σ trend line (0.018 counts s^{-1}), as measured from the cumulative flux distribution observed from Sgr A*. None of the Swift observations are simultaneous with the 2017 April 11 Chandra flare described in the following section.

4.2.2. Chandra X-Ray Observatory

A series of Chandra X-ray Observatory (Weisskopf et al. 2002) exposures of Sgr A* were acquired on 2017 April 6, 7, 11, and 12 using the ACIS-S3 chip in FAINT mode with a 1/8 subarray (observations IDs 19726, 19727, 20041, 20040; PI: Garmire), for a total of ~133 ks coordinated with the EHT campaign (Figure 2). The small subarray mitigates photon pileup during bright Sgr A* flares, as well as contamination from the magnetar SGR J1745−2900, which peaked at X-ray wavelengths in 2013 and has faded over the more than 6 yr since (Mori et al. 2013; Rea et al. 2013, 2020; Coti Zelati et al. 2015, 2017). It also achieves a frame rate of 0.44 s versus Chandra's standard rate of 3.2 s.

Chandra data reduction and analysis are performed with the CIAO v4.13 package[169] (Fruscione et al. 2006), CALDB v4.9.4. We use the `chandra_repro` script to reprocess the level 2 events files, update the WCS coordinate system (`wcs_update`), and apply barycentric corrections to the event times (`axbary`). The 2–8 keV light curves are then extracted from a circular region of radius 1.″25 centered on the radio position of Sgr A*. Light curves for 2017 April 6, 7, and 11 are shown in Figure 6. Using the Bayesian Blocks algorithm (Scargle 1998; Scargle et al. 2013; Williams et al. 2017), we search these light curves for flares and robustly detect one on 2017 April 11, with a second weaker detection on April 7 (orange histograms overplotted on the Chandra light curves in Figure 6).

[166] Korean VLBI Network: three 21 m telescopes in Korea (Yonsei, Ulsan, and Tamna).
[167] VLBI Exploration of Radio Astrometry: four 20 m telescopes in Japan (Mizusawa, Iriki, Ogasawara, and Ishigakijima).
[168] https://www3.mpifr-bonn.mpg.de/div/vlbi/globalmm/
[169] Chandra Interactive Analysis of Observations (CIAO) is available at http://cxc.harvard.edu/ciao/.

We use specextract to extract X-ray spectra and response files from a similar 1.″25 region, centered on Sgr A*. Since our primary interest for this data set is the flare emission, we do not extract background spectra from a separate spatial region. Instead, spectra of the quiescent off-flare intervals play the role of our background spectra.

The flare and off-flare intervals are identified by analyzing the X-ray light curves of each observation. For the easily detectable flare on 2017 April 11 (observation ID 20041), we use the direct Gaussian fitting method presented in Neilsen et al. (2013). For 2017 April 7 (observation ID 19727), we use the Bayesian Blocks decomposition (Scargle 1998; Scargle et al. 2013; Williams et al. 2017); this method is better suited to detecting the sustained low-level activity apparent toward the end of the observation.

4.2.3. Nuclear Spectroscopic Telescope Array

X-ray observations from the Nuclear Spectroscopic Telescope Array (NuSTAR; Harrison et al. 2013) performed three Sgr A* observations from 2017 April 6 to 11 (observation IDs: 30302006002, 30302006004, 30302006006). These provide a total exposure time of ∼103.9 ks and were coordinated with the EHT campaign. We reduced the data using the NuSTAR Data Analysis Software NuSTARDAS-v.1.6.0[170] and HEASOFT-v.6.19, filtered for periods of high instrumental background due to South Atlantic Anomaly (SAA) passages and known bad detector pixels. Photon arrival times were corrected for onboard clock drift and processed to the solar system barycenter using the JPL-DE200 ephemeris. We used a source extraction region with 50″ radius centered on the radio position of Sgr A* and extracted 3–79 keV light curves in 100 s bins with dead time, point-spread function, and vignetting effects corrected (see Zhang et al. 2017, for further details on NuSTAR Sgr A* data reduction). For all three observations we made use of the data obtained by both focal plane modules FPMA and FPMB.

For flare spectral analysis, we used nuproducts in HEASOFT-v.6.19 to create spectra and responses from 30″ circular regions (as recommended for faint sources to minimize the background) centered on the coordinates of Sgr A*. As explained in Section 4.2.4, NuSTAR only partially detected a flare from Sgr A* on 2017 April 11 (observation ID 30302006004); hence, we focus on this observation alone in the present work. The source spectrum was extracted from the NuSTAR good time intervals (GTIs) that overlap with the Chandra flare duration. The background spectrum was extracted from off-flare time intervals in the same observation.

4.2.4. X-Ray Flare Spectral Analysis

To obtain the best constraint on the spectrum of Sgr A* during its faint and moderate X-ray flares, we performed joint Chandra/NuSTAR spectral analysis of the two flares described in Section 4.2.2. The following analysis was performed in ISIS v1.6.2-43 and made use of Remeis isisscripts.[171] Chandra flare spectra were binned to a minimum of four channels and an S/N of 3 above 0.5 keV, while off-flare spectra were combined and binned to a minimum of two channels and an S/N of 3; we fit bins contained within the interval 1–9 keV. The NuSTAR FPMA/FPMB spectra of the 2017 April 11 flare were binned to a combined minimum S/N of 2 and a minimum of three channels above 3 keV. We ignored all bins not fully contained within the interval 3–79 keV. The resulting spectra are shown in Figure 7.

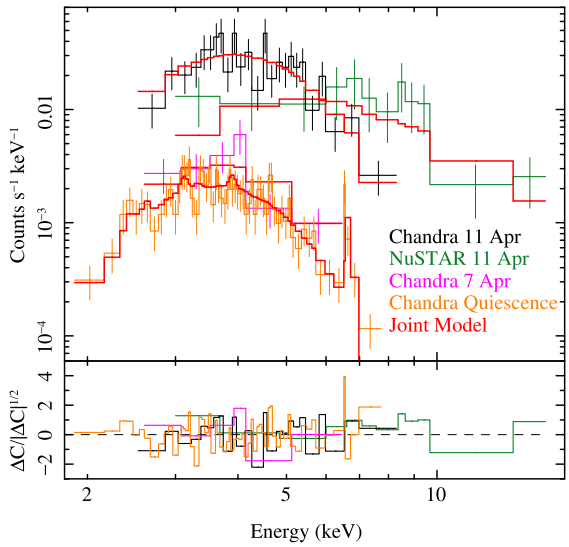

Figure 7. Joint Chandra–NuSTAR spectra of flares from Sgr A*. The magenta and black spectra are the Chandra flare spectra from 2017 April 7 and 11, respectively; the 2017 April 11 NuSTAR FPMA and FPMB flare spectra are combined for plotting purposes and shown in green. The orange data are the combined spectrum from the off-flare quiescent intervals of all four Chandra observations. The model described in Section 4.2.4 is shown in red for each data set.

Given the relatively small numbers of counts, we opted for simple absorbed power-law models for the flare spectra and compared our model to our data with Cash statistics (Cash 1979). We used the TBvarabs model with Wilms abundances and Verner cross sections (Verner et al. 1996; Wilms et al. 2000) and assumed a shared spectral index for both flares. (There is no conclusive evidence for a relationship between X-ray flare luminosity and X-ray spectral index; Neilsen et al. 2013; Zhang et al. 2017; Haggard et al. 2019.) Because a portion of the 2017 April 11 flare fell within a gap in the NuSTAR light curve, we included a cross-normalization constant between our NuSTAR and Chandra spectra (as well as between the FPMA and FPMB spectra).

For NuSTAR, we simply defined the spectrum of the off-flare interval as the background file for the 2017 April 11 flare spectrum, but we had to treat the Chandra spectra differently because they are susceptible to pileup during flares (e.g., Nowak et al. 2012), though fainter flares like those described here are not likely to be impacted. In particular, because pileup depends on the total count rate, not the background count rate, it is necessary to model the background spectrum and treat the flare emission as the sum of the background model and the absorbed power law. We fit the quiescent (off-flare) emission with a single vapec model; see Nowak et al. (2012) for more details.

Once we had a satisfactory fit to the joint flare spectra, we used the emcee Markov Chain Monte Carlo (MCMC) routine to find credible intervals for our fit parameters. For our MCMC runs, we used 10 walkers (i.e., 10 members of the ensemble) for each of our 10 free parameters and allowed them to evolve for 10,000 steps (a total of 1 million samples). These runs appear to converge within the first several tens of steps, so we

[170] https://heasarc.gsfc.nasa.gov/docs/nustar/analysis

[171] This research has made use of a collection of ISIS functions (ISISscripts) provided by ECAP/Remeis observatory and MIT (http://www.sternwarte.uni-erlangen.de/isis).

Table 5
Chandra/NuSTAR Joint Spectral Parameters

Parameter	Value	Units
$N_{\rm H}$	$17.8^{+3.5}_{-2.5}$	10^{22} cm^{-2}
Γ	$2.1^{+0.5}_{-0.4}$	...
$N_{\rm FPMB}$	$1.2^{+0.9}_{-0.4}$	...
$K_{\rm vapec}$	$0.0012^{+0.0009}_{-0.0005}$	...
$kT_{\rm vapec}$	$2^{+0.4}_{-0.5}$	keV
$N_{\rm ACIS}$	$1^{+0.7}_{-0.3}$	...
$F_{0704,2-10}$	$0.3^{+0.2}_{-0.2}$	10^{-12} erg s^{-1} cm^{-2}
$F_{0704,3-79}$	$0.5^{+0.8}_{-0.4}$	10^{-12} erg s^{-1} cm^{-2}
$F_{1104,2-10}$	$7.8^{+2.6}_{-3.9}$	10^{-12} erg s^{-1} cm^{-2}
$F_{1104,3-79}$	$15.4^{+8.9}_{-7.5}$	10^{-12} erg s^{-1} cm^{-2}
$F_{Q,2-10}$	$0.5^{+0.2}_{-0.1}$	10^{-12} erg s^{-1} cm^{-2}
$F_{Q,3-79}$	$0.31^{+0.05}_{-0.03}$	10^{-12} erg s^{-1} cm^{-2}

Note. $N_{\rm H}$ is the X-ray absorbing column density. Γ is the flare photon index. $N_{\rm FPMB}$ is the cross-normalization of the NuSTAR FPMB relative to the FPMA. $K_{\rm vapec}$ and $kT_{\rm vapec}$ are the normalization and temperature of the quiescent `vapec` component. $N_{\rm ACIS}$ is the cross-normalization of the Chandra ACIS spectrum relative to NuSTAR. Flare (F_{0704}, F_{1104}) and quiescent fluxes (F_Q) are quoted for the intervals 2–10 keV and 3–79 keV—the X-ray quiescent and flare fluxes presented in Table 2 are νF_ν in units of erg s^{-1} cm^{-2}, and so they differ slightly from the integrated values quoted here. See Sections 4.2.4 and 5.2.2 for further details.

discard the first 500 steps. We estimate an autocorrelation time for our parameter chains between ∼200 and 400 steps, indicating that we have 2500–5000 independent samples of each parameter.

Finally, we calculate the minimum width 90% credible interval for each parameter. We compute the cumulative distribution function for the samples for each parameter and select the smallest interval that contains 90% of the samples. The results are given in Table 5. Sgr A* flares are highly absorbed, with a column density of $N_{\rm H} = 17.8^{+3.5}_{-2.5}$ cm^{-2}; this is a bit higher than the values found by Nowak et al. (2012) and Wang et al. (2013), but the differences are within 1σ in both cases. The photon index of the flare is $\Gamma = 2.1^{+0.5}_{-0.4}$, which is not well constrained but is consistent with other analyses of X-ray flares (Porquet et al. 2008; Nowak et al. 2012; Neilsen et al. 2013; Haggard et al. 2019). The 2017 April 7 flare is only detected at 99% confidence but has an unabsorbed 2–10 keV flux of $F_{0704,2-10} = (0.3 \pm 0.2) \times 10^{-12}$ erg s^{-1} cm^{-2} and a 3–79 keV flux $F_{0704,3-79} = (0.5^{+0.8}_{-0.4}) \times 10^{-12}$ erg s^{-1} cm^{-2}. The 2017 April 11 flare has an unabsorbed 2–10 keV flux of $F_{1104,2-10} = (7.8^{+2.6}_{-3.9}) \times 10^{-12}$ erg s^{-1} cm^{-2}, which rises to $F_{1104,3-79} = (15.4^{+8.9}_{-7.5}) \times 10^{-12}$ erg s^{-1} cm^{-2} over the interval 3–79 keV.

As reported in Neilsen et al. (2015), the quiescent X-ray flux ($F_{Q,2-10}$) results from an admixture of two components. At the faint end of Sgr A*'s flux distribution, there are both variable and steady components, with the variable component likely arising from unresolved faint flares that contribute ∼10% of the apparent quiescent flux (see also Neilsen et al. 2013). Adopting the 2–10 keV flux from this joint fit (Table 5) and allowing a generous ∼1/3 contribution from unresolved X-ray flares, we estimate an upper limit on the median luminosity of $\sim 10^{33}$ erg s^{-1}. Larger flare contributions would be inconsistent with estimates that approximately 90% of the quiescent emission from Sgr A* is in fact associated with spatially resolved emission.

5. Final Data Products and Features

5.1. Event Horizon Telescope Data

In this section, we describe the properties of the 2017 Sgr A* EHT VLBI data. In particular, we detail the (u, v)-coverage, correlated flux densities, systematic error budgets, estimations for residual antenna-based gain errors, the influence of interstellar scattering on the measured visibilities, conservative estimates for the size of Sgr A* at 1.3 mm, and an assessment of the source variability.

5.1.1. Data Content

The observing schedules and (u, v)-coverages of our April 6 and 7 Sgr A* observing days are shown in Figures 1 and 8, respectively. Correlated flux densities as a function of baseline length are shown in Figure 9. The measurements show a good agreement between the products of our processing pipelines. The amplitude data presented in Figure 9 are broadly consistent with the Fourier signature of a blurred ring, indicating the presence of two minima at ∼3 and ∼6.5 Gλ. The ring model is a simple description of the data, used primarily to guide the eye in Figure 9. More complex best-fitting geometric models and image reconstructions are presented in Papers III and IV.

The calibrated Stokes $\mathcal{I}$ VLBI data of Sgr A* are made publicly available through the EHT data portal[172] under the `2022-D02-01` code (DOI: https://doi.org/10.25739/m140-ct59). The past validation history leading up to this data release is described in M87* Paper III. The calibration procedures applied to the Sgr A* data are described in Section 3. These procedures are agnostic to the source structure and encompass the signal stabilization with the automated EHT-HOPS and rPICARD data reduction pipelines, the flux density calibration based on a priori telescope metadata, the network gain calibration of colocated stations using measured 1.3 mm light curves of Sgr A*, and the bootstrapped telescope gain calibration from the analysis of the NRAO 530 and J1924 −2914 calibrator sources. The Stokes $\mathcal{I}$ data provided are time-averaged within 10 s intervals and frequency-averaged over 1875 MHz for the 227.1 GHz low band and 229.1 GHz high band. All common radio interferometric software packages can be used to further average the data in time, depending on the needs of the data analysis method used. As described in Section 3.3, a coherent average within 120 s intervals is recommended to minimize systematics. The accompanying telescope metadata used for the flux density calibration are provided in the standard ANTAB format,[173] and the visibilities are provided in the standard UVFITS format,[174] as well as simple text files, where the visibilities are given as comma-separated values (Table 6).

5.1.2. Interstellar Scattering

Interstellar scattering is a long-known extrinsic effect on the observed radio structure of Sgr A* (Davies et al. 1976). The scattering of radio waves from Sgr A* is predominantly caused by foreground stochastic turbulent electrons along the line of

[172] https://eventhorizontelescope.org/for-astronomers/data
[173] The generic definition of the flexible ANTAB text file format is given in http://www.aips.nrao.edu/cgi-bin/ZXHLP2.PL?ANTAB. The specific format convention adopted by the EHT is described in Janssen et al. (2019a).
[174] The UVFITS file format is described in ftp://ftp.aoc.nrao.edu/pub/software/aips/TEXT/PUBL/AIPSMEM117.PS.

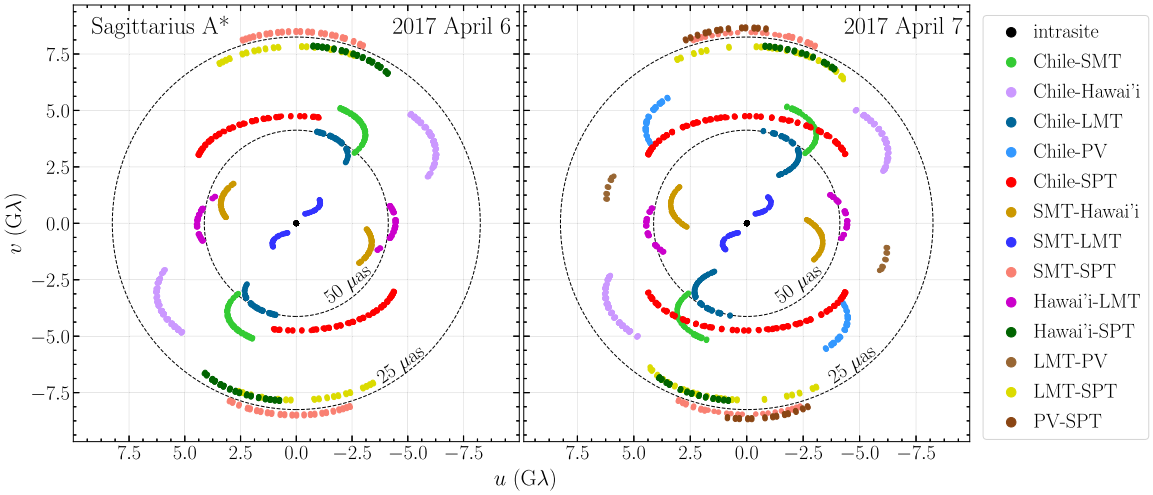

Figure 8. (u, v)-coverages from fringe detections of Sgr A* on 2017 April 6 and 7 plotted from scan-averaged data. Colocated stations are identified by location for clarity (Chile for ALMA and APEX, Hawai'i for JCMT and SMA). Fringe spacings of 25 and 50 μas are indicated with dashed circles.

the sight located far from the Galactic center (Bower et al. 2014; Dexter et al. 2017). At long observing wavelengths, the most dominant effect on the source structure is angular broadening, a chromatic effect arising from diffractive scattering (see, e.g., Narayan 1992), resulting in a Gaussian image with a size proportional to the squared wavelength for wavelengths $\lambda \gtrsim 1$ cm (Davies et al. 1976; van Langevelde et al. 1992; Bower et al. 2004; Shen et al. 2005; Bower et al. 2006; Johnson et al. 2018; Lu et al. 2018). Furthermore, the scattering is anisotropic, with stronger angular broadening along the east–west direction compared to the north–south direction (Frail et al. 1994; Jauncey et al. 1989). The angular broadening has an FWHM of $(1.380 \pm 0.013)\lambda_{\rm cm}^2$ mas along the major axis and $(0.703 \pm 0.013)\lambda_{\rm cm}^2$ mas along the minor axis, with the major axis at a position angle $81^\circ.9 \pm 0^\circ.2$ east of north (Johnson et al. 2018). The intrinsic source angular size is also chromatic, with a $\theta_{\rm src} \propto \lambda$ dependence (Johnson et al. 2018). Consequently, observations at 1.3 mm, where historical measurements of Sgr A* determined the size to be ~50–60 μas (Doeleman et al. 2008; Fish et al. 2011; Johnson et al. 2018; Lu et al. 2018), are in the regime where the intrinsic source structure is no longer subdominant to scattering and becomes the dominant structure in the image. Angular broadening can be described by a convolution of an unscattered image with a scattering kernel, or equivalently by a multiplication of the unscattered, intrinsic interferometric visibilities by the appropriate Fourier-conjugate kernel (Goodman & Narayan 1989). More background information and reviews on interstellar scattering can be found in Rickett (1990), Narayan (1992), and Thompson et al. (2017).

Secondary effects arise from density irregularities in the interstellar medium, causing stochastic variations in the scattering, as well as diffraction effects. These variations introduce substructure in the image that is not intrinsic to the source (Goodman & Narayan 1989; Johnson & Gwinn 2015; Johnson & Narayan 2016; Psaltis et al. 2018). Scattering-induced substructure was first discovered in images of Sgr A* at 1.3 cm by Gwinn et al. (2014) and later observed at other wavelengths (Johnson et al. 2018; Issaoun et al. 2019b, 2021; Cho et al. 2022), giving additional constraints on the scattering properties of Sgr A*. This substructure is caused by modes in the scattering material on scales comparable to the image extent, so scattering models with identical scatter broadening may still exhibit strong differences in their scattering substructure. The substructure manifests in the visibility domain as "refractive noise," which is an additive complex noise component with broad correlation structure across baselines and time (Johnson & Narayan 2016). Using observations of Sgr A* from 1.3 mm to 30 cm, Johnson et al. (2018) have shown that the combined image broadening and substructure strongly constrain the power spectrum of density fluctuations, which is consistent with later observations that occurred close to the 2017 EHT observations of Sgr A* described in this work (Sections 4.1.1 and 4.1.2) and in Issaoun et al. (2019b, 2021) and Cho et al. (2022).

Calibrated EHT data sets indicate that the intrinsic structure is dominant in measured visibilities and that both diffractive and refractive scattering effects are limited, as anticipated from the empirically obtained scattering model and early EHT observations. In Figure 10, we show the scattering kernel in both the image and visibility domains based on the scattering parameters in Johnson et al. (2018), together with the calibrated EHT data. The analysis from Johnson et al. (2018) implies a non-Gaussian kernel (solid lines) more compact than the conventional Gaussian kernel adopted in early literature. Consequently, the angular broadening effect, i.e., multiplication of the intrinsic visibilities with the Fourier-conjugate kernel of scattering, causes a slight decrease in visibility amplitudes (and therefore the S/N) by a factor of a few at maximum. The observed Sgr A* visibility amplitudes exhibit a steeper decrease with baseline length than the scattering kernel, suggesting that the intrinsic source structure, larger than the scattering kernel, is clearly resolved despite angular broadening.

The refractive substructure is likely also not dominant in Sgr A* at 1.3 mm. In Figure 10(b), we show typical refractive substructures along with the major and minor axes of the anisotropic scattering kernel expected for a reference model, adopted in Paper III, computed with `eht-imaging` based on the Psaltis et al. (2018) and Johnson et al. (2018) scattering model (see Paper III, Section 4.1 for details). While the rms noise levels due to the refractive substructure are dependent on the source size and shape (see, e.g., Johnson & Narayan 2016), the variations due to the deviation of the intrinsic source

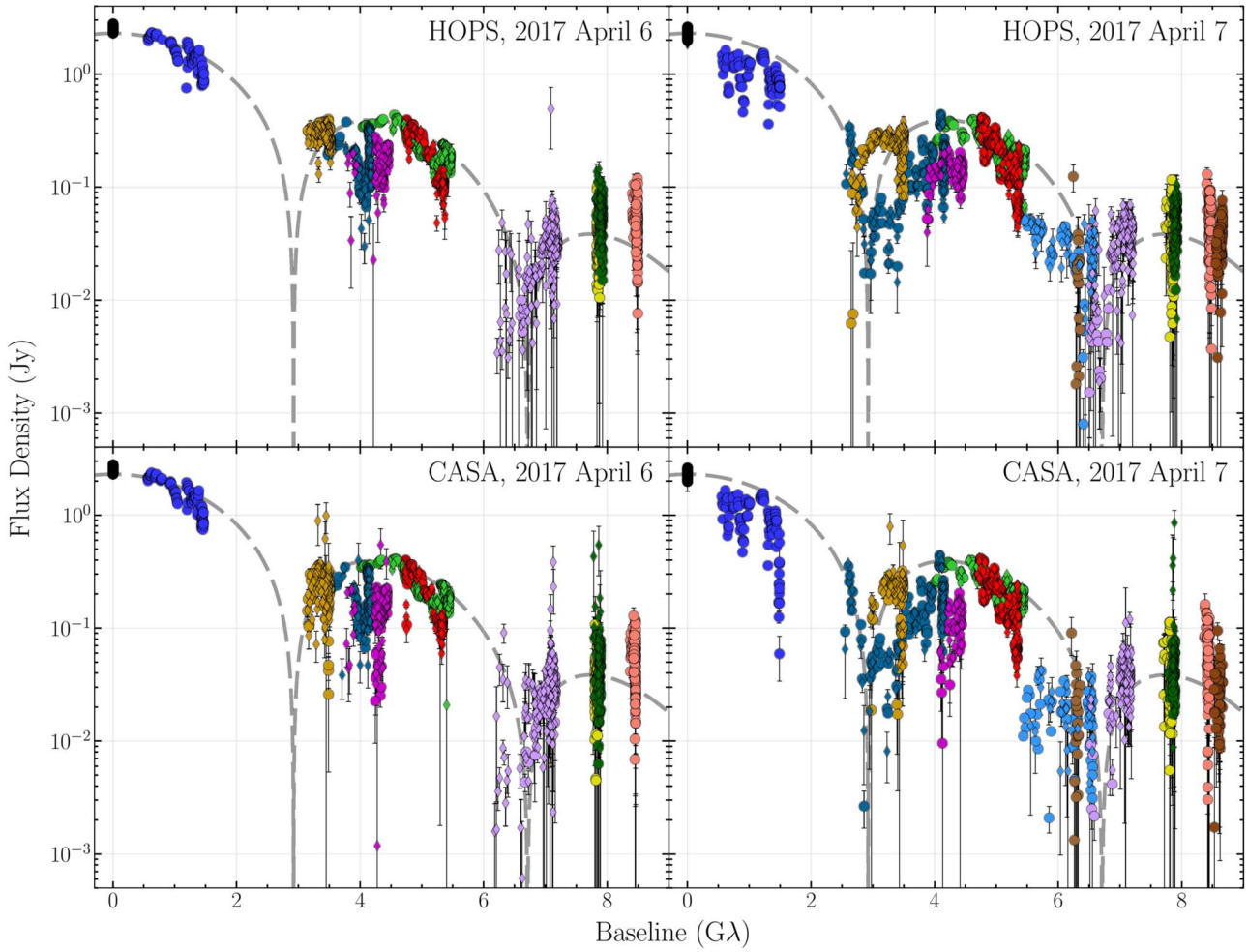

Figure 9. Measured correlated flux densities of Sgr A* on April 6 and 7 of the HOPS (top) and CASA (bottom) data overplotted with a thin (unresolved) ring model with a ∼50 μas diameter, which has been blurred with a 23 μas FWHM circular Gaussian source (Papers III and IV). Flux densities have been calibrated based on estimated station SEFDs, measured light curves (Section 3.2.1), and calibrator gain transfers (Section 3.2.2). The data are averaged in 120 s bins, which causes phase coherence losses in a few scans. Error bars denote ±1σ uncertainty from thermal noise. Detections are color-coded by baselines, as in Figure 8. Redundant baselines are shown with different symbols: circles for baselines to ALMA and SMA; diamonds for baselines to APEX and JCMT.

Table 6
Description of the Public Sgr A* EHT Data Release Content Provided in csv Format for the Low and High Bands on 2017 April 6 and 7

Column	Unit	Description
`Time`	UTC	Provided as fraction of a day
`T1`	(string)	Antenna #1 of the baseline
`T2`	(string)	Antenna #2 of the baseline
`U`	λ	(*u*) baseline vector component
`V`	λ	(*v*) baseline vector component
`Iamp`	Jy	Stokes $\mathcal{I}$ amplitude measurement
`Iphase`	degrees	Stokes $\mathcal{I}$ phase measurement
`Isigma`	Jy	Stokes $\mathcal{I}$ thermal noise

structure from the reference model are expected to be within a factor of a few (Paper III). Consequently, the effects of the refractive structure remain only a few percent of the total flux density at the maximum regardless of the source structure, hardly affecting the measured visibilities except for data points around the second null and/or at baselines longer than ∼6 Gλ, which are in the low-S/N regime. A more detailed analysis of the scattering properties on the observed visibilities and source structure is provided in Paper III. For the purposes of the current paper, we conclude that an estimate of the size of Sgr A* drawn from visibility data will be dominated by the intrinsic structure of the source rather than scattering.

5.1.3. Source Size and Fractional Compact Flux Density

The 1.3 mm source structure of Sgr A* has been reported to have FWHMs of several tens of microarcseconds from early EHT observations in the past decade (Doeleman et al. 2008; Fish et al. 2011; Johnson et al. 2015; Lu et al. 2018), consistent with our 2017 observations (Figure 8). The SMT–LMT baseline is the shortest intersite VLBI baseline provided in EHT observations, covering ∼0.6–1.5 Gλ corresponding to a fringe spacing of ∼140–370 μas. For a fringe spacing much larger than the source size, the visibility amplitude is well approximated by a quadratic function solely governed by the size along the baseline direction and the compact total flux density of the source (Issaoun et al. 2019a). Along with the direction of the SMT–LMT baseline, the EHT array has the

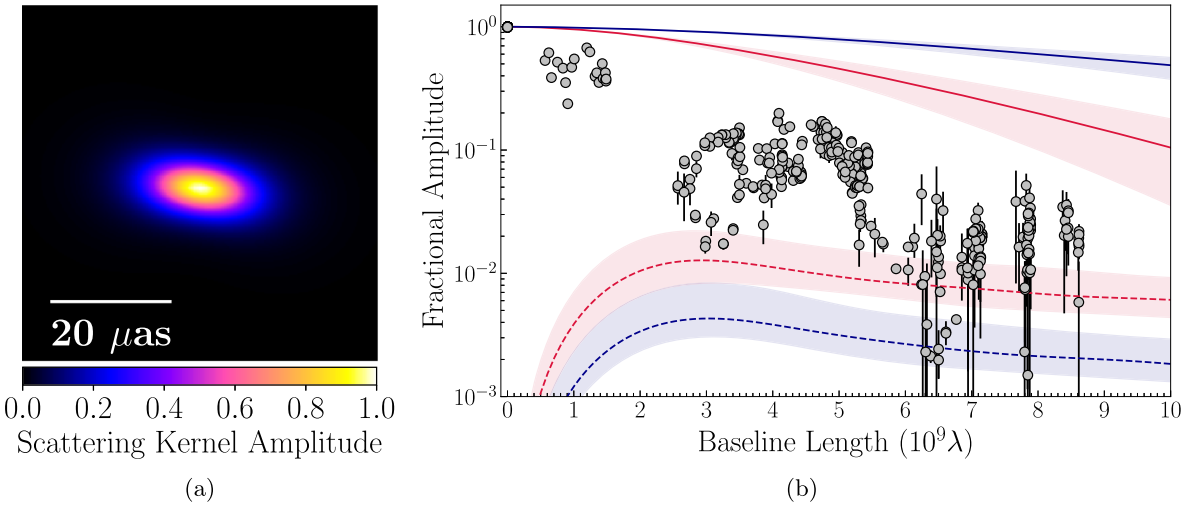

Figure 10. Diffractive scattering kernel and refractive noise rms at 1.3 mm based on the scattering model of Psaltis et al. (2018) and Johnson et al. (2018). (a) The image-domain representation of the kernel, with a second moment of 23.6 × 12.1 μas in FWHM at PA = 82°. (b) The normalized kernel amplitude and refractive noise level at 1.3 mm as a function of the baseline length (lines), overlaid on normalized Sgr A* low-band data from 2017 April 7 (circles). The red and blue solid lines show the amplitudes of the kernel along the major and minor axes, respectively. The dashed lines show the rms refractive noise levels for a reference model in Paper III along each axis colored in the same way. The shaded area around each line covers the range of possible amplitude values given the uncertainties of scattering parameters in the model. The Sgr A* amplitudes exhibit a steeper fall-off than that of the scatter-broadening kernel, indicative of resolved dominant intrinsic structure larger than the scattering kernel size. Furthermore, most of the amplitudes are well above the expected range of the refractive noise, implying that the refractive substructure is likely not dominant in the observed structure. The most affected baselines are Chile to Hawai'i and Spain, Mexico to Spain and the South Pole, and Hawai'i to the South Pole in the 6 – 8 Gλ range.

ALMA–LMT baseline with intermediate baseline lengths of 2.6–4.2 Gλ (see Figure 8). The visibility amplitudes on these baselines are useful to constrain the compact total flux density and source size on VLBI scales along the directions of these baselines, together with the intrasite short baselines tracing the total flux density on arcsecond scales (see M87* Paper IV, Appendix B.1).

Here, we derive constraints on the total compact flux density and the source size in a similar manner to M87* Paper IV by making use of these baselines. Compared with M87* data presented in M87* Paper III, Sgr A* data are further calibrated using interpolated gain solutions from calibrators (Section 3.2.2). We therefore modify the equations in M87* Paper IV and derive the three constraints outlined below.

Constraint 1. The first constraint is based on the fact that the visibility amplitudes fall approximately quadratically with baseline length on short baselines, (Issaoun et al. 2019a). The intermediate to long baselines tend to measure larger correlated flux density than what is expected for a Gaussian source with equivalent quadratic amplitude behavior on short baselines. While localized visibility-domain features such as "nulls" may give lower flux densities than the equivalent Gaussian, the presence of image substructure will tend to increase the average flux density. On short baselines, we can thus express the visibility amplitudes in terms of an equivalent circular Gaussian visibility function,

$$V_{\rm G}(\boldsymbol{u};\, I_0,\, \theta) = I_0 e^{-\frac{(\pi\theta|\boldsymbol{u}|)^2}{4\ln 2}}, \tag{5}$$

where I_0 is the total flux density of the Gaussian source, $|\boldsymbol{u}|$ is the length of the baseline, and θ is its FWHM in radians. We can deduce that the measured amplitude ratio of the ALMA–LMT over SMT–LMT baselines will be larger than the corresponding ratio from a circular Gaussian source model. Consequently, the FWHM size of a circular Gaussian determined by the amplitude ratio between SMT–LMT and ALMA–LMT baselines provides an estimate of the minimum compact source size $\theta_{\rm cpt}$ that is not significantly affected by the intrinsic fine-scale source structure:

$$\theta_{\rm cpt} \gtrsim \sqrt{\frac{4\ln 2 \ln\left(\frac{|\,\mathcal{V}_{\rm SMT-LMT}\,|}{|\,\mathcal{V}_{\rm ALMA-LMT}\,|}\right)}{\pi^2(|\boldsymbol{u}|^2_{\rm ALMA-LMT} - |\boldsymbol{u}|^2_{\rm SMT-LMT})}}. \tag{6}$$

Here $\mathcal{V}_{i-j}$ denotes the true visibility on the baseline $i-j$. The ratio of the true visibility amplitudes is lower-bounded by

$$\frac{|\mathcal{V}_{\rm SMT-LMT}|}{|\mathcal{V}_{\rm ALMA-LMT}|} \geqslant (1 - \sqrt{\Delta g^2_{\rm ALMA} + \Delta g^2_{\rm SMT}})\frac{|V_{\rm SMT-LMT}|}{|V_{\rm ALMA-LMT}|}, \tag{7}$$

where V_{i-j} and Δg_i denote the calibrated measured visibility and the deviation of its residual station gain from unity, respectively, after gain calibration using calibrators. $\Delta g_{\rm ALMA}$ and $\Delta g_{\rm SMT}$ are estimated to be 0.05 and 0.06, respectively, corresponding to the standard deviation of gain solutions from calibrator data across multiple imaging methods described in Section 3.2.2. We take the median of the visibility amplitude ratio from the collection of constraints derived for each single VLBI scan to derive a robust estimate of the minimum source size. With this method, we are able to derive a conservative constraint, which is agnostic to the assumed source structure (e.g., the presence of a null from a ring-like structure).

Constraint 2. The second constraint comes from the curvature of visibility amplitudes between the intrasite baselines and the LMT–SMT baseline. Since the compact flux density should not exceed the total flux density measured with the intrasite baselines, the amplitude fall from the intrasite to LMT–SMT baselines gives the maximum limit of that from the compact flux density to LMT–SMT baseline. Therefore, it gives the maximum limit of the source FWHM size with an

equivalent circular Gaussian as

$$\theta_{\rm cpt} \leqslant \frac{2\sqrt{\ln 2}}{\pi |\boldsymbol{u}|} \sqrt{\ln \frac{F_{\rm tot}}{|\mathcal{V}_{\rm LMT-SMT}|}}. \quad (8)$$

With the residual gain uncertainty, this maximum limit is upper-bounded by

$$\frac{1}{|\mathcal{V}_{\rm LMT-SMT}|} \leqslant \frac{1 + \sqrt{\Delta g_{\rm LMT}^2 + \Delta g_{\rm SMT}^2 + \Delta g_{\rm tot}^2}}{|V_{\rm LMT-SMT}|}. \quad (9)$$

In the same manner as with other stations, $\Delta g_{\rm LMT}$ is estimated to be 0.12 after calibrator gain transfer. $\Delta g_{\rm tot}$, the fractional uncertainty in the light curve, is estimated to be at most 0.2 based on the consistency of light curves obtained with different instruments / reduction pipelines (see Wielgus et al. 2022). Similarly to Constraint 1, the median of the ratio is adopted to mitigate the effects of statistical errors.

Constraint 3. The minimum compact flux density can be derived by the maximum amplitudes of the LMT–SMT baseline, since the visibility amplitudes are maximum at zero baseline length, as given by

$$\begin{aligned} F_{\rm cpt} &\geqslant |\mathcal{V}_{\rm SMT-LMT}| \\ &\geqslant (1 - \sqrt{\Delta g_{\rm LMT}^2 + \Delta g_{\rm SMT}^2})|V_{\rm LMT-SMT}|. \end{aligned} \quad (10)$$

In the above equation, the equality is satisfied in the extreme situation when the source is completely unresolved at the LMT–SMT baseline, whereas in reality it partially resolves the source structure. A stronger constraint is given by the equivalent circular Gaussian with the minimum source size (Constraint 1) extrapolated from the LMT–SMT baselines, described by

$$F_{\rm cpt} \geqslant |\mathcal{V}_{\rm LMT-SMT}| e^{\frac{(\pi |\boldsymbol{u}| \theta_{\rm cpt})^2}{4 \ln 2}}. \quad (11)$$

We note that the upper and lower limits on the source size obtained from Constraints 1 and 2 are along the directions of LMT–SMT and LMT–ALMA baselines. Using synthetic data from general relativistic magnetohydrodynamics (GRMHD) and semianalytic geometric models in Paper III, we have verified that these size constraints remain valid for various morphologies sharing similar profiles of visibility amplitudes with EHT Sgr A* data (see Paper III for details). The variability of the GRMHD models is often in excess of our observational measurements (Paper V). Therefore, our size constraints are also validated against a changing source structure over the course of our observations.

The derived constraints are summarized in Table 7 and Figure 11(a) for each observing day and for both days combined. As shown in Figure 11(b), the equivalent Gaussians with the minimum and maximum sizes reasonably give the upper and lower bounds of the visibility amplitudes, respectively, on short baselines. Either of the source size constraints indicates that the 2017 EHT Sgr A* data resolve compact emission of several tens of microarcseconds, consistent with the early EHT observations (Doeleman et al. 2008; Fish et al. 2011; Johnson et al. 2015, 2018; Lu et al. 2018).

The estimated minimum fractional compact flux density is ~70%–90%, indicating that the vast majority of the radio emission from Sgr A* arises from the horizon-scale emission resolved with the EHT. The maximum limit on the extended emission resolved out on the shortest VLBI baselines is indeed much less than for M87*, 3C 279, and Centaurus A—all of which are known to have a prominent extended jet (M87* Paper IV; Kim et al. 2020; Janssen et al. 2021)—as expected by the nondetection of an extended jet in longer-wavelength VLBI observations across many decades (see Section 5.1.2 and references therein) and early EHT observations.

5.1.4. Source Variability

Studies of the variability of Sgr A* light curves at 230 GHz in 2005–2017 (e.g., Marrone et al. 2008; Dexter et al. 2014; Bower et al. 2018) indicate that on long timescales (from a few days to years) the source fluctuates between 2.0 and 4.5 Jy. During the 2017 EHT observations, Sgr A* was in a low-luminosity state with a mean flux density of $\sim 2.4 \pm 0.2$ Jy between 213 and 229 GHz (Table 2). The 2 days for which VLBI data analysis is presented in this series of papers exhibit a low degree of variability that is typical for this source, characterized by the modulation index (standard deviation divided by mean) $\sigma/\mu < 10\%$. The power spectral density has a red-noise character on timescales from 1 minute to several hours, with a transition to white noise for longer timescales. On 2017 April 11 the millimeter flux rises by over 50%, following the X-ray flare maximum with a delay of ~2 hr. The data on this day appear significantly more variable. An analysis of the 2017 April 11 VLBI data will be presented in a separate future publication. A detailed analysis of the full data set of Sgr A* light curves contemporaneous with the EHT 2017 observations is presented in the companion paper Wielgus et al. (2022).

The $\mathcal{Q}$-metric (Roelofs et al. 2017) quantifies the variability of a compact source resolved on VLBI baselines in a series of closure phases as a function of time on a specific baseline triangle. The metric compares the observed closure phase variations ($\hat{\sigma}^2$) to those expected from thermal noise ($\tilde{\epsilon}^2$), after detrending the data to account for slow variations due to the evolution of baselines as Earth rotates (see Roelofs et al. 2017, for details):

$$\mathcal{Q} = \frac{\hat{\sigma}^2 - \tilde{\epsilon}^2}{\hat{\sigma}^2}. \quad (12)$$

A static source is expected to give a $\mathcal{Q}$-metric value close to 0, and a variable source can give a $\mathcal{Q}$-metric value up to 1.

Figure 12 shows the $\mathcal{Q}$-metric for M87* and Sgr A* data. First, we have averaged the visibilities within bins of 120 s to accumulate S/N. These averaged data are used to compute closure phases. Then, we have divided the closure phases into 2 hr segments and performed the detrending with a third-order polynomial within each segment. Our analysis is therefore sensitive to structural source variability occurring on timescales between 120 s and 2 hr. The $\mathcal{Q}$-metric is generally higher for Sgr A* than for M87*, which does not necessarily indicate that Sgr A* varies more strongly because of the different error budgets for the two sources. However, the different $\mathcal{Q}$-metric values do indicate that intrinsic variability is detected with higher significance for Sgr A* than for M87*. The high sensitivity to thermal noise can lead to different $\mathcal{Q}$-values on redundant triangles.

Because of imperfections in the detrending procedure (a third-order polynomial does not generally capture any static source structure) and the particular realization of the thermal noise, a static source may also give nonzero $\mathcal{Q}$-metric values. In order to determine on which triangles we detect significant variability, the measured $\mathcal{Q}$-metric values are therefore

Table 7
Constraints on Fractional Compact Flux Density and Source Size Measured along the Directions of the LMT–SMT and LMT–ALMA Baselines

UTC Day (2017 April)	Fractional Compact Flux Density	Fractional Compact Flux Density (with the Minimum Source Size)	Minimum Source Size (μas)	Maximum Source Size (μas)
6	0.83	0.88	42	79
7	0.66	0.73	38	95
6+7	0.83	0.88	39	87

compared to those simulated for a range of static source models for Sgr A*. Shown in Figure 12 are 1σ upper limits of the distributions of $\mathcal{Q}$-metric values obtained from synthetic data generated from different single static GRMHD-GRRT snapshots (Paper V), with different realizations of either a static or moving scattering screen. We have applied random position angle rotations to 12 random frames drawn from MAD/SANE models with spins of ± 0.94, ± 0.5, 0; $R_{\rm high} = 10$, 40; and inclination angles of 10°, 30°, 50°, 70° (a description of these models and their parameters is given in Paper V). For these 960 different source structures, we have generated synthetic data using 100 different thermal noise realizations for each observing day and the low- and high-frequency bands. We applied the same procedure to 11 frames of each of the source models used to calibrate the imaging methods in Paper III, which were chosen to match the measured visibility amplitudes of Sgr A*. The resulting $\mathcal{Q}$-metric values were bootstrapped to obtain the same number of values as those from the GRMHD models.

Scattering-screen variability generally has a small effect on the $\mathcal{Q}$-metric. Comparing the measured and simulated $\mathcal{Q}$-metric values, we see a significant excess for Sgr A* on ALMA–LMT–SMA, ALMA–SMT–SMA, and ALMA–SMT–LMT. For these triangles, the observed closure phase variability cannot be explained by variability due to interstellar scattering or imperfections in the detrending procedure. The excess variability in degrees $\breve{\mathcal{Q}} = \sqrt{\hat{\sigma}^2 - \tilde{\epsilon}^2}$ is 16.4°, 6.8°, and 3.1° for these triangles, respectively. Hence, although the $\mathcal{Q}$-metric does indicate intraday closure phase variability in the Sgr A* data, it only does so on a few triangles, and the variability amplitude is small.

More detailed discussions of the source variability based on static and time-dependent reconstructions of the underlying Sgr A* source model, as well as examples of typical closure phase trends, are given in Papers III and IV. Effects of phase decoherence, low S/N near interferometric nulls, residual time-dependent gain errors, stochastic interstellar scattering effects, and changing baseline vectors due to Earth rotation introduce additional scatter in the correlated flux densities shown in Figures 9, 10, and 11. Paper IV presents a model that takes these effects into account and provides a clear detection of intrinsic flux density variability on horizon scales.

5.2. Multiwavelength Data

5.2.1. Millimeter, NIR, and X-Ray Data Products

The supplementary ground- and space-based data products leveraged here are published in original works and/or are available in public archives.

EAVN observations of Sgr A* at 22 and 43 GHz are available in Cho et al. (2022), GMVA 86 GHz observations are published in Issaoun et al. (2019b), and a detailed discussion of the VLT/GRAVITY NIR flux distribution can be found in Gravity Collaboration et al. (2020).

Chandra, Swift, and NuSTAR data products are available via NASA archives[175,176,177] and are collected in the EHT data portal[178] under the `2022-D02-03` code (DOI:https://doi.org/10.25739/26fq-k306). The repository contains the following data products:

1. Description of observations and data processing (format: text).
2. Fluxes from Swift-XRT observations (format: CSV).
3. Fluxes from Chandra observations (format: CSV).
4. Fluxes from NuSTAR observations (format: CSV).
5. Scripts, spectral, and response files for modeling Chandra and NuSTAR data (format: standard X-ray data formats).
6. Sampled posterior distributions of X-ray spectral model based on Chandra and NuSTAR data (format: FITS).

The EHT data portal also contains the broadband spectrum presented in Table 2 (see also Section 5.2.2 below) with frequency, flux density, its uncertainty, and instrument index (format: CSV).

5.2.2. Time-averaged Spectral Energy Distribution

Figure 13 displays the SED for Sgr A* during the 2017 EHT campaign (open black circles) overplotted on the historically observed broadband spectrum (colored points). The SED illustrates Sgr A*'s wide range of variable and nonvariable states. Larger shaded swaths mark regions of the SED where the source is particularly variable; their bounds mark characteristic quiescent emission and high flux states, which can last for timescales of minutes to hours. (A time-binned historic SED representative of states without extreme variability is presented in Paper VI.) We do not plot a typical quiescent value for NuSTAR frequencies (3–79 keV) since upper limits are complicated by contributions from non-Sgr A* sources in the Galactic center. The flux and luminosity values from each observatory coordinating during the EHT campaign are listed in Table 2. The quiescent and flare X-ray luminosities in the SED are νL_ν in units of erg s^{-1}; their equivalent νF_ν values in erg s^{-1} cm^{-2} (Table 2) differ slightly from the integrated flux values in Table 5.

During the EHT run, Sgr A*'s SED is consistent with historical observations of the black hole in the radio, millimeter, NIR, and X-ray, as outlined in the Introduction and Section 5.2.3. For example, the moderately bright X-ray flare detected with Chandra and NuSTAR on 2017 April 11 falls within the range of previously observed X-ray flares (see

[175] The Chandra Data Archive: https://cxc.harvard.edu/cda/.
[176] The Swift Data Archive: https://swift.gsfc.nasa.gov/archive/.
[177] The NuSTAR Data Archive: https://heasarc.gsfc.nasa.gov/docs/nustar/nustar_archive.html.
[178] https://eventhorizontelescope.org/for-astronomers/data

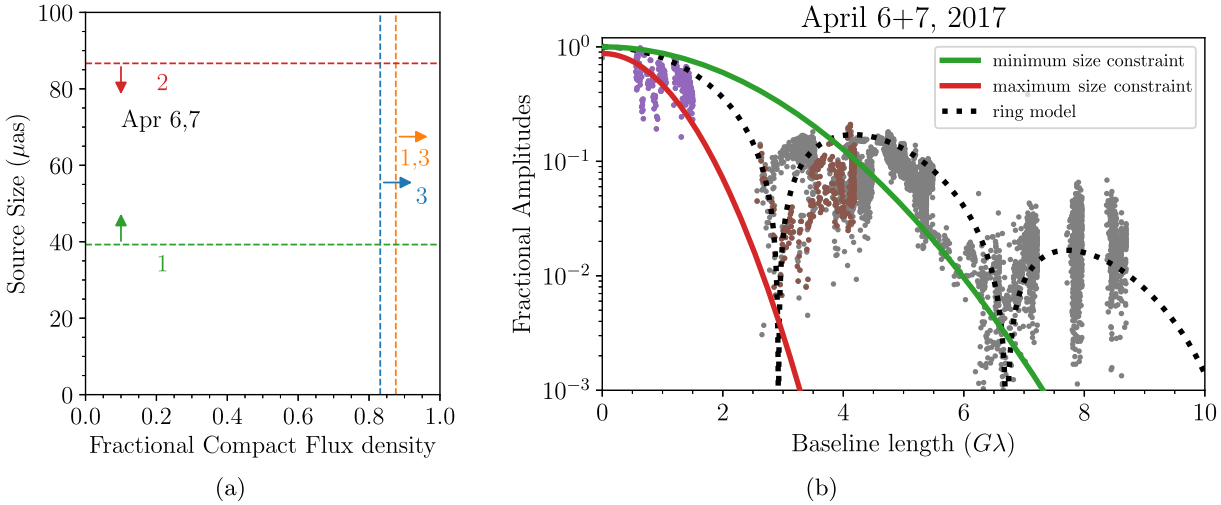

Figure 11. Joint constraints on the size and total compact flux density of the 1.3 mm emission in Sgr A* shown in Table 7. See Section 5.1.3 for details. (a) Numbered constraints correspond to (1) the LMT–SMT/LMT–ALMA amplitude ratio, (2) LMT–SMT amplitudes coupled with the requirement $F_{\rm cpt} \leqslant F_{\rm tot}$, and (3) the maximum LMT–SMT amplitude. The position angles of the LMT–SMT and LMT–ALMA baselines range from 125° to 164°. (b) Fractional visibility amplitudes of circular Gaussian sources with FWHMs corresponding to the minimum (green line) and maximum (red line) size constraints for the April 6 and 7 data sets. Flux-normalized calibrated amplitudes are overlaid, where those of the LMT–SMT and ALMA–LMT baselines used to derive these size constraints are colored in purple and brown, respectively. The dotted line denotes the ring model shown in Figure 9 for comparison.

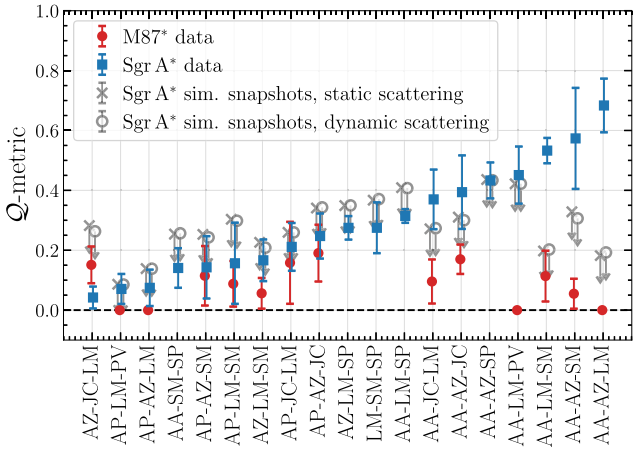

Figure 12. $\mathcal{Q}$-metric values (12) indicating intrinsic closure phase variability on baseline triangles with mutual visibility of both M87* and Sgr A* in ascending order of the Sgr A* variability. The two-letter station codes are taken from Table 3. Only closure phase tracks with more than 10 data points after averaging down to 120 s were used. The closure phase tracks were detrended within 2 hr segments by subtracting a third-degree polynomial before computing the $\mathcal{Q}$-metric. The plotted values are averages across days (2017 April 5, 6, 10, and 11 for M87*, 2017 April 6 and 7 for Sgr A*) and bands, with the error bars indicating the 1σ spread across the days and bands. The $\mathcal{Q}$-metrics for the M87* and Sgr A* data are shown in red and blue, respectively. The gray points show 1σ upper limits of the distributions of $\mathcal{Q}$-metric values obtained from synthetic data generated from intrinsically static source models, with either a static or moving scattering screen with parameters from Johnson et al. (2018), but with an enlarged power-law index of $\alpha = 1.5$ for the interstellar turbulence to obtain more conservative upper limits of scattering-induced variability. The static source models are a mix of models from the GRMHD library, which contains a large range of source structures, and the models used to calibrate the imaging methods in Paper III. Upper limits are computed based on the maximum $\mathcal{Q}$-metric values from independent realizations of possible source models and thermal noise on each triangle.

Section 4.2 and Figure 13). Since Sgr A* is not in an exceptional state during the 2017 EHT campaign, these observational constraints on the broadband SED offer valuable priors on theoretical models aiming to constrain GR, for example, the Kerr metric investigation presented in Paper VI.

Paper V in this series also uses these (quasi-)simultaneous EHT 1.3 mm and MWL constraints (on both luminosity and degree of variability) to aid in model selection and to provide a physical interpretation for these data, for example, by testing aligned, tilted, and stellar wind-fed scenarios using time-dependent GRMHD models. They compare specifically to three MWL bands, 86 GHz, 2.2 μas, and X-ray, which are relatively independent and thus probe different physics, and find that no one existing model can meet all of the EHT and MWL constraints. These challenges motivate improvements to the GRMHD model suites and encourage additional, joint EHT and MWL campaigns to fully characterize Sgr A*'s short- and long-term variability.

5.2.3. Characteristic Multiwavelength Variability

Sgr A*'s MWL variability has been studied in detail for more than two decades. Substantial obscuration in the plane of the Galaxy blocks our view of its optical and UV emission, but observations at other wavelengths show flickering, flares, and other stochastic processes on long and short timescales (e.g., Baganoff et al. 2001; Dodds-Eden et al. 2009; Nowak et al. 2012; Witzel et al. 2012; Bower et al. 2015; Neilsen et al. 2015; Do et al. 2019b; Haggard et al. 2019; Gravity Collaboration et al. 2020). Theoretical models also anticipate that observations at different wavelengths will probe different size scales and resolutions (e.g., Falcke & Markoff 2013). We briefly describe Sgr A*'s characteristic MWL variability, to put the X-ray flares (Section 4.2.4) and the broadband spectrum (Section 5.2.2) observed in 2017 into this broader context.

Sgr A*'s X-ray flux distribution can be decomposed into a steady quiescent component described by a Poisson process and a variable power-law component attributed to nonthermal flares that appear approximately once per day (Neilsen et al. 2015). Sgr A*'s quiescent NIR light curves show a red-noise process and a nonlinear, non-Gaussian flux density distribution, skewed to higher flux densities, which changes slope near a median flux density of 1.1 ± 0.3 mJy (flux densities below 0.1 mJy are rarely observed; e.g., Witzel et al. 2012;

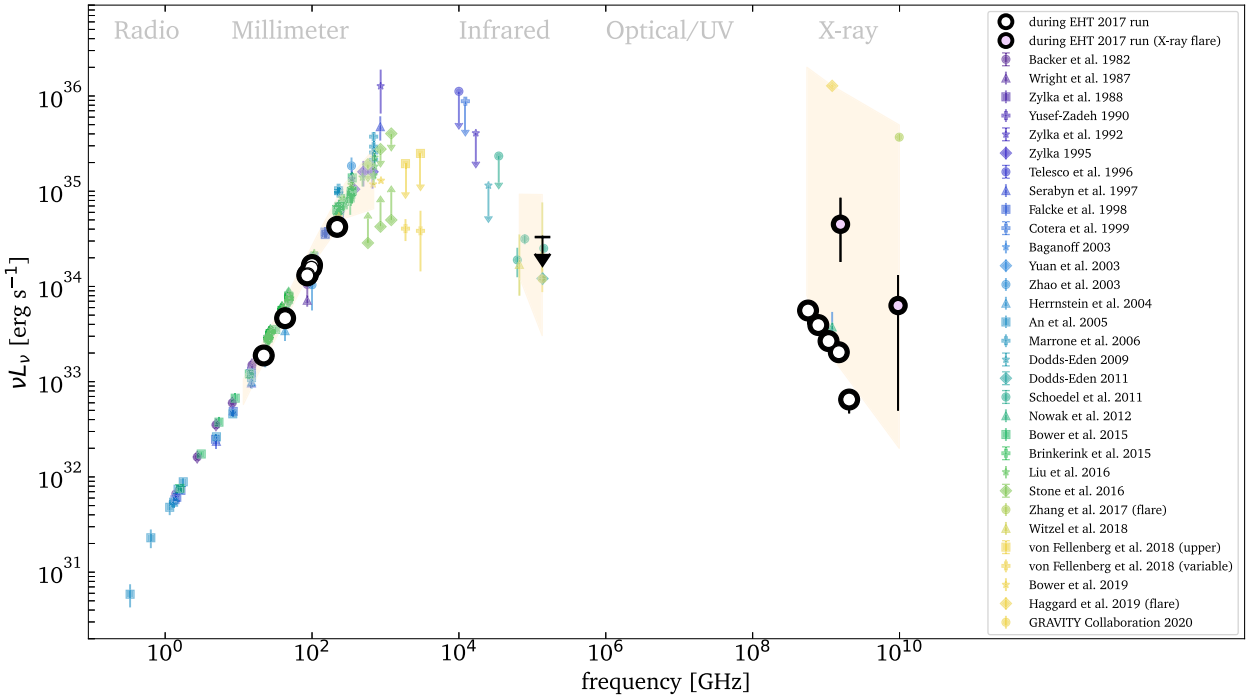

Figure 13. The time-averaged SED for the compact Sgr A* source during the 2017 EHT run is shown as black open circles and an NIR upper limit. Luminosities for the X-ray flare observed on 2017 April 11 are indicated as black circles filled with light purple. Table 2 lists the 2017 values in units of flux and luminosity. Colored background points display the historic SED of Sgr A* in flaring and quiescent states, with the light yellow polygons indicating the range of previously observed variability (Backer 1982; Wright et al. 1987; Zylka & Mezger 1988; Yusef-Zadeh et al. 1990; Zylka et al. 1992, 1995; Telesco et al. 1996; Serabyn et al. 1997; Falcke et al. 1998; Cotera et al. 1999; Baganoff et al. 2003; Yuan et al. 2003; Zhao et al. 2003; Herrnstein et al. 2004; An et al. 2005; Marrone et al. 2006b; Dodds-Eden et al. 2009, 2011; Schödel et al. 2011; Nowak et al. 2012; Bower et al. 2015; Brinkerink et al. 2015; Liu et al. 2016; Stone et al. 2016; Zhang et al. 2017; von Fellenberg et al. 2018; Witzel et al. 2018; Bower et al. 2019; Haggard et al. 2019; Gravity Collaboration et al. 2020). A time-binned historic SED representative of states without extreme variability is presented in Paper VI.

Do et al. 2019b; Gravity Collaboration et al. 2020). Thus, the NIR flux can also be attributed to separate quiescent and variable components.

The X-ray and NIR variability timescales are both typically several hours, consistent with Sgr A*'s ISCO period of approximately 4–30 minutes for prograde orbits (vs. 5 days to 1 month for M87*; for further discussion of this comparison, see Paper I). Recently, the orbital motion of a compact polarized hot spot just outside of the ISCO has been offered as an explanation for high-resolution, time-resolved interferometric NIR observations (Gravity Collaboration et al. 2018), reinforcing the notion that this may be a horizon-scale phenomena.

Correlations between the X-ray and NIR flux peaks (e.g., Dodds-Eden et al. 2009; Ponti et al. 2017; Boyce et al. 2019; GRAVITY Collaboration et al. 2021; Michail et al. 2021; Boyce 2022) and similarities in their statistical properties and flux density distributions (Witzel et al. 2012, 2018, 2021; Neilsen et al. 2015) point to a physical connection between the emission at these wavelengths, though the X-ray structure function seems to have less power at short timescales than the NIR structure function (Witzel et al. 2012, 2018; Neilsen et al. 2015; Witzel et al. 2021).

At submillimeter and radio wavelengths Sgr A* also shows a quiescent state superposed with almost continuous variability (e.g., Miyazaki et al. 2004; Macquart & Bower 2006; Yusef-Zadeh et al. 2011; Brinkerink et al. 2015). These longer-duration flares may be delayed by a few hours relative to the X-ray/NIR flares, but simultaneous observations are sparse and the correlations remain tenuous (Capellupo et al. 2017). Some submillimeter flares have also been associated with NIR flares, while others show no correlation (Marrone et al. 2008; Morris et al. 2012; Fazio et al. 2018; Michail et al. 2021; Boyce 2022). Iwata et al. (2020) pursued a detailed study of Sgr A*'s flux density distribution at 217.5, 219.5, and 234.0 GHz, finding variability on timescales of ∼tens of minutes to hours that is likely to arise near the ISCO. They find no lag between 217.5 and 234.0 GHz.

Analysis by Wielgus et al. (2022) based on the ALMA and SMA data associated with this 2017 EHT campaign shows Sgr A* mostly in a quiescent state at 213, 220, and 229 GHz (Figures 6 and 13), though the 2017 April 11 observations following the X-ray flare show enhanced millimeter-wavelength variability. The millimeter light curves are consistent with a red-noise process with the power spectral density slope between −2 and −3 on timescales between 1 minute and several hours. In an independent study, Bower et al. (2018) detect both linear and circular polarization in Sgr A*'s millimeter emission. They find a mean RM of about -5×10^5 rad m^{-2} and variability on timescales of hours to months. Long-term variability in the RM (of order weeks to months) is likely due to turbulence in the accretion flow, while short-term variability seems to arise from complex emission and propagation effects near the black hole. They also detect circular polarization with a mean value of $-1.1\% \pm 0.2\%$ that is variable on timescales of hours to months (Bower et al. 2018). EHT polarimetric measurements of Sgr A* will be the subject of future works in this series.

These and other MWL observations have led to broad consensus that near Sgr A*'s event horizon there are two components: (1) a relatively stable quiescent accretion flow, and (2) flares or bright flux excursions that vary on shorter

timescales. Accretion models for Sgr A* suggest that the system may drive a jet, and some data support this possibility. For example, an observed increase of variability amplitude with frequency and persistent time lags in the 18 – 43 GHz band may be indicative of a jet outflow (Brinkerink et al. 2021). Yet despite this and other tentative claims at γ-ray, X-ray, and radio wavelengths (e.g., Su & Finkbeiner 2012; Yusef-Zadeh et al. 2012; Li et al. 2013; Zhu et al. 2019; Rauch et al. 2016), a jet has not yet been conclusively confirmed. The accretion flow and the jet base are both candidates to drive Sgr A*'s variability (e.g., the base of the jet very likely dominates the emission near M87*), yet while their timescales may be distinct, the base of a jet and a variable RIAF remain difficult to tell apart (see Paper V).

Interstellar scattering may induce additional variable signals over timescales similar to (or longer than) those from the quiescent accretion flow. For example, one explanation for the detectability of the GC magnetar was a variable scattering screen (Eatough et al. 2013; Bower et al. 2014). Meanwhile, interactions with orbiting objects may cause additional variability, e.g., disruptions of ∼kilometer-sized rocky bodies, gaseous structures, or other interlopers (Čadež et al. 2008; Kostić et al. 2009; Gillessen et al. 2012; Zubovas et al. 2012; Ciurlo et al. 2020; Peißker et al. 2021). Contemporaneous observations with EHT and MWL facilities, particularly simultaneous capture of serendipitous events like flares, continue to offer the best opportunity for disentangling these contributions to Sgr A*'s variable emission.

6. Summary and Conclusions

Sgr A* and M87* are the primary targets of the EHT, for which the 2017 April observing campaign provided the required resolution and sensitivity to obtain horizon-scale images of these SMBHs. M87* total-intensity and polarization results from the 2017 data have been published earlier (M87* Papers I–VIII). In this new series of papers (Papers I–VI), we present the imaging, analysis, and interpretation of the 2017 Sgr A* EHT and accompanying data at X-ray, NIR, and millimeter wavelengths from EAVN, GMVA, VLT/NACO, Swift, Chandra, and NuSTAR. Sgr A* was observed by the EHT on 2017 April 5, 6, 7, 10, and 11. In this series of papers, we focus our analysis on the days with the best (u, v)-coverage, 2017 April 6 and 7; a detailed analysis of the full set of Sgr A* millimeter light curves can be found in the companion paper by Wielgus et al. (2022).

We use the two independent pipelines EHT-HOPS (Blackburn et al. 2019) and rPICARD (Janssen et al. 2018, 2019b) for the calibration of the EHT data. By utilizing the data from both pipelines, we obtain scientific results in a robust manner, independent of assumptions made for the data calibration. With various jackknife tests, we estimate the amount of systematic noise present in the EHT data and verify that data issues are mitigated.

We present updates to the a priori gain calibration for several EHT stations. Additionally, we perform a network calibration (Blackburn et al. 2019) based on the total flux of the source to correct the gains of the colocated EHT stations. To account for the rapid flux variability of Sgr A* in this process, we use light curves obtained at a short intrascan cadence from the ALMA and SMA connected element interferometers. Finally, we transfer gain solutions from self-calibration solutions of the co-observed J1924−2914 and NRAO 530 calibrator sources. With the time-dependent network calibration and calibrator gain transfer, it is possible to partially correct for time-variable station gain errors that are difficult to solve for using the Sgr A* data alone owing to intrinsic source variability.

The calibrated visibility amplitudes can be described by a blurred ring with a diameter of ∼50 μas (a deeper discussion of the source size and morphology can be found in Papers III and IV). The majority of the total flux measured in our VLBI experiment arises from horizon scales in Sgr A*. Using MWL constraints on the interstellar scattering screen toward Sgr A*, we show that the scattering-induced angular broadening of the source is subdominant to the intrinsic source structure uncovered by the EHT. The refractive noise added by the scattering screen is only relevant for data at baseline lengths $\gtrsim$6 Gλ.

Without making strong assumptions about the source structure, we find a compact source size of 39–87 μas for Sgr A*, which is in agreement with earlier 1.3 mm VLBI observations of the source. A more precise modeling-based estimation of the source size is given in Paper III. On 2017 April 6 and 7, the source was in a low-luminosity state, where the total flux fluctuates around 2.4 Jy with a modulation index of less than 10%. The Sgr A* closure phases show clear intrinsic structural variability on timescales of a few minutes to a few hours that is further investigated in Papers III and IV.

MWL observations show that Sgr A* was in a mostly quiescent state, with broadband flux levels consistent with historical measures. We detect two X-ray flares: one very faint flare on 2017 April 7, and a brighter flare on 2017 April 11. The fainter 2017 April 7 flare is detected at low significance by Swift and Chandra, and the brighter 2017 April 11 flare is detected more confidently by Chandra and NuSTAR. ALMA and SMA 2017 April 11 observations begin immediately after the bright X-ray flare and show enhanced millimeter-wavelength variability (Wielgus et al. 2022). These MWL data offer important constraints for theoretical models; indeed, no one of the GRMHD models presented in Paper V can match the full suite of MWL constraints. These unprecedented EHT and MWL data thus provide a rich opportunity to improve models of Sgr A* and to advance our understanding of the physics near the SMBH event horizon. The high-quality, nearly simultaneous MWL SED is additionally valuable for understanding the priors for sophisticated tests of GR (see Paper VI). Looking ahead, future detailed analysis of the EHT and MWL observations on 2017 April 11 holds great promise for understanding the underlying mechanisms that drive Sgr A*'s flares and other variability.

We thank an anonymous referee for their insight and helpful suggestions that have improved this paper.

The Event Horizon Telescope Collaboration thanks the following organizations and programs: the Academia Sinica; the Academy of Finland (projects 274477, 284495, 312496, 315721); the Agencia Nacional de Investigación y Desarrollo (ANID), Chile via NCN19_058 (TITANs) and Fondecyt 1221421, the Alexander von Humboldt Stiftung; an Alfred P. Sloan Research Fellowship; Allegro, the European ALMA Regional Centre node in the Netherlands, the NL astronomy research network NOVA and the astronomy institutes of the University of Amsterdam, Leiden University and Radboud University; the ALMA North America Development Fund; the Black Hole Initiative, which is funded by grants from the John

Templeton Foundation and the Gordon and Betty Moore Foundation (although the opinions expressed in this work are those of the author(s) and do not necessarily reflect the views of these Foundations); Chandra DD7-18089X and TM6-17006X; the China Scholarship Council; China Postdoctoral Science Foundation fellowship (2020M671266); Consejo Nacional de Ciencia y Tecnología (CONACYT, Mexico, projects U0004-246083, U0004-259839, F0003-272050, M0037-279006, F0003-281692, 104497, 275201, 263356); the Consejería de Economía, Conocimiento, Empresas y Universidad of the Junta de Andalucía (grant P18-FR-1769), the Consejo Superior de Investigaciones Científicas (grant 2019AEP112); the Delaney Family via the Delaney Family John A. Wheeler Chair at Perimeter Institute; Dirección General de Asuntos del Personal Académico-Universidad Nacional Autónoma de México (DGAPA-UNAM, projects IN112417 and IN112820); the Dutch Organization for Scientific Research (NWO) VICI award (grant 639.043.513) and grant OCENW.KLEIN.113; the Dutch National Supercomputers, Cartesius and Snellius (NWO Grant 2021.013); the EACOA Fellowship awarded by the East Asia Core Observatories Association, which consists of the Academia Sinica Institute of Astronomy and Astrophysics, the National Astronomical Observatory of Japan, Center for Astronomical Mega-Science, Chinese Academy of Sciences, and the Korea Astronomy and Space Science Institute; the European Research Council (ERC) Synergy Grant "BlackHoleCam: Imaging the Event Horizon of Black Holes" (grant 610058); the European Union Horizon 2020 research and innovation programme under grant agreements RadioNet (No 730562) and M2FINDERS (No 101018682); the Generalitat Valenciana postdoctoral grant APOSTD/2018/177 and GenT Program (project CIDEGENT/2018/021); MICINN Research Project PID2019-108995GB-C22; the European Research Council for advanced grant "JETSET: Launching, propagation and emission of relativistic jets from binary mergers and across mass scales" (Grant No. 884631); the Institute for Advanced Study; the Istituto Nazionale di Fisica Nucleare (INFN) sezione di Napoli, iniziative specifiche TEONGRAV; the International Max Planck Research School for Astronomy and Astrophysics at the Universities of Bonn and Cologne; DFG research grant "Jet physics on horizon scales and beyond" (Grant No. FR 4069/2-1); Joint Princeton/Flatiron and Joint Columbia/Flatiron Postdoctoral Fellowships, research at the Flatiron Institute is supported by the Simons Foundation; the Japan Ministry of Education, Culture, Sports, Science and Technology (MEXT; grant JPMXP1020200109); the Japanese Government (Monbukagakusho: MEXT) Scholarship; the Japan Society for the Promotion of Science (JSPS) Grant-in-Aid for JSPS Research Fellowship (JP17J08829); the Joint Institute for Computational Fundamental Science, Japan; the Key Research Program of Frontier Sciences, Chinese Academy of Sciences (CAS, grants QYZDJ-SSW-SLH057, QYZDJSSW-SYS008, ZDBS-LY-SLH011); the Leverhulme Trust Early Career Research Fellowship; the Max-Planck-Gesellschaft (MPG); the Max Planck Partner Group of the MPG and the CAS; the MEXT/JSPS KAKENHI (grants 18KK0090, JP21H01137, JP18H03721, JP18K13594, 18K03709, JP19K14761, 18H01245, 25120007); the Malaysian Fundamental Research Grant Scheme (FRGS) FRGS/1/2019/STG02/UM/02/6; the MIT International Science and Technology Initiatives (MISTI) Funds; the Ministry of Science and Technology (MOST) of Taiwan (103-2119-M-001-010-MY2, 105-2112-M-001-025-MY3, 105-2119-M-001-042, 106-2112-M-001-011, 106-2119-M-001-013, 106-2119-M-001-027, 106-2923-M-001-005, 107-2119-M-001-017, 107-2119-M-001-020, 107-2119-M-001-041, 107-2119-M-110-005, 107-2923-M-001-009, 108-2112-M-001-048, 108-2112-M-001-051, 108-2923-M-001-002, 109-2112-M-001-025, 109-2124-M-001-005, 109-2923-M-001-001, 110-2112-M-003-007-MY2, 110-2112-M-001-033, 110-2124-M-001-007, and 110-2923-M-001-001); the Ministry of Education (MoE) of Taiwan Yushan Young Scholar Program; the Physics Division, National Center for Theoretical Sciences of Taiwan; the National Aeronautics and Space Administration (NASA, Fermi Guest Investigator grant 80NSSC20K1567, NASA Astrophysics Theory Program grant 80NSSC20K0527, NASA NuSTAR award 80NSSC20K0645); NASA Hubble Fellowship grant HST-HF2-51431.001-A awarded by the Space Telescope Science Institute, which is operated by the Association of Universities for Research in Astronomy, Inc., for NASA, under contract NAS5-26555; the National Institute of Natural Sciences (NINS) of Japan; the National Key Research and Development Program of China (grant 2016YFA0400704, 2017YFA0402703, 2016YFA0400702); the National Science Foundation (NSF, grants AST-0096454, AST-0352953, AST-0521233, AST-0705062, AST-0905844, AST-0922984, AST-1126433, AST-1140030, DGE-1144085, AST-1207704, AST-1207730, AST-1207752, MRI-1228509, OPP-1248097, AST-1310896, AST-1440254, AST-1555365, AST-1614868, AST-1615796, AST-1715061, AST-1716327, AST-1716536, OISE-1743747, AST-1816420, AST-1935980, AST-2034306); NSF Astronomy and Astrophysics Postdoctoral Fellowship (AST-1903847); the Natural Science Foundation of China (grants 11650110427, 10625314, 11721303, 11725312, 11873028, 11933007, 11991052, 11991053, 12192220, 12192223); the Natural Sciences and Engineering Research Council of Canada (NSERC, including a Discovery Grant and the NSERC Alexander Graham Bell Canada Graduate Scholarships-Doctoral Program); the National Youth Thousand Talents Program of China; the National Research Foundation of Korea (the Global PhD Fellowship Grant: grants NRF-2015H1A2A1033752, the Korea Research Fellowship Program: NRF-2015H1D3A1066561, Brain Pool Program: 2019H1D3A1A01102564, Basic Research Support Grant 2019R1F1A1059721, 2021R1A6A3A01086420, 2022R1C 1C1005255); Netherlands Research School for Astronomy (NOVA) Virtual Institute of Accretion (VIA) postdoctoral fellowships; Onsala Space Observatory (OSO) national infrastructure, for the provisioning of its facilities/observational support (OSO receives funding through the Swedish Research Council under grant 2017-00648); the Perimeter Institute for Theoretical Physics (research at Perimeter Institute is supported by the Government of Canada through the Department of Innovation, Science and Economic Development and by the Province of Ontario through the Ministry of Research, Innovation and Science); the Spanish Ministerio de Ciencia e Innovación (grants PGC2018-098915-B-C21, AYA2016-80889-P, PID2019-108995GB-C21, PID2020-117404GB-C21); the University of Pretoria for financial aid in the provision of the new Cluster Server nodes and SuperMicro (USA) for a SEEDING GRANT approved towards these nodes in 2020; the Shanghai Pilot Program for Basic Research, Chinese Academy of Science, Shanghai Branch (JCYJ-SHFY-2021-013); the State Agency for Research of the Spanish

MCIU through the "Center of Excellence Severo Ochoa" award for the Instituto de Astrofísica de Andalucía (SEV-2017-0709); the Spinoza Prize SPI 78-409; the South African Research Chairs Initiative, through the South African Radio Astronomy Observatory (SARAO, grant ID 77948), which is a facility of the National Research Foundation (NRF), an agency of the Department of Science and Innovation (DSI) of South Africa; the Toray Science Foundation; Swedish Research Council (VR); the US Department of Energy (USDOE) through the Los Alamos National Laboratory (operated by Triad National Security, LLC, for the National Nuclear Security Administration of the USDOE (Contract 89233218CNA000001); and the YCAA Prize Postdoctoral Fellowship.

We thank the staff at the participating observatories, correlation centers, and institutions for their enthusiastic support. This paper makes use of the following ALMA data: ADS/JAO.ALMA#2016.1.01154.V. ALMA is a partnership of the European Southern Observatory (ESO; Europe, representing its member states), NSF, and National Institutes of Natural Sciences of Japan, together with National Research Council (Canada), Ministry of Science and Technology (MOST; Taiwan), Academia Sinica Institute of Astronomy and Astrophysics (ASIAA; Taiwan), and Korea Astronomy and Space Science Institute (KASI; Republic of Korea), in cooperation with the Republic of Chile. The Joint ALMA Observatory is operated by ESO, Associated Universities, Inc. (AUI)/NRAO, and the National Astronomical Observatory of Japan (NAOJ). The NRAO is a facility of the NSF operated under cooperative agreement by AUI. This research used resources of the Oak Ridge Leadership Computing Facility at the Oak Ridge National Laboratory, which is supported by the Office of Science of the U.S. Department of Energy under Contract No. DE-AC05-00OR22725. We also thank the Center for Computational Astrophysics, National Astronomical Observatory of Japan. The computing cluster of Shanghai VLBI correlator supported by the Special Fund for Astronomy from the Ministry of Finance in China is acknowledged.

APEX is a collaboration between the Max-Planck-Institut für Radioastronomie (Germany), ESO, and the Onsala Space Observatory (Sweden). The SMA is a joint project between the SAO and ASIAA and is funded by the Smithsonian Institution and the Academia Sinica. The JCMT is operated by the East Asian Observatory on behalf of the NAOJ, ASIAA, and KASI, as well as the Ministry of Finance of China, Chinese Academy of Sciences, and the National Key Research and Development Program (No. 2017YFA0402700) of China and Natural Science Foundation of China grant 11873028. Additional funding support for the JCMT is provided by the Science and Technologies Facility Council (UK) and participating universities in the UK and Canada. The LMT is a project operated by the Instituto Nacional de Astrófisica, Óptica, y Electrónica (Mexico) and the University of Massachusetts at Amherst (USA). The IRAM 30-m telescope on Pico Veleta, Spain is operated by IRAM and supported by CNRS (Centre National de la Recherche Scientifique, France), MPG (Max-Planck-Gesellschaft, Germany) and IGN (Instituto Geográfico Nacional, Spain). The SMT is operated by the Arizona Radio Observatory, a part of the Steward Observatory of the University of Arizona, with financial support of operations from the State of Arizona and financial support for instrumentation development from the NSF. Support for SPT participation in the EHT is provided by the National Science Foundation through award OPP-1852617 to the University of Chicago. Partial support is also provided by the Kavli Institute of Cosmological Physics at the University of Chicago. The SPT hydrogen maser was provided on loan from the GLT, courtesy of ASIAA.

This work used the Extreme Science and Engineering Discovery Environment (XSEDE), supported by NSF grant ACI-1548562, and CyVerse, supported by NSF grants DBI-0735191, DBI-1265383, and DBI-1743442. XSEDE Stampede2 resource at TACC was allocated through TG-AST170024 and TG-AST080026N. XSEDE JetStream resource at PTI and TACC was allocated through AST170028. This research is part of the Frontera computing project at the Texas Advanced Computing Center through the Frontera Large-Scale Community Partnerships allocation AST20023. Frontera is made possible by National Science Foundation award OAC-1818253. This research was carried out using resources provided by the Open Science Grid, which is supported by the National Science Foundation and the U.S. Department of Energy Office of Science. Additional work used ABACUS2.0, which is part of the eScience center at Southern Denmark University. Simulations were also performed on the SuperMUC cluster at the LRZ in Garching, on the LOEWE cluster in CSC in Frankfurt, on the HazelHen cluster at the HLRS in Stuttgart, and on the Pi2.0 and Siyuan Mark-I at Shanghai Jiao Tong University. The computer resources of the Finnish IT Center for Science (CSC) and the Finnish Computing Competence Infrastructure (FCCI) project are acknowledged. This research was enabled in part by support provided by Compute Ontario (http://computeontario.ca), Calcul Quebec (http://www.calculquebec.ca) and Compute Canada (http://www.computecanada.ca).

The EHTC has received generous donations of FPGA chips from Xilinx Inc., under the Xilinx University Program. The EHTC has benefited from technology shared under open-source license by the Collaboration for Astronomy Signal Processing and Electronics Research (CASPER). The EHT project is grateful to T4Science and Microsemi for their assistance with Hydrogen Masers. This research has made use of NASA's Astrophysics Data System. We gratefully acknowledge the support provided by the extended staff of the ALMA, both from the inception of the ALMA Phasing Project through the observational campaigns of 2017 and 2018. We would like to thank A. Deller and W. Brisken for EHT-specific support with the use of DiFX. We thank Martin Shepherd for the addition of extra features in the Difmap software that were used for the CLEAN imaging results presented in this paper. We acknowledge the significance that Maunakea, where the SMA and JCMT EHT stations are located, has for the indigenous Hawaiian people.

The scientific results reported here are also based in part on observations made by the East Asian VLBI Network (EAVN), the Global 3 mm VLBI Array (GMVA), the Very Large Telescope (VLT), the Neil Gehrels Swift Observatory, the Chandra X-ray Observatory, and the Nuclear Spectroscopic Telescope (NuSTAR). We thank the scheduling, data processing, and archive teams from these facilities for making these observations possible. IMV acknowledges the use of LLuis Vives HPC resources of the University of Valencia.

Facility: EHT, ALMA, APEX, IRAM:30 m, JCMT, LMT, SMA, ARO:SMT, SPT, Chandra, EAVN, GMVA, NuSTAR, Swift, VLT.

Software: DiFX (Deller et al. 2011), CALC, PolConvert (Martí-Vidal et al. 2016), HOPS (Whitney et al. 2004), EHT-HOPS Pipeline (Blackburn et al. 2019), CASA (McMullin et al. 2007), rPICARD (Janssen et al. 2018, 2019b).

ORCID iDs

Kazunori Akiyama https://orcid.org/0000-0002-9475-4254
Antxon Alberdi https://orcid.org/0000-0002-9371-1033
Juan Carlos Algaba https://orcid.org/0000-0001-6993-1696
Richard Anantua https://orcid.org/0000-0003-3457-7660
Keiichi Asada https://orcid.org/0000-0001-6988-8763
Rebecca Azulay https://orcid.org/0000-0002-2200-5393
Uwe Bach https://orcid.org/0000-0002-7722-8412
Anne-Kathrin Baczko https://orcid.org/0000-0003-3090-3975
Mislav Baloković https://orcid.org/0000-0003-0476-6647
John Barrett https://orcid.org/0000-0002-9290-0764
Michi Bauböck https://orcid.org/0000-0002-5518-2812
Bradford A. Benson https://orcid.org/0000-0002-5108-6823
Lindy Blackburn https://orcid.org/0000-0002-9030-642X
Raymond Blundell https://orcid.org/0000-0002-5929-5857
Katherine L. Bouman https://orcid.org/0000-0003-0077-4367
Geoffrey C. Bower https://orcid.org/0000-0003-4056-9982
Hope Boyce https://orcid.org/0000-0002-6530-5783
Christiaan D. Brinkerink https://orcid.org/0000-0002-2322-0749
Roger Brissenden https://orcid.org/0000-0002-2556-0894
Silke Britzen https://orcid.org/0000-0001-9240-6734
Avery E. Broderick https://orcid.org/0000-0002-3351-760X
Dominique Broguiere https://orcid.org/0000-0001-9151-6683
Thomas Bronzwaer https://orcid.org/0000-0003-1151-3971
Sandra Bustamante https://orcid.org/0000-0001-6169-1894
Do-Young Byun https://orcid.org/0000-0003-1157-4109
John E. Carlstrom https://orcid.org/0000-0002-2044-7665
Chiara Ceccobello https://orcid.org/0000-0002-4767-9925
Andrew Chael https://orcid.org/0000-0003-2966-6220
Chi-kwan Chan https://orcid.org/0000-0001-6337-6126
Koushik Chatterjee https://orcid.org/0000-0002-2825-3590
Shami Chatterjee https://orcid.org/0000-0002-2878-1502
Ming-Tang Chen https://orcid.org/0000-0001-6573-3318
Yongjun Chen (陈永军) https://orcid.org/0000-0001-5650-6770
Xiaopeng Cheng https://orcid.org/0000-0003-4407-9868
Ilje Cho https://orcid.org/0000-0001-6083-7521
Pierre Christian https://orcid.org/0000-0001-6820-9941
Nicholas S. Conroy https://orcid.org/0000-0003-2886-2377
John E. Conway https://orcid.org/0000-0003-2448-9181
James M. Cordes https://orcid.org/0000-0002-4049-1882
Thomas M. Crawford https://orcid.org/0000-0001-9000-5013
Geoffrey B. Crew https://orcid.org/0000-0002-2079-3189
Alejandro Cruz-Osorio https://orcid.org/0000-0002-3945-6342
Yuzhu Cui (崔玉竹) https://orcid.org/0000-0001-6311-4345
Jordy Davelaar https://orcid.org/0000-0002-2685-2434
Mariafelicia De Laurentis https://orcid.org/0000-0002-9945-682X
Roger Deane https://orcid.org/0000-0003-1027-5043
Jessica Dempsey https://orcid.org/0000-0003-1269-9667
Gregory Desvignes https://orcid.org/0000-0003-3922-4055
Jason Dexter https://orcid.org/0000-0003-3903-0373
Vedant Dhruv https://orcid.org/0000-0001-6765-877X
Sheperd S. Doeleman https://orcid.org/0000-0002-9031-0904
Sean Dougal https://orcid.org/0000-0002-3769-1314
Sergio A. Dzib https://orcid.org/0000-0001-6010-6200
Ralph P. Eatough https://orcid.org/0000-0001-6196-4135
Razieh Emami https://orcid.org/0000-0002-2791-5011
Heino Falcke https://orcid.org/0000-0002-2526-6724
Joseph Farah https://orcid.org/0000-0003-4914-5625
Vincent L. Fish https://orcid.org/0000-0002-7128-9345
Ed Fomalont https://orcid.org/0000-0002-9036-2747
H. Alyson Ford https://orcid.org/0000-0002-9797-0972
Raquel Fraga-Encinas https://orcid.org/0000-0002-5222-1361
Per Friberg https://orcid.org/0000-0002-8010-8454
Christian M. Fromm https://orcid.org/0000-0002-1827-1656
Antonio Fuentes https://orcid.org/0000-0002-8773-4933
Peter Galison https://orcid.org/0000-0002-6429-3872
Charles F. Gammie https://orcid.org/0000-0001-7451-8935
Roberto García https://orcid.org/0000-0002-6584-7443
Olivier Gentaz https://orcid.org/0000-0002-0115-4605
Boris Georgiev https://orcid.org/0000-0002-3586-6424
Ciriaco Goddi https://orcid.org/0000-0002-2542-7743
Roman Gold https://orcid.org/0000-0003-2492-1966
Arturo I. Gómez-Ruiz https://orcid.org/0000-0001-9395-1670
José L. Gómez https://orcid.org/0000-0003-4190-7613
Minfeng Gu (顾敏峰) https://orcid.org/0000-0002-4455-6946
Mark Gurwell https://orcid.org/0000-0003-0685-3621
Kazuhiro Hada https://orcid.org/0000-0001-6906-772X
Daryl Haggard https://orcid.org/0000-0001-6803-2138
Michael H. Hecht https://orcid.org/0000-0002-4114-4583
Ronald Hesper https://orcid.org/0000-0003-1918-6098
Dirk Heumann https://orcid.org/0000-0002-7671-0047
Luis C. Ho (何子山) https://orcid.org/0000-0001-6947-5846
Paul Ho https://orcid.org/0000-0002-3412-4306
Mareki Honma https://orcid.org/0000-0003-4058-9000
Chih-Wei L. Huang https://orcid.org/0000-0001-5641-3953
Lei Huang (黄磊) https://orcid.org/0000-0002-1923-227X
Shiro Ikeda https://orcid.org/0000-0002-2462-1448
C. M. Violette Impellizzeri https://orcid.org/0000-0002-3443-2472
Makoto Inoue https://orcid.org/0000-0001-5037-3989
Sara Issaoun https://orcid.org/0000-0002-5297-921X
David J. James https://orcid.org/0000-0001-5160-4486
Buell T. Jannuzi https://orcid.org/0000-0002-1578-6582
Michael Janssen https://orcid.org/0000-0001-8685-6544
Britton Jeter https://orcid.org/0000-0003-2847-1712
Wu Jiang (江悟) https://orcid.org/0000-0001-7369-3539
Alejandra Jiménez-Rosales https://orcid.org/0000-0002-2662-3754
Michael D. Johnson https://orcid.org/0000-0002-4120-3029
Svetlana Jorstad https://orcid.org/0000-0001-6158-1708
Abhishek V. Joshi https://orcid.org/0000-0002-2514-5965
Taehyun Jung https://orcid.org/0000-0001-7003-8643

Mansour Karami https://orcid.org/0000-0001-7387-9333
Ramesh Karuppusamy https://orcid.org/0000-0002-5307-2919
Tomohisa Kawashima https://orcid.org/0000-0001-8527-0496
Garrett K. Keating https://orcid.org/0000-0002-3490-146X
Mark Kettenis https://orcid.org/0000-0002-6156-5617
Dong-Jin Kim https://orcid.org/0000-0002-7038-2118
Jae-Young Kim https://orcid.org/0000-0001-8229-7183
Jongsoo Kim https://orcid.org/0000-0002-1229-0426
Junhan Kim https://orcid.org/0000-0002-4274-9373
Motoki Kino https://orcid.org/0000-0002-2709-7338
Jun Yi Koay https://orcid.org/0000-0002-7029-6658
Prashant Kocherlakota https://orcid.org/0000-0001-7386-7439
Patrick M. Koch https://orcid.org/0000-0003-2777-5861
Shoko Koyama https://orcid.org/0000-0002-3723-3372
Carsten Kramer https://orcid.org/0000-0002-4908-4925
Michael Kramer https://orcid.org/0000-0002-4175-2271
Thomas P. Krichbaum https://orcid.org/0000-0002-4892-9586
Cheng-Yu Kuo https://orcid.org/0000-0001-6211-5581
Noemi La Bella https://orcid.org/0000-0002-8116-9427
Tod R. Lauer https://orcid.org/0000-0003-3234-7247
Daeyoung Lee https://orcid.org/0000-0002-3350-5588
Sang-Sung Lee https://orcid.org/0000-0002-6269-594X
Po Kin Leung https://orcid.org/0000-0002-8802-8256
Aviad Levis https://orcid.org/0000-0001-7307-632X
Zhiyuan Li (李志远) https://orcid.org/0000-0003-0355-6437
Rocco Lico https://orcid.org/0000-0001-7361-2460
Greg Lindahl https://orcid.org/0000-0002-6100-4772
Michael Lindqvist https://orcid.org/0000-0002-3669-0715
Mikhail Lisakov https://orcid.org/0000-0001-6088-3819
Jun Liu (刘俊) https://orcid.org/0000-0002-7615-7499
Kuo Liu https://orcid.org/0000-0002-2953-7376
Elisabetta Liuzzo https://orcid.org/0000-0003-0995-5201
Wen-Ping Lo https://orcid.org/0000-0003-1869-2503
Andrei P. Lobanov https://orcid.org/0000-0003-1622-1484
Laurent Loinard https://orcid.org/0000-0002-5635-3345
Colin J. Lonsdale https://orcid.org/0000-0003-4062-4654
Ru-Sen Lu (路如森) https://orcid.org/0000-0002-7692-7967
Jirong Mao (毛基荣) https://orcid.org/0000-0002-7077-7195
Nicola Marchili https://orcid.org/0000-0002-5523-7588
Sera Markoff https://orcid.org/0000-0001-9564-0876
Daniel P. Marrone https://orcid.org/0000-0002-2367-1080
Alan P. Marscher https://orcid.org/0000-0001-7396-3332
Iván Martí-Vidal https://orcid.org/0000-0003-3708-9611
Satoki Matsushita https://orcid.org/0000-0002-2127-7880
Lynn D. Matthews https://orcid.org/0000-0002-3728-8082
Lia Medeiros https://orcid.org/0000-0003-2342-6728
Karl M. Menten https://orcid.org/0000-0001-6459-0669
Daniel Michalik https://orcid.org/0000-0002-7618-6556
Izumi Mizuno https://orcid.org/0000-0002-7210-6264
Yosuke Mizuno https://orcid.org/0000-0002-8131-6730
James M. Moran https://orcid.org/0000-0002-3882-4414
Kotaro Moriyama https://orcid.org/0000-0003-1364-3761
Monika Moscibrodzka https://orcid.org/0000-0002-4661-6332
Cornelia Müller https://orcid.org/0000-0002-2739-2994
Alejandro Mus https://orcid.org/0000-0003-0329-6874
Gibwa Musoke https://orcid.org/0000-0003-1984-189X
Ioannis Myserlis https://orcid.org/0000-0003-3025-9497
Andrew Nadolski https://orcid.org/0000-0001-9479-9957
Hiroshi Nagai https://orcid.org/0000-0003-0292-3645
Neil M. Nagar https://orcid.org/0000-0001-6920-662X
Masanori Nakamura https://orcid.org/0000-0001-6081-2420
Ramesh Narayan https://orcid.org/0000-0002-1919-2730
Gopal Narayanan https://orcid.org/0000-0002-4723-6569
Iniyan Natarajan https://orcid.org/0000-0001-8242-4373
Joey Neilsen https://orcid.org/0000-0002-8247-786X
Roberto Neri https://orcid.org/0000-0002-7176-4046
Chunchong Ni https://orcid.org/0000-0003-1361-5699
Aristeidis Noutsos https://orcid.org/0000-0002-4151-3860
Michael A. Nowak https://orcid.org/0000-0001-6923-1315
Junghwan Oh https://orcid.org/0000-0002-4991-9638
Hiroki Okino https://orcid.org/0000-0003-3779-2016
Héctor Olivares https://orcid.org/0000-0001-6833-7580
Gisela N. Ortiz-León https://orcid.org/0000-0002-2863-676X
Tomoaki Oyama https://orcid.org/0000-0003-4046-2923
Feryal Özel https://orcid.org/0000-0003-4413-1523
Daniel C. M. Palumbo https://orcid.org/0000-0002-7179-3816
Georgios Filippos Paraschos https://orcid.org/0000-0001-6757-3098
Jongho Park https://orcid.org/0000-0001-6558-9053
Harriet Parsons https://orcid.org/0000-0002-6327-3423
Nimesh Patel https://orcid.org/0000-0002-6021-9421
Ue-Li Pen https://orcid.org/0000-0003-2155-9578
Dominic W. Pesce https://orcid.org/0000-0002-5278-9221
Richard Plambeck https://orcid.org/0000-0001-6765-9609
Oliver Porth https://orcid.org/0000-0002-4584-2557
Felix M. Pötzl https://orcid.org/0000-0002-6579-8311
Ben Prather https://orcid.org/0000-0002-0393-7734
Jorge A. Preciado-López https://orcid.org/0000-0002-4146-0113
Dimitrios Psaltis https://orcid.org/0000-0003-1035-3240
Hung-Yi Pu https://orcid.org/0000-0001-9270-8812
Venkatessh Ramakrishnan https://orcid.org/0000-0002-9248-086X
Ramprasad Rao https://orcid.org/0000-0002-1407-7944
Mark G. Rawlings https://orcid.org/0000-0002-6529-202X
Alexander W. Raymond https://orcid.org/0000-0002-5779-4767
Luciano Rezzolla https://orcid.org/0000-0002-1330-7103
Angelo Ricarte https://orcid.org/0000-0001-5287-0452
Bart Ripperda https://orcid.org/0000-0002-7301-3908
Freek Roelofs https://orcid.org/0000-0001-5461-3687
Alan Rogers https://orcid.org/0000-0003-1941-7458
Eduardo Ros https://orcid.org/0000-0001-9503-4892
Cristina Romero-Cañizales https://orcid.org/0000-0001-6301-9073
Arash Roshanineshat https://orcid.org/0000-0002-8280-9238
Alan L. Roy https://orcid.org/0000-0002-1931-0135
Ignacio Ruiz https://orcid.org/0000-0002-0965-5463
Chet Ruszczyk https://orcid.org/0000-0001-7278-9707
Kazi L. J. Rygl https://orcid.org/0000-0003-4146-9043
Salvador Sánchez https://orcid.org/0000-0002-8042-5951
David Sánchez-Argüelles https://orcid.org/0000-0002-7344-9920

Miguel Sánchez-Portal https://orcid.org/0000-0003-0981-9664
Mahito Sasada https://orcid.org/0000-0001-5946-9960
Kaushik Satapathy https://orcid.org/0000-0003-0433-3585
Tuomas Savolainen https://orcid.org/0000-0001-6214-1085
Jonathan Schonfeld https://orcid.org/0000-0002-8909-2401
Karl-Friedrich Schuster https://orcid.org/0000-0003-2890-9454
Lijing Shao https://orcid.org/0000-0002-1334-8853
Zhiqiang Shen (沈志强) https://orcid.org/0000-0003-3540-8746
Des Small https://orcid.org/0000-0003-3723-5404
Bong Won Sohn https://orcid.org/0000-0002-4148-8378
Jason SooHoo https://orcid.org/0000-0003-1938-0720
Kamal Souccar https://orcid.org/0000-0001-7915-5272
He Sun (孙赫) https://orcid.org/0000-0003-1526-6787
Fumie Tazaki https://orcid.org/0000-0003-0236-0600
Alexandra J. Tetarenko https://orcid.org/0000-0003-3906-4354
Paul Tiede https://orcid.org/0000-0003-3826-5648
Remo P. J. Tilanus https://orcid.org/0000-0002-6514-553X
Michael Titus https://orcid.org/0000-0001-9001-3275
Pablo Torne https://orcid.org/0000-0001-8700-6058
Efthalia Traianou https://orcid.org/0000-0002-1209-6500
Sascha Trippe https://orcid.org/0000-0003-0465-1559
Matthew Turk https://orcid.org/0000-0002-5294-0198
Ilse van Bemmel https://orcid.org/0000-0001-5473-2950
Huib Jan van Langevelde https://orcid.org/0000-0002-0230-5946
Daniel R. van Rossum https://orcid.org/0000-0001-7772-6131
Jesse Vos https://orcid.org/0000-0003-3349-7394
Jan Wagner https://orcid.org/0000-0003-1105-6109
Derek Ward-Thompson https://orcid.org/0000-0003-1140-2761
John Wardle https://orcid.org/0000-0002-8960-2942
Jonathan Weintroub https://orcid.org/0000-0002-4603-5204
Norbert Wex https://orcid.org/0000-0003-4058-2837
Robert Wharton https://orcid.org/0000-0002-7416-5209
Maciek Wielgus https://orcid.org/0000-0002-8635-4242
Kaj Wiik https://orcid.org/0000-0002-0862-3398
Gunther Witzel https://orcid.org/0000-0003-2618-797X
Michael F. Wondrak https://orcid.org/0000-0002-6894-1072
George N. Wong https://orcid.org/0000-0001-6952-2147
Qingwen Wu (吴庆文) https://orcid.org/0000-0003-4773-4987
Paul Yamaguchi https://orcid.org/0000-0002-6017-8199
Doosoo Yoon https://orcid.org/0000-0001-8694-8166
André Young https://orcid.org/0000-0003-0000-2682
Ken Young https://orcid.org/0000-0002-3666-4920
Ziri Younsi https://orcid.org/0000-0001-9283-1191
Feng Yuan (袁峰) https://orcid.org/0000-0003-3564-6437
Ye-Fei Yuan (袁业飞) https://orcid.org/0000-0002-7330-4756
J. Anton Zensus https://orcid.org/0000-0001-7470-3321
Shuo Zhang https://orcid.org/0000-0002-2967-790X
Guang-Yao Zhao https://orcid.org/0000-0002-4417-1659
Shan-Shan Zhao (赵杉杉) https://orcid.org/0000-0002-9774-3606
Jay Blanchard https://orcid.org/0000-0002-2756-395X
Iain M. Coulson https://orcid.org/0000-0002-7316-4626
Nathalie Degenaar https://orcid.org/0000-0002-0092-3548
Sven Dornbusch https://orcid.org/0000-0003-3211-3352
Carlos A. Durán https://orcid.org/0000-0001-7622-3890
Karl Forster https://orcid.org/0000-0001-5800-5531
Ruben Herrero-Illana https://orcid.org/0000-0002-7758-8717
Caleb Kwon https://orcid.org/0000-0001-9006-7345
Robert Laing https://orcid.org/0000-0001-6786-3087
Hugo Messias https://orcid.org/0000-0002-2985-7994
Francisco Montenegro-Montes https://orcid.org/0000-0002-7430-3771
Dirk Muders https://orcid.org/0000-0002-2315-2571
Juan Pablo Pérez-Beaupuits https://orcid.org/0000-0003-3536-2274
Michael Poirier https://orcid.org/0000-0001-6641-0959
Mark Reynolds https://orcid.org/0000-0003-1621-9392
Alejandro F. Saez-Madain https://orcid.org/0000-0002-0804-3414
Don Sousa https://orcid.org/0000-0002-2625-2607
Rudy Wijnands https://orcid.org/0000-0002-3516-2152
Jan G. A. Wouterloot https://orcid.org/0000-0002-4694-6905

References

Alef, W., & Porcas, R. W. 1986, A&A, 168, 365
An, T., Goss, W. M., Zhao, J.-H., et al. 2005, ApJL, 634, L49
An, T., Sohn, B. W., & Imai, H. 2018, NatAs, 2, 118
Andrés, A., van den Eijnden, J., Degenaar, N., et al. 2022, MNRAS, 510, 2851
Backer, D. 1982, in Proc. IAU Symp. 97, Extragalactic Radio Sources, Radio Observations of the Galactic Center, ed. D. S. Heeschen & C. M. Wade (Dordrecht: Kluwer), 389
Baganoff, F. K., Bautz, M. W., Brandt, W. N., et al. 2001, Natur, 413, 45
Baganoff, F. K., Maeda, Y., Morris, M., et al. 2003, ApJ, 591, 891
Bardeen, J. M. 1973, in Black Holes (Les Astres Occlus) (New York: Gordon & Breach), 215
Blackburn, L., Chan, C.-k., Crew, G. B., et al. 2019, ApJ, 882, 23
Blackburn, L., Pesce, D. W., Johnson, M. D., et al. 2020, ApJ, 894, 31
Bower, G. C., Broderick, A., Dexter, J., et al. 2018, ApJ, 868, 101
Bower, G. C., Deller, A., Demorest, P., et al. 2014, ApJL, 780, L2
Bower, G. C., Dexter, J., Asada, K., et al. 2019, ApJL, 881, L2
Bower, G. C., Falcke, H., Herrnstein, R. M., et al. 2004, Sci, 304, 704
Bower, G. C., Goss, W. M., Falcke, H., Backer, D. C., & Lithwick, Y. 2006, ApJL, 648, L127
Bower, G. C., Markoff, S., Dexter, J., et al. 2015, ApJ, 802, 69
Boyce, H., Haggard, D., Witzel, G., et al. 2022, arXiv:2203.13311
Boyce, H., Haggard, D., Witzel, G., et al. 2019, ApJ, 871, 161
Brinkerink, C., Falcke, H., Brunthaler, A., & Law, C. 2021, arXiv:2107.13402
Brinkerink, C. D., Falcke, H., Law, C. J., et al. 2015, A&A, 576, A41
Broderick, A. E., & Pesce, D. W. 2020, ApJ, 904, 126
Burrows, D. N., Hill, J. E., Nousek, J. A., et al. 2005, SSRv, 120, 165
Butler, B. 2012, ALMA Memo Series 594, https://science.nrao.edu/facilities/alma/aboutALMA/Technology/ALMA_Memo_Series/alma594/abs594
Čadež, A., Calvani, M., & Kostić, U. 2008, A&A, 487, 527
Capellupo, D. M., Haggard, D., Choux, N., et al. 2017, ApJ, 845, 35
Cash, W. 1979, ApJ, 228, 939
Cho, I., Zhao, G.-Y., Kawashima, T., et al. 2022, ApJ, 926, 108
Ciurlo, A., Campbell, R. D., Morris, M. R., et al. 2020, Natur, 577, 337
Cotera, A., Morris, M., Ghez, A. M., et al. 1999, in ASP Conf. Ser. 186, The Central Parsecs of the Galaxy, ed. H. Falcke et al. (San Francisco, CA: ASP), 240
Coti Zelati, F., Rea, N., Papitto, A., et al. 2015, MNRAS, 449, 2685
Coti Zelati, F., Rea, N., Turolla, R., et al. 2017, MNRAS, 471, 1819
Cui, Y.-Z., Hada, K., Kino, M., et al. 2021, RAA, 21, 205
Davies, R. D., Walsh, D., & Booth, R. S. 1976, MNRAS, 177, 319
Degenaar, N., Miller, J. M., Kennea, J., et al. 2013, ApJ, 769, 155

Degenaar, N., Wijnands, R., Miller, J. M., et al. 2015, JHEAp, 7, 137
Deller, A. T., Brisken, W. F., Phillips, C. J., et al. 2011, PASP, 123, 275
Dexter, J., Deller, A., Bower, G. C., et al. 2017, MNRAS, 471, 3563
Dexter, J., Kelly, B., Bower, G. C., et al. 2014, MNRAS, 442, 2797
Do, T., Hees, A., Ghez, A., et al. 2019a, Sci, 365, 664
Do, T., Witzel, G., Gautam, A. K., et al. 2019b, ApJL, 882, L27
Dodds-Eden, K., Gillessen, S., Fritz, T. K., et al. 2011, ApJ, 728, 37
Dodds-Eden, K., Porquet, D., Trap, G., et al. 2009, ApJ, 698, 676
Doeleman, S. S., Weintroub, J., Rogers, A. E. E., et al. 2008, Natur, 455, 78
Doi, A., Fujisawa, K., Harada, K., et al. 2006, in Proc. of the 8th European VLBI Network Symp., Japanese VLBI Network, ed. B. Willem et al. (Sieste: SISSA), 71
Eatough, R. P., Falcke, H., Karuppusamy, R., et al. 2013, Natur, 501, 391
Event Horizon Telescope Collaboration, Akiyama, K., Alberdi, A., et al. 2019a, ApJL, 875, L1 (M87* Paper I)
Event Horizon Telescope Collaboration, Akiyama, K., Alberdi, A., et al. 2019b, ApJL, 875, L2 (M87* Paper II)
Event Horizon Telescope Collaboration, Akiyama, K., Alberdi, A., et al. 2019c, ApJL, 875, L3 (M87* Paper III)
Event Horizon Telescope Collaboration, Akiyama, K., Alberdi, A., et al. 2019d, ApJL, 875, L4 (M87* Paper IV)
Event Horizon Telescope Collaboration, Akiyama, K., Alberdi, A., et al. 2019e, ApJL, 875, L5 (M87* Paper V)
Event Horizon Telescope Collaboration, Akiyama, K., Alberdi, A., et al. 2019f, ApJL, 875, L6 (M87* Paper VI)
Event Horizon Telescope Collaboration, Akiyama, K., Alberdi, A., et al. 2021a, ApJL, 910, L12 (M87* Paper VII)
Event Horizon Telescope Collaboration, Akiyama, K., Alberdi, A., et al. 2021b, ApJL, 910, L13 (M87* Paper VIII)
Event Horizon Telescope Collaboration, Akiyama, K., Alberdi, A., et al. 2022a, ApJL, 930, L12 (Paper I)
Event Horizon Telescope Collaboration, Akiyama, K., Alberdi, A., et al. 2022b, ApJL, 930, L13 (Paper II)
Event Horizon Telescope Collaboration, Akiyama, K., Alberdi, A., et al. 2022c, ApJL, 930, L14 (Paper III)
Event Horizon Telescope Collaboration, Akiyama, K., Alberdi, A., et al. 2022d, ApJL, 930, L15 (Paper IV)
Event Horizon Telescope Collaboration, Akiyama, K., Alberdi, A., et al. 2022e, ApJL, 930, L16 (Paper V)
Event Horizon Telescope Collaboration, Akiyama, K., Alberdi, A., et al. 2022f, ApJL, 930, L17 (Paper VI)
Falcke, H., Goss, W. M., Matsuo, H., et al. 1998, ApJ, 499, 731
Falcke, H., & Markoff, S. B. 2013, CQGra, 30, 244003
Falcke, H., Melia, F., & Agol, E. 2000, ApJL, 528, L13
Fazio, G. G., Hora, J. L., Witzel, G., et al. 2018, ApJ, 864, 58
Fish, V. L., Doeleman, S. S., Beaudoin, C., et al. 2011, ApJL, 727, L36
Fish, V. L., Johnson, M. D., Doeleman, S. S., et al. 2016, ApJ, 820, 90
Frail, D. A., Diamond, P. J., Cordes, J. M., & van Langevelde, H. J. 1994, ApJ, 427, L43
Fruscione, A., McDowell, J. C., Allen, G. E., et al. 2006, Proc. SPIE, 6270, 62701V
Gehrels, N., Chincarini, G., Giommi, P., et al. 2004, ApJ, 611, 1005
Genzel, R., Eisenhauer, F., & Gillessen, S. 2010, RvMP, 82, 3121
Genzel, R., Schödel, R., Ott, T., et al. 2003, Natur, 425, 934
Ghez, A. M., Wright, S. A., Matthews, K., et al. 2004, ApJL, 601, L159
Gillessen, S., Genzel, R., Fritz, T. K., et al. 2012, Natur, 481, 51
Goddi, C., Martí-Vidal, I., Messias, H., et al. 2019, PASP, 131, 075003
Goddi, C., Martí-Vidal, I., Messias, H., et al. 2021, ApJL, 910, L14
Goodman, J., & Narayan, R. 1989, MNRAS, 238, 995
Gravity Collaboration, Abuter, R., Accardo, M., et al. 2017, A&A, 602, A94
Gravity Collaboration, Abuter, R., Amorim, A., et al. 2018, A&A, 618, L10
Gravity Collaboration, Abuter, R., Amorim, A., et al. 2019, A&A, 625, L10
Gravity Collaboration, Abuter, R., Amorim, A., et al. 2020, A&A, 638, A2
GRAVITY Collaboration, Abuter, R., Amorim, A., et al. 2021, A&A, 654, A22
Greisen, E. W. 2003, in Astrophysics and Space Science Library, Information Handling in Astronomy—Historical Vistas, AIPS, the VLA, and the VLBA 285, ed. A. Heck (Dordrecht: Kluwer), 109
Greve, A., Torres, M., Wink, J. E., et al. 1995, A&A, 299, L33
Gwinn, C. R., Kovalev, Y. Y., Johnson, M. D., & Soglasnov, V. A. 2014, ApJL, 794, L14
Haggard, D., Nynka, M., Mon, B., et al. 2019, ApJ, 886, 96
Hamaker, J. P., Bregman, J. D., & Sault, R. J. 1996, A&AS, 117, 137
Harrison, F. A., Craig, W. W., Christensen, F. E., et al. 2013, ApJ, 770, 103
Herrnstein, R. M., Zhao, J.-H., Bower, G. C., & Goss, W. M. 2004, AJ, 127, 3399
Issaoun, S., Folkers, T. W., Blackburn, L., et al. 2017, A conceptual overview of single-dish absolute amplitude calibration, Tech. Rep. 2017-CE-02, EHT Memo Series, (https://eventhorizontelescope.org/for-astronomers/memos)
Issaoun, S., Johnson, M. D., Blackburn, L., et al. 2019a, A&A, 629, A32
Issaoun, S., Johnson, M. D., Blackburn, L., et al. 2019b, ApJ, 871, 30
Issaoun, S., Johnson, M. D., Blackburn, L., et al. 2021, ApJ, 915, 99
Iwata, Y., Oka, T., Tsuboi, M., Miyoshi, M., & Takekawa, S. 2020, ApJL, 892, L30
Janssen, M., Blackburn, L., Issaoun, S., et al. 2019a, A Priori Calibration of EHT Stations, Tech. Rep. 2019-CE-01, EHT Memo Series, (https://eventhorizontelescope.org/for-astronomers/memos)
Janssen, M., Falcke, H., Kadler, M., et al. 2021, NatAs, 5, 1017
Janssen, M., Goddi, C., Falcke, H., et al. 2018, European VLBI Network Symp. & Users Meeting, RPICARD: A CASA-based Calibration Pipeline for VLBI Data 14 (Trieste: SISSA), 80
Janssen, M., Goddi, C., van Bemmel, I. M., et al. 2019b, A&A, 626, A75
Jauncey, D. L., Tzioumis, A. K., Preston, R. A., et al. 1989, AJ, 98, 44
Johnson, M. D., Fish, V. L., Doeleman, S. S., et al. 2015, Sci, 350, 1242
Johnson, M. D., & Gwinn, C. R. 2015, ApJ, 805, 180
Johnson, M. D., & Narayan, R. 2016, ApJ, 826, 170
Johnson, M. D., Narayan, R., Psaltis, D., et al. 2018, ApJ, 865, 104
Kim, J.-Y., Krichbaum, T. P., Broderick, A. E., et al. 2020, A&A, 640, A69
Kostić, U., Čadež, A., Calvani, M., & Gomboc, A. 2009, A&A, 496, 307
Krichbaum, T. P., Graham, D. A., Greve, A., et al. 1997, A&A, 323, L17
Krichbaum, T. P., Graham, D. A., Witzel, A., et al. 1998, A&A, 335, L106
Lee, S.-S., Petrov, L., Byun, D.-Y., et al. 2014, AJ, 147, 77
Li, Z., Morris, M. R., & Baganoff, F. K. 2013, ApJ, 779, 154
Liu, H. B., Wright, M. C. H., Zhao, J.-H., et al. 2016, A&A, 593, A107
Liu, S., Petrosian, V., & Melia, F. 2004, ApJL, 611, L101
Lo, K. Y., & Claussen, M. J. 1983, Natur, 306, 647
Lo, K. Y., Shen, Z.-Q., Zhao, J.-H., & Ho, P. T. P. 1998, ApJL, 508, L61
Lu, R.-S., Krichbaum, T. P., Roy, A. L., et al. 2018, ApJ, 859, 60
Macquart, J.-P., & Bower, G. C. 2006, ApJ, 641, 302
Marrone, D. P., Baganoff, F. K., Morris, M. R., et al. 2008, ApJ, 682, 373
Marrone, D. P., Moran, J. M., Zhao, J.-H., & Rao, R. 2006a, ApJ, 640, 308
Marrone, D. P., Moran, J. M., Zhao, J.-H., & Rao, R. 2006b, in Journal of Physics Conf. Ser. 54, Proc. of The Universe Under the Microscope - Astrophysics at High Angular Resolution, The Submillimeter Polarization of Sgr A*, ed. R. Schoedel et al. (Bristol: IOP Publishing), 354
Marrone, D. P., Moran, J. M., Zhao, J.-H., & Rao, R. 2007, ApJL, 654, L57
Martí-Vidal, I., Roy, A., Conway, J., & Zensus, A. J. 2016, A&A, 587, A143
Matthews, L. D., Crew, G. B., Doeleman, S. S., et al. 2018, PASP, 130, 015002
McMullin, J. P., Waters, B., Schiebel, D., Young, W., & Golap, K. 2007, in ASP Conf. Ser. 376, Astronomical Data Analysis Software and Systems XVI, ed. R. A. Shaw, F. Hill, & D. J. Bell (San Francisco, CA: ASP), 127
Michail, J. M., Wardle, M., Yusef-Zadeh, F., & Kunneriath, D. 2021, ApJ, 923, 54
Miyazaki, A., Tsutsumi, T., & Tsuboi, M. 2004, ApJL, 611, L97
Mori, K., Gotthelf, E. V., Zhang, S., et al. 2013, ApJL, 770, L23
Morris, M. R., Meyer, L., & Ghez, A. M. 2012, RAA, 12, 995
Narayan, R. 1992, RSPTA, 341, 151
Neilsen, J., Markoff, S., Nowak, M. A., et al. 2015, ApJ, 799, 199
Neilsen, J., Nowak, M. A., Gammie, C., et al. 2013, ApJ, 774, 42
Niinuma, K., Lee, S.-S., Kino, M., & Sohn, B. W. 2015, PKAS, 30, 637
Nowak, M. A., Neilsen, J., Markoff, S. B., et al. 2012, ApJ, 759, 95
Padin, S., Woody, D. P., Hodges, M. W., et al. 1990, ApJL, 360, L11
Peißker, F., Zajaček, M., Eckart, A., et al. 2021, ApJ, 923, 69
Ponti, G., George, E., Scaringi, S., et al. 2017, MNRAS, 468, 2447
Porquet, D., Grosso, N., Predehl, P., et al. 2008, A&A, 488, 549
Primiani, R. A., Young, K. H., Young, A., et al. 2016, JAI, 5, 1641006
Psaltis, D., Johnson, M., Narayan, R., et al. 2018, arXiv:1805.01242
Quataert, E. 2002, ApJ, 575, 855
Rauch, C., Ros, E., Krichbaum, T. P., et al. 2016, A&A, 587, A37
Rea, N., Coti Zelati, F., Viganò, D., et al. 2020, ApJ, 894, 159
Rea, N., Esposito, P., Pons, J. A., et al. 2013, ApJL, 775, L34
Reid, M. J., & Brunthaler, A. 2004, ApJ, 616, 872
Reid, M. J., & Brunthaler, A. 2020, ApJ, 892, 39
Rickett, B. J. 1990, ARA&A, 28, 561
Roelofs, F., Johnson, M. D., Shiokawa, H., Doeleman, S. S., & Falcke, H. 2017, ApJ, 847, 55
Scargle, J. D. 1998, ApJ, 504, 405
Scargle, J. D., Norris, J. P., Jackson, B., & Chiang, J. 2013, ApJ, 764, 167
Schödel, R., Morris, M. R., Muzic, K., et al. 2011, A&A, 532, A83
Schwab, F. R., & Cotton, W. D. 1983, AJ, 88, 688
Serabyn, E., Carlstrom, J., Lay, O., et al. 1997, ApJL, 490, L77
Shcherbakov, R. V., Penna, R. F., & McKinney, J. C. 2012, ApJ, 755, 133

Shen, Z.-Q., Lo, K. Y., Liang, M.-C., Ho, P. T. P., & Zhao, J.-H. 2005, Natur, 438, 62
Smirnov, O. M. 2011a, A&A, 527, A106
Smirnov, O. M. 2011b, A&A, 527, A107
Smirnov, O. M. 2011c, A&A, 527, A108
Smirnov, O. M. 2011d, A&A, 531, A159
Steel, S., Wielgus, M., Blackburn, L., Issaoun, S., & Johnson, M. 2019, EHT Memo Series, 2019-CE-03, https://eventhorizontelescope.org/files/eht/files/EHT_memo_Steel_2019-CE-03.pdf
Stone, J. M., Marrone, D. P., Dowell, C. D., et al. 2016, ApJ, 825, 32
Su, M., & Finkbeiner, D. P. 2012, ApJ, 753, 61
Telesco, C. M., Davidson, J. A., & Werner, M. W. 1996, ApJ, 456, 541
Thompson, A. R., Moran, J. M., & Swenson, G. W., Jr. 2017, Interferometry and Synthesis in Radio Astronomy (Berlin: Springer)
van Bemmel, I., Small, D., Kettenis, M., et al. 2019, arXiv:1904.11747
van Langevelde, H. J., Frail, D. A., Cordes, J. M., & Diamond, P. J. 1992, ApJ, 396, 686
Verner, D. A., Ferland, G. J., Korista, K. T., & Yakovlev, D. G. 1996, ApJ, 465, 487
Vertatschitsch, L., Primiani, R., Young, A., et al. 2015, PASP, 127, 1226
von Fellenberg, S. D., Gillessen, S., Graciá-Carpio, J., et al. 2018, ApJ, 862, 129
Wajima, K., Hagiwara, Y., An, T., et al. 2016, in ASP Conf. Ser. 502, The East-Asian VLBI Network, ed. L. Qain & D. Li (San Francisco, CA: ASP), 81
Wang, Q. D., Nowak, M. A., Markoff, S. B., et al. 2013, Sci, 341, 981
Weisskopf, M. C., Brinkman, B., Canizares, C., et al. 2002, PASP, 114, 1
Whitney, A. R., Beaudoin, C. J., Cappallo, R. J., et al. 2013, PASP, 125, 196
Whitney, A. R., Cappallo, R., Aldrich, W., et al. 2004, RaSc, 39, RS1007
Wielgus, M., Blackburn, L., Issaoun, S., et al. 2019, EHT data set validation and characterization of errors, Tech. Rep. 2019-CE-02, EHT Memo Series, https://eventhorizontelescope.org/for-astronomers/memos
Wielgus, M., Marchili, N., Martí-Vidal, I., et al. 2022, ApJL, 930, L19
Williams, P. K. G., Clavel, M., Newton, E., & Ryzhkov, D. 2017, pwkit: Astronomical utilities in Python, Astrophysics Source Code Library, ascl:1704.001
Wilms, J., Allen, A., & McCray, R. 2000, ApJ, 542, 914
Witzel, G., Eckart, A., Bremer, M., et al. 2012, ApJS, 203, 18
Witzel, G., Martinez, G., Hora, J., et al. 2018, ApJ, 863, 15
Witzel, G., Martinez, G., Willner, S. P., et al. 2021, ApJ, 917, 73
Wright, M. C. H., Genzel, R., Güsten, R., & Jaffe, D. T. 1987, in AIP Conf. Ser. 155, The Galactic Center, ed. D. C. Backer (New York: AIP), 133
Young, A., Primiani, R., Weintroub, J., et al. 2016, in IEEE International Symp. on Phased Array Systems and Technology (PAST), Performance assessment of an adaptive beamformer for the submillimeter array (Piscataway, NJ: IEEE)
Yuan, F., Quataert, E., & Narayan, R. 2003, ApJ, 598, 301
Yusef-Zadeh, F., Arendt, R., Bushouse, H., et al. 2012, ApJL, 758, L11
Yusef-Zadeh, F., Bushouse, H., Schödel, R., et al. 2015, ApJ, 809, 10
Yusef-Zadeh, F., Morris, M., & Ekers, R. D. 1990, Natur, 348, 45
Yusef-Zadeh, F., Wardle, M., Miller-Jones, J. C. A., et al. 2011, ApJ, 729, 44
Zhang, S., Baganoff, F. K., Ponti, G., et al. 2017, ApJ, 843, 96
Zhao, J.-H., Young, K. H., Herrnstein, R. M., et al. 2003, ApJL, 586, L29
Zheng, W. 2015, IAUGA, 29, 2255896
Zhu, Z., Li, Z., Morris, M. R., Zhang, S., & Liu, S. 2019, ApJ, 875, 44
Zubovas, K., Nayakshin, S., & Markoff, S. 2012, MNRAS, 421, 1315
Zylka, R., & Mezger, P. G. 1988, A&A, 190, L25
Zylka, R., Mezger, P. G., & Lesch, H. 1992, A&A, 261, 119
Zylka, R., Mezger, P. G., Ward-Thompson, D., Duschl, W. J., & Lesch, H. 1995, A&A, 297, 83

Event Horizon Telescope Collaboration,
Kazunori Akiyama[1,2,3], Antxon Alberdi[4], Walter Alef[5], Juan Carlos Algaba[6], Richard Anantua[3,7,8], Keiichi Asada[9], Rebecca Azulay[5,10,11], Uwe Bach[5], Anne-Kathrin Baczko[5], David Ball[12], Mislav Baloković[13], John Barrett[1], Michi Bauböck[14], Bradford A. Benson[15,16], Dan Bintley[17,18], Lindy Blackburn[3,7], Raymond Blundell[7], Katherine L. Bouman[19], Geoffrey C. Bower[20,21], Hope Boyce[22,23], Michael Bremer[24], Christiaan D. Brinkerink[25], Roger Brissenden[3,7], Silke Britzen[5], Avery E. Broderick[26,27,28], Dominique Broguiere[24], Thomas Bronzwaer[25], Sandra Bustamante[29], Do-Young Byun[30,31], John E. Carlstrom[16,32,33,34], Chiara Ceccobello[35], Andrew Chael[36,37], Chi-kwan Chan[12,38,39], Koushik Chatterjee[3,7], Shami Chatterjee[40], Ming-Tang Chen[20], Yongjun Chen (陈永军)[41,42], Xiaopeng Cheng[30], Ilje Cho[4], Pierre Christian[43], Nicholas S. Conroy[7,44], John E. Conway[35], James M. Cordes[40], Thomas M. Crawford[16,32], Geoffrey B. Crew[1], Alejandro Cruz-Osorio[45], Yuzhu Cui (崔玉竹)[46,47,48], Jordy Davelaar[25,49,50], Mariafelicia De Laurentis[45,51,52], Roger Deane[53,54,55], Jessica Dempsey[17,18,56], Gregory Desvignes[5,57], Jason Dexter[58], Vedant Dhruv[14], Sheperd S. Doeleman[3,7], Sean Dougal[12], Sergio A. Dzib[5,24], Ralph P. Eatough[5,59], Razieh Emami[7], Heino Falcke[25], Joseph Farah[60,61], Vincent L. Fish[1], Ed Fomalont[62], H. Alyson Ford[12], Raquel Fraga-Encinas[25], William T. Freeman[63,64], Per Friberg[17,18], Christian M. Fromm[5,45,65], Antonio Fuentes[4], Peter Galison[3,66,67], Charles F. Gammie[14,44,68], Roberto García[24], Olivier Gentaz[24], Boris Georgiev[26,27,28], Ciriaco Goddi[69,70], Roman Gold[45,71], Arturo I. Gómez-Ruiz[72,73], José L. Gómez[4], Minfeng Gu (顾敏峰)[41,74], Mark Gurwell[7], Kazuhiro Hada[47,48], Daryl Haggard[22,23], Kari Haworth[7], Michael H. Hecht[1], Ronald Hesper[75], Dirk Heumann[12], Luis C. Ho (何子山)[76,77], Paul Ho[9,17,18], Mareki Honma[47,48,78], Chih-Wei L. Huang[9], Lei Huang (黄磊)[41,74], David H. Hughes[72], Shiro Ikeda[2,79,80,81], C. M. Violette Impellizzeri[62,82], Makoto Inoue[9], Sara Issaoun[7,37], David J. James[83], Buell T. Jannuzi[12], Michael Janssen[5], Britton Jeter[9], Wu Jiang (江悟)[41], Alejandra Jiménez-Rosales[25], Michael D. Johnson[3,7], Svetlana Jorstad[84], Abhishek V. Joshi[14], Taehyun Jung[30,31], Mansour Karami[26,27], Ramesh Karuppusamy[5], Tomohisa Kawashima[85], Garrett K. Keating[7], Mark Kettenis[86], Dong-Jin Kim[5], Jae-Young Kim[5,30,87], Jongsoo Kim[30], Junhan Kim[12,19], Motoki Kino[2,88], Jun Yi Koay[9], Prashant Kocherlakota[45], Yutaro Kofuji[47,78], Patrick M. Koch[9], Shoko Koyama[9,89], Carsten Kramer[24], Michael Kramer[5], Thomas P. Krichbaum[5], Cheng-Yu Kuo[9,90], Noemi La Bella[25], Tod R. Lauer[91], Daeyoung Lee[14], Sang-Sung Lee[30], Po Kin Leung[92], Aviad Levis[19], Zhiyuan Li (李志远)[93,94], Rocco Lico[4,95], Greg Lindahl[7], Michael Lindqvist[35], Mikhail Lisakov[5], Jun Liu (刘俊)[5], Kuo Liu[5], Elisabetta Liuzzo[96], Wen-Ping Lo[9,97], Andrei P. Lobanov[5], Laurent Loinard[98,99],

Colin J. Lonsdale[1], Ru-Sen Lu (路如森)[5,41,42], Jirong Mao (毛基荣)[100,101,102], Nicola Marchili[5,96], Sera Markoff[103,104], Daniel P. Marrone[12], Alan P. Marscher[84], Iván Martí-Vidal[10,11], Satoki Matsushita[9], Lynn D. Matthews[1], Lia Medeiros[12,105,106], Karl M. Menten[5], Daniel Michalik[16,107], Izumi Mizuno[17,18], Yosuke Mizuno[45,46,108], James M. Moran[3,7], Kotaro Moriyama[1,45,47], Monika Moscibrodzka[25], Cornelia Müller[5,25], Alejandro Mus[10,11], Gibwa Musoke[25,103], Ioannis Myserlis[109], Andrew Nadolski[44], Hiroshi Nagai[2,48], Neil M. Nagar[110], Masanori Nakamura[9,111], Ramesh Narayan[3,7], Gopal Narayanan[29], Iniyan Natarajan[53,112], Antonios Nathanail[45,113], Santiago Navarro Fuentes[109], Joey Neilsen[114], Roberto Neri[24], Chunchong Ni[26,27,28], Aristeidis Noutsos[5], Michael A. Nowak[115], Junghwan Oh[116], Hiroki Okino[47,78], Héctor Olivares[25], Gisela N. Ortiz-León[5,99], Tomoaki Oyama[47], Feryal Özel[12], Daniel C. M. Palumbo[3,7], Georgios Filippos Paraschos[5], Jongho Park[9,117], Harriet Parsons[17,18], Nimesh Patel[7], Ue-Li Pen[9,26,118,119,120], Dominic W. Pesce[3,7], Vincent Piétu[24], Richard Plambeck[121], Aleksandar PopStefanija[29], Oliver Porth[45,103], Felix M. Pötzl[5,122], Ben Prather[14], Jorge A. Preciado-López[26], Dimitrios Psaltis[12], Hung-Yi Pu[9,123,124], Venkatessh Ramakrishnan[110,125,126], Ramprasad Rao[7], Mark G. Rawlings[17,18,127], Alexander W. Raymond[3,7], Luciano Rezzolla[45,128,129], Angelo Ricarte[3,7], Bart Ripperda[50,130], Freek Roelofs[3,7,25], Alan Rogers[1], Eduardo Ros[5], Cristina Romero-Cañizales[9], Arash Roshanineshat[12], Helge Rottmann[5], Alan L. Roy[5], Ignacio Ruiz[109], Chet Ruszczyk[1], Kazi L. J. Rygl[96], Salvador Sánchez[109], David Sánchez-Argüelles[72,73], Miguel Sánchez-Portal[109], Mahito Sasada[47,131,132], Kaushik Satapathy[12], Tuomas Savolainen[5,126,133], F. Peter Schloerb[29], Jonathan Schonfeld[7], Karl-Friedrich Schuster[24], Lijing Shao[5,77], Zhiqiang Shen (沈志强)[41,42], Des Small[86], Bong Won Sohn[30,31,134], Jason SooHoo[1], Kamal Souccar[29], He Sun (孙赫)[19], Fumie Tazaki[47], Alexandra J. Tetarenko[37,135], Paul Tiede[3,7], Remo P. J. Tilanus[12,25,82,136], Michael Titus[1], Pablo Torne[5,109], Efthalia Traianou[4,5], Tyler Trent[12], Sascha Trippe[137], Matthew Turk[44], Ilse van Bemmel[86], Huib Jan van Langevelde[82,86,138], Daniel R. van Rossum[25], Jesse Vos[25], Jan Wagner[5], Derek Ward-Thompson[139], John Wardle[140], Jonathan Weintroub[3,7], Norbert Wex[5], Robert Wharton[5], Maciek Wielgus[5], Kaj Wiik[141], Gunther Witzel[5], Michael F. Wondrak[25,142], George N. Wong[106,143], Qingwen Wu (吴庆文)[144], Paul Yamaguchi[7], Doosoo Yoon[103], André Young[25], Ken Young[7], Ziri Younsi[45,145], Feng Yuan (袁峰)[41,74,146], Ye-Fei Yuan (袁业飞)[147], J. Anton Zensus[5], Shuo Zhang[148], Guang-Yao Zhao[4], Shan-Shan Zhao (赵杉杉)[41], Claudio Agurto[149], Juan Pablo Araneda[149], Oriel Arriagada[149], Alessandra Bertarini[5,150], Ryan Berthold[17,18], Jay Blanchard[151], Ken Brown[17,18], Mauricio Cárdenas[149], Michael Cantzler[149], Patricio Caro[149], Tim C. Chuter[17,18], Miroslaw Ciechanowicz[5,149], Iain M. Coulson[17,18], Joseph Crowley[1], Nathalie Degenaar[103], Sven Dornbusch[5], Carlos A. Durán[149], Karl Forster[152], Gertie Geertsema[153], Edouard González[149], Dave Graham[5], Frédéric Gueth[24], Chih-Chiang Han[9], Cristian Herrera[149], Ruben Herrero-Illana[149], Stefan Heyminck[5], James Hoge[17,18], Yau-De Huang[9], Homin Jiang[9], David John[109], Thomas Klein[149], Derek Kubo[20], John Kuroda[17,18], Caleb Kwon[114], Robert Laing[155,156], Ching-Tang Liu[9], Kuan-Yu Liu[9,17,18], Felipe Mac-Auliffe[149], Pierre Martin-Cocher[9], Callie Matulonis[17,18], Hugo Messias[149,154], Zheng Meyer-Zhao[56], Francisco Montenegro-Montes[149], William Montgomerie[17,18,157], Dirk Muders[5], Hiroaki Nishioka[9], Timothy J. Norton[7], Rodrigo Olivares[149], Juan Pablo Pérez-Beaupuits[5,149,158], Rodrigo Parra[149], Michael Poirier[1], Nicolas Pradel[9], Philippe A. Raffin[20], Jorge Ramírez[149], Mark Reynolds[159], Alejandro F. Saez-Madain[154,160], Jorge Santana[149], Kevin M. Silva[17,18], Don Sousa[1], William Stahm[17,18], Karl Torstensson[149], Paulina Venegas[149], Craig Walther[17,18], Gundolf Wieching[5], Rudy Wijnands[103], and Jan G. A. Wouterloot[17,18]

[1] Massachusetts Institute of Technology Haystack Observatory, 99 Millstone Road, Westford, MA 01886, USA
[2] National Astronomical Observatory of Japan, 2-21-1 Osawa, Mitaka, Tokyo 181-8588, Japan
[3] Black Hole Initiative at Harvard University, 20 Garden Street, Cambridge, MA 02138, USA
[4] Instituto de Astrofísica de Andalucía-CSIC, Glorieta de la Astronomía s/n, E-18008 Granada, Spain
[5] Max-Planck-Institut für Radioastronomie, Auf dem Hügel 69, D-53121 Bonn, Germany
[6] Department of Physics, Faculty of Science, Universiti Malaya, 50603 Kuala Lumpur, Malaysia
[7] Center for Astrophysics | Harvard & Smithsonian, 60 Garden Street, Cambridge, MA 02138, USA
[8] Department of Physics & Astronomy, The University of Texas at San Antonio, One UTSA Circle, San Antonio, TX 78249, USA
[9] Institute of Astronomy and Astrophysics, Academia Sinica, 11F of Astronomy-Mathematics Building, AS/NTU No. 1, Sec. 4, Roosevelt Rd., Taipei 10617, Taiwan, R.O.C.
[10] Departament d'Astronomia i Astrofísica, Universitat de València, C. Dr. Moliner 50, E-46100 Burjassot, València, Spain
[11] Observatori Astronòmic, Universitat de València, C. Catedrático José Beltrán 2, E-46980 Paterna, València, Spain
[12] Steward Observatory and Department of Astronomy, University of Arizona, 933 N. Cherry Ave., Tucson, AZ 85721, USA
[13] Yale Center for Astronomy & Astrophysics, Yale University, 52 Hillhouse Avenue, New Haven, CT 06511, USA
[14] Department of Physics, University of Illinois, 1110 West Green Street, Urbana, IL 61801, USA
[15] Fermi National Accelerator Laboratory, MS209, P.O. Box 500, Batavia, IL 60510, USA
[16] Department of Astronomy and Astrophysics, University of Chicago, 5640 South Ellis Avenue, Chicago, IL 60637, USA
[17] East Asian Observatory, 660 N. A'ohoku Place, Hilo, HI 96720, USA
[18] James Clerk Maxwell Telescope (JCMT), 660 N. A'ohoku Place, Hilo, HI 96720, USA
[19] California Institute of Technology, 1200 East California Boulevard, Pasadena, CA 91125, USA
[20] Institute of Astronomy and Astrophysics, Academia Sinica, 645 N. A'ohoku Place, Hilo, HI 96720, USA
[21] Department of Physics and Astronomy, University of Hawaii at Manoa, 2505 Correa Road, Honolulu, HI 96822, USA
[22] Department of Physics, McGill University, 3600 rue University, Montréal, QC H3A 2T8, Canada
[23] McGill Space Institute, McGill University, 3550 rue University, Montréal, QC H3A 2A7, Canada

[24] Institut de Radioastronomie Millimétrique (IRAM), 300 rue de la Piscine, F-38406 Saint Martin d'Hères, France
[25] Department of Astrophysics, Institute for Mathematics, Astrophysics and Particle Physics (IMAPP), Radboud University, P.O. Box 9010, 6500 GL Nijmegen, The Netherlands
[26] Perimeter Institute for Theoretical Physics, 31 Caroline Street N, Waterloo, ON N2L 2Y5, Canada
[27] Department of Physics and Astronomy, University of Waterloo, 200 University Avenue W, Waterloo, ON N2L 3G1, Canada
[28] Waterloo Centre for Astrophysics, University of Waterloo, Waterloo, ON N2L 3G1, Canada
[29] Department of Astronomy, University of Massachusetts, Amherst, MA 01003, USA
[30] Korea Astronomy and Space Science Institute, Daedeok-daero 776, Yuseong-gu, Daejeon 34055, Republic Of Korea
[31] University of Science and Technology, Gajeong-ro 217, Yuseong-gu, Daejeon 34113, Republic Of Korea
[32] Kavli Institute for Cosmological Physics, University of Chicago, 5640 South Ellis Avenue, Chicago, IL 60637, USA
[33] Department of Physics, University of Chicago, 5720 South Ellis Avenue, Chicago, IL 60637, USA
[34] Enrico Fermi Institute, University of Chicago, 5640 South Ellis Avenue, Chicago, IL 60637, USA
[35] Department of Space, Earth and Environment, Chalmers University of Technology, Onsala Space Observatory, SE-43992 Onsala, Sweden
[36] Princeton Center for Theoretical Science, Jadwin Hall, Princeton University, Princeton, NJ 08544, USA
[37] NASA Hubble Fellowship Program, Einstein Fellow
[38] Data Science Institute, University of Arizona, 1230 N. Cherry Ave., Tucson, AZ 85721, USA
[39] Program in Applied Mathematics, University of Arizona, 617 N. Santa Rita, Tucson, AZ 85721,USA
[40] Cornell Center for Astrophysics and Planetary Science, Cornell University, Ithaca, NY 14853, USA
[41] Shanghai Astronomical Observatory, Chinese Academy of Sciences, 80 Nandan Road, Shanghai 200030, People's Republic of China
[42] Key Laboratory of Radio Astronomy, Chinese Academy of Sciences, Nanjing 210008, People's Republic of China
[43] Physics Department, Fairfield University, 1073 North Benson Road, Fairfield, CT 06824, USA
[44] Department of Astronomy, University of Illinois at Urbana-Champaign, 1002 West Green Street, Urbana, IL 61801, USA
[45] Institut für Theoretische Physik, Goethe-Universität Frankfurt, Max-von-Laue-Straße 1, D-60438 Frankfurt am Main, Germany
[46] Tsung-Dao Lee Institute, Shanghai Jiao Tong University, Shengrong Road 520, Shanghai, 201210, People's Republic of China
[47] Mizusawa VLBI Observatory, National Astronomical Observatory of Japan, 2-12 Hoshigaoka, Mizusawa, Oshu, Iwate 023-0861, Japan
[48] Department of Astronomical Science, The Graduate University for Advanced Studies (SOKENDAI), 2-21-1 Osawa, Mitaka, Tokyo 181-8588, Japan
[49] Department of Astronomy and Columbia Astrophysics Laboratory, Columbia University, 550 W. 120th Street, New York, NY 10027, USA
[50] Center for Computational Astrophysics, Flatiron Institute, 162 Fifth Avenue, New York, NY 10010, USA
[51] Dipartimento di Fisica "E. Pancini," Universitá di Napoli "Federico II," Compl. Univ. di Monte S. Angelo, Edificio G, Via Cinthia, I-80126, Napoli, Italy
[52] INFN Sez. di Napoli, Compl. Univ. di Monte S. Angelo, Edificio G, Via Cinthia, I-80126, Napoli, Italy
[53] Wits Centre for Astrophysics, University of the Witwatersrand, 1 Jan Smuts Avenue, Braamfontein, Johannesburg 2050, South Africa
[54] Department of Physics, University of Pretoria, Hatfield, Pretoria 0028, South Africa
[55] Centre for Radio Astronomy Techniques and Technologies, Department of Physics and Electronics, Rhodes University, Makhanda 6140, South Africa
[56] ASTRON, Oude Hoogeveensedijk 4, 7991 PD Dwingeloo, The Netherlands
[57] LESIA, Observatoire de Paris, Université PSL, CNRS, Sorbonne Université, Université de Paris, 5 place Jules Janssen, F-92195 Meudon, France
[58] JILA and Department of Astrophysical and Planetary Sciences, University of Colorado, Boulder, CO 80309, USA
[59] National Astronomical Observatories, Chinese Academy of Sciences, 20A Datun Road, Chaoyang District, Beijing 100101, People's Republic of China
[60] Las Cumbres Observatory, 6740 Cortona Drive, Suite 102, Goleta, CA 93117-5575, USA
[61] Department of Physics, University of California, Santa Barbara, CA 93106-9530, USA
[62] National Radio Astronomy Observatory, 520 Edgemont Road, Charlottesville, VA 22903, USA
[63] Department of Electrical Engineering and Computer Science, Massachusetts Institute of Technology, 32-D476, 77 Massachusetts Ave., Cambridge, MA 02142, USA
[64] Google Research, 355 Main St., Cambridge, MA 02142, USA
[65] Institut für Theoretische Physik und Astrophysik, Universität Würzburg, Emil-Fischer-Str. 31, D-97074 Würzburg, Germany
[66] Department of History of Science, Harvard University, Cambridge, MA 02138, USA
[67] Department of Physics, Harvard University, Cambridge, MA 02138, USA
[68] NCSA, University of Illinois, 1205 W. Clark St., Urbana, IL 61801, USA
[69] Dipartimento di Fisica, Università degli Studi di Cagliari, SP Monserrato-Sestu km 0.7, I-09042 Monserrato, Italy
[70] INAF—Osservatorio Astronomico di Cagliari, Via della Scienza 5, I-09047, Selargius, CA, Italy
[71] CP3-Origins, University of Southern Denmark, Campusvej 55, DK-5230 Odense M, Denmark
[72] Instituto Nacional de Astrofísica, Óptica y Electrónica. Apartado Postal 51 y 216, 72000. Puebla Pue., México
[73] Consejo Nacional de Ciencia y Tecnologìa, Av. Insurgentes Sur 1582, 03940, Ciudad de México, México
[74] Key Laboratory for Research in Galaxies and Cosmology, Chinese Academy of Sciences, Shanghai 200030, People's Republic of China
[75] NOVA Sub-mm Instrumentation Group, Kapteyn Astronomical Institute, University of Groningen, Landleven 12, 9747 AD Groningen, The Netherlands
[76] Department of Astronomy, School of Physics, Peking University, Beijing 100871, People's Republic of China
[77] Kavli Institute for Astronomy and Astrophysics, Peking University, Beijing 100871, People's Republic of China
[78] Department of Astronomy, Graduate School of Science, The University of Tokyo, 7-3-1 Hongo, Bunkyo-ku, Tokyo 113-0033, Japan
[79] The Institute of Statistical Mathematics, 10-3 Midori-cho, Tachikawa, Tokyo, 190-8562, Japan
[80] Department of Statistical Science, The Graduate University for Advanced Studies (SOKENDAI), 10-3 Midori-cho, Tachikawa, Tokyo 190-8562, Japan
[81] Kavli Institute for the Physics and Mathematics of the Universe, The University of Tokyo, 5-1-5 Kashiwanoha, Kashiwa, 277-8583, Japan
[82] Leiden Observatory, Leiden University, Postbus 2300, 9513 RA Leiden, The Netherlands
[83] ASTRAVEO LLC, PO Box 1668, Gloucester, MA 01931, USA
[84] Institute for Astrophysical Research, Boston University, 725 Commonwealth Ave., Boston, MA 02215, USA
[85] Institute for Cosmic Ray Research, The University of Tokyo, 5-1-5 Kashiwanoha, Kashiwa, Chiba 277-8582, Japan
[86] Joint Institute for VLBI ERIC (JIVE), Oude Hoogeveensedijk 4, 7991 PD Dwingeloo, The Netherlands
[87] Department of Astronomy and Atmospheric Sciences, Kyungpook National University, Daegu 702-701, Republic Of Korea
[88] Kogakuin University of Technology & Engineering, Academic Support Center, 2665-1 Nakano, Hachioji, Tokyo 192-0015, Japan
[89] Niigata University, 8050 Ikarashi-nino-cho, Nishi-ku, Niigata 950-2181, Japan
[90] Physics Department, National Sun Yat-Sen University, No. 70, Lien-Hai Road, Kaosiung City 80424, Taiwan, R.O.C.
[91] National Optical Astronomy Observatory, 950 N. Cherry Ave., Tucson, AZ 85719, USA
[92] Department of Physics, The Chinese University of Hong Kong, Shatin, N.T., Hong Kong
[93] School of Astronomy and Space Science, Nanjing University, Nanjing 210023, People's Republic of China
[94] Key Laboratory of Modern Astronomy and Astrophysics, Nanjing University, Nanjing 210023, People's Republic of China
[95] INAF-Istituto di Radioastronomia, Via P. Gobetti 101, I-40129 Bologna, Italy
[96] INAF-Istituto di Radioastronomia & Italian ALMA Regional Centre, Via P. Gobetti 101, I-40129 Bologna, Italy

[97] Department of Physics, National Taiwan University, No. 1, Sec. 4, Roosevelt Rd., Taipei 10617, Taiwan, R.O.C
[98] Instituto de Radioastronomía y Astrofísica, Universidad Nacional Autónoma de México, Morelia 58089, México
[99] Instituto de Astronomía, Universidad Nacional Autónoma de México (UNAM), Apdo Postal 70-264, Ciudad de México, México
[100] Yunnan Observatories, Chinese Academy of Sciences, 650011 Kunming, Yunnan Province, People's Republic of China
[101] Center for Astronomical Mega-Science, Chinese Academy of Sciences, 20A Datun Road, Chaoyang District, Beijing, 100012, People's Republic of China
[102] Key Laboratory for the Structure and Evolution of Celestial Objects, Chinese Academy of Sciences, 650011 Kunming, People's Republic of China
[103] Anton Pannekoek Institute for Astronomy, University of Amsterdam, Science Park 904, 1098 XH, Amsterdam, The Netherlands
[104] Gravitation and Astroparticle Physics Amsterdam (GRAPPA) Institute, University of Amsterdam, Science Park 904, 1098 XH Amsterdam, The Netherlands
[105] NSF Astronomy and Astrophysics Postdoctoral Fellow
[106] School of Natural Sciences, Institute for Advanced Study, 1 Einstein Drive, Princeton, NJ 08540, USA
[107] Science Support Office, Directorate of Science, European Space Research and Technology Centre (ESA/ESTEC), Keplerlaan 1, 2201 AZ Noordwijk, The Netherlands
[108] School of Physics and Astronomy, Shanghai Jiao Tong University, 800 Dongchuan Road, Shanghai, 200240, People's Republic of China
[109] Institut de Radioastronomie Millimétrique (IRAM), Avenida Divina Pastora 7, Local 20, E-18012, Granada, Spain
[110] Astronomy Department, Universidad de Concepción, Casilla 160-C, Concepción, Chile
[111] National Institute of Technology, Hachinohe College, 16-1 Uwanotai, Tamonoki, Hachinohe City, Aomori 039-1192, Japan
[112] South African Radio Astronomy Observatory, Observatory 7925, Cape Town, South Africa
[113] Department of Physics, National and Kapodistrian University of Athens, Panepistimiopolis, GR 15783 Zografos, Greece
[114] Department of Physics, Villanova University, 800 Lancaster Avenue, Villanova, PA 19085, USA
[115] Physics Department, Washington University CB 1105, St. Louis, MO 63130, USA
[116] Sejong University, 209 Neungdong-ro, Gwangjin-gu, Seoul, Republic Of Korea
[117] EACOA Fellow
[118] Canadian Institute for Theoretical Astrophysics, University of Toronto, 60 St. George Street, Toronto, ON M5S 3H8, Canada
[119] Dunlap Institute for Astronomy and Astrophysics, University of Toronto, 50 St. George Street, Toronto, ON M5S 3H4, Canada
[120] Canadian Institute for Advanced Research, 180 Dundas St. W, Toronto, ON M5G 1Z8, Canada
[121] Radio Astronomy Laboratory, University of California, Berkeley, CA 94720, USA
[122] Department of Physics, University College Cork, Kane Building, College Road, Cork T12 K8AF, Ireland
[123] Department of Physics, National Taiwan Normal University, No. 88, Sec. 4, Tingzhou Rd., Taipei 116, Taiwan, R.O.C.
[124] Center of Astronomy and Gravitation, National Taiwan Normal University, No. 88, Section 4, Tingzhou Road, Taipei 116, Taiwan, R.O.C.
[125] Finnish Centre for Astronomy with ESO, University of Turku, FI-20014, Finland
[126] Aalto University Metsähovi Radio Observatory, Metsähovintie 114, FI-02540 Kylmälä, Finland
[127] Gemini Observatory/NSF NOIRLab, 670 N. A'ohōkū Place, Hilo, HI 96720, USA
[128] Frankfurt Institute for Advanced Studies, Ruth-Moufang-Strasse 1, D-60438 Frankfurt, Germany
[129] School of Mathematics, Trinity College, Dublin 2, Ireland
[130] Department of Astrophysical Sciences, Peyton Hall, Princeton University, Princeton, NJ 08544, USA
[131] Department of Physics, Tokyo Institute of Technology, 2-12-1 Ookayama, Meguro-ku, Tokyo 152-8551, Japan
[132] Hiroshima Astrophysical Science Center, Hiroshima University, 1-3-1 Kagamiyama, Higashi-Hiroshima, Hiroshima 739-8526, Japan
[133] Aalto University Department of Electronics and Nanoengineering, PL 15500, FI-00076 Aalto, Finland
[134] Department of Astronomy, Yonsei University, Yonsei-ro 50, Seodaemun-gu, 03722 Seoul, Republic Of Korea
[135] Department of Physics and Astronomy, Texas Tech University, Lubbock, TX 79409-1051, USA
[136] Netherlands Organisation for Scientific Research (NWO), Postbus 93138, 2509 AC Den Haag, The Netherlands
[137] Department of Physics and Astronomy, Seoul National University, Gwanak-gu, Seoul 08826, Republic Of Korea
[138] University of New Mexico, Department of Physics and Astronomy, Albuquerque, NM 87131, USA
[139] Jeremiah Horrocks Institute, University of Central Lancashire, Preston PR1 2HE, UK
[140] Physics Department, Brandeis University, 415 South Street, Waltham, MA 02453, USA
[141] Tuorla Observatory, Department of Physics and Astronomy, University of Turku, Finland
[142] Radboud Excellence Fellow of Radboud University, Nijmegen, The Netherlands
[143] Princeton Gravity Initiative, Princeton University, Princeton, NJ 08544, USA
[144] School of Physics, Huazhong University of Science and Technology, Wuhan, Hubei, 430074, People's Republic of China
[145] Mullard Space Science Laboratory, University College London, Holmbury St. Mary, Dorking, Surrey, RH5 6NT, UK
[146] School of Astronomy and Space Sciences, University of Chinese Academy of Sciences, No. 19A Yuquan Road, Beijing 100049, People's Republic of China
[147] Astronomy Department, University of Science and Technology of China, Hefei 230026, People's Republic of China
[148] Bard College, 30 Campus Road, Annandale-on-Hudson, NY 12504, USA
[149] European Southern Observatory, Alonso de Córdova 3107, Vitacura, Casilla 19001, Santiago de Chile, Chile
[150] Institute of Geodesy and Geoinformation, University of Bonn, D-53113 Bonn, Germany
[151] National Radio Astronomy Observatory, Socorro, NM 87801, USA
[152] Space Radiation Laboratory, California Institute of Technology, 1200 East California Boulevard, Pasadena, CA 91125, USA
[153] Research and Development Weather and Climate Models, Royal Netherlands Meteorological Institute, Utrechtseweg 297, 3731 GA, De Bilt, The Netherlands
[154] Joint ALMA Observatory, Alonso de Córdova 3107, Vitacura 763-0355, Santiago de Chile, Chile
[155] SKA Observatory, Jodrell Bank, Lower Withington, Macclesfield SK11 9FT, UK
[156] European Southern Observatory, Karl-Schwarzschild-Strasse 2, D-85478 Garching, Germany
[157] SOFIA Science Center, Universities Space Research Association, NASA Ames Research Center, Moffett Field, CA 94035, USA
[158] Centro de Astro-Ingeniería (AIUC), Pontificia Universidad Católica de Chile, Av. Vicuña Mackena 4860, Macul, Santiago, Chile
[159] Department of Astronomy, University of Michigan, 1085 South University Avenue, Ann Arbor, MI 48109, USA
[160] National Radio Astronomy Observatory, NRAO Technology Center, 1180 Boxwood Estate Road, Charlottesville, VA 22903, USA